UNIVERSITÀ
DI PARMA

UNIVERSITÀ DEGLI STUDI DI PARMA

DOTTORATO DI RICERCA IN
”FISICA”

CICLO XXXV

OPTIMISING QUANTUM STATE TRANSFER

Coordinatore:
Chiar.mo Prof. Stefano Carretta

Tutore:
Chiar.mo Prof. Sandro Wimberger

Dottorando: Michele Delvecchio

Anni Accademici 2019/2020 - 2021/2022

Michele Delvecchio
Optimising quantum state transfer, © October 2022, Parma

ABSTRACT

The possibility of extending the technological advances with quantum technologies have attracted many scientists since several decades. However, their experimental realization is slowed down due to their errors and noise sensitivity. For this reason, recently, one of the most important challenges to overcome is the necessity of performing reliable and efficient single quantum operations and sequences of them.

This thesis is devoted to the optimization, under unfavorable conditions, of quantum operations by utilizing standard tools of the quantum control framework. In particular, we exploit the intrinsic robustness of the accelerated adiabatic evolution, using the well-known counterdiabatic driving methodology, to realize high-fidelity quantum state transfer. The efficient implementation of such an apparently simple operation is directly linked to many important applications. Indeed, based on previous experimental results, first we optimize the protocol for quantum state transfer between molecular states, otherwise impossible to reach. With the accelerated adiabatic framework we satisfy the requirements imposed by the experimental setup obtaining fidelity and robustness much higher than previous proposals. Second, we study noisy accelerated adiabatic drivings under the effects of decoherence and decay in an open quantum system environment. The results provide new strategies for a further optimization of the driving protocols in order to counteract a wide range of disturbing phenomena. Indeed, for our investigation single and two-qubits gates have been considered using superconducting qubits. Finally, we propose a new compensation scheme exploiting the tunable interactions typical of a Rydberg platform. The application of our protocol to different driving configurations, including the well-known stimulated Raman adiabatic passage, supports the validity of the scheme in a large range of applications.

Our findings provide optimization tools for quantum-state transfer which allow to take a step toward the efficient and reliable realization of fast quantum operations. Indeed, the natural extension of this thesis is the implementation of our strategies in quantum gates with obvious impact in quantum computing.

PUBLICATIONS

From the work of this thesis we have obtained the following three publications:

[1] M. Delvecchio, T. Kirova, E. Arimondo, D. Ciampini and S. Wimberger. " High-fidelity quantum control via Autler-Townes splitting". *Phys. Rev. A* **106**, 052802 (2022)

[2] M. Delvecchio, F. Petiziol, E. Arimondo and S. Wimberger. "Atomic interactions for qubit-error compensation". *Phys. Rev. A* **105**, 042431 (2022)

[3] M. Delvecchio, F. Petiziol and S. Wimberger. "The Renewed Role of Sweep Functions in Noisy Shortcuts to Adiabaticity" *Entropy* **23**, no. 7:897 (2021)

CONTENTS

ACRONYMS

ATH	Adiabatic Theorem
CD	Counterdiabatic Driving
LZ	Landau-Zener
PL	Polynomial
RC	Roland-Cerf
ATAN	Arctan
AC	Avoided Crossing
STA	shortcut-to-adiabaticity
RWA	Rotating-Wave Approximation

1

INTRODUCTION

Since its formulation, quantum mechanics has renewed the physical understanding of the microscopic world. Despite its counter-intuitive explanation of phenomena, many experiments have confirmed its validity, such as the famous Stern-Gerlach experiment which demonstrates the spin property of particles [1]. Quantum mechanics is already used in common devices, such as lasers, transistors, magnetic resonance for medicine purposes and many others. However, they are devices for ”classical” applications that could not replicate the behavior of a quantum system. In fact, Richard Feynman introduced the idea that a classical computer could not simulate efficiently the real quantum world, but a quantum device is needed for this goal [2]. In the year in which this thesis is written, the 40th anniversary of quantum computing is celebrated [3] and the Nobel Prize was given to Alain Aspect, John F. Clauser and Anton Zeilinger for their achievements in quantum optics. Since then, scientists and governments have put a lot of effort in trying to build quantum computers and quantum simulators. Many problems and algorithms, that classical computers can solve in ages, have been rethought such that in their quantum form can be achieved in much shorter time [4]. This is possible by exploiting the quantum phenomena, such as superposition and entanglement, and some exemplary algorithms are the Deutsch-Jozsa [5], Shor [6] and Grover algorithm [7, 8]. Although much progress has been made in recent years for reaching the so called quantum supremacy [9], a lot of work has still to be done. Many types of quantum platform are being explored, such as superconducting circuits [10–12], trapped-ion [13] or Rydberg atoms [14, 15]. We anticipate that part of this thesis is dedicated to the latter type. One of the common problems of all the quantum platforms is the presence of errors which limit the performance of the quantum device. They can be generated by the experimental apparatus or can be intrinsic to the quantum system, as decoherence and decay. To face this problem, tools have been developed like Quantum Error Correction [16, 17] or *Quantum Control* techniques [18, 19]. The present thesis aims at optimizing quantum operations, such that the effects of errors in the systems is limited, using *quantum control* tools.

QUANTUM CONTROL Experimental quantum systems are typically controlled using electromagnetic fields, e.g., laser using different techniques. These techniques are part of the *Quantum Control* theory which studies methods to arbitrarily control the particles dynamics [18]. Its applications range from quantum technologies [20] to the control of molecular processes [21] and quantum metrology [22]. One of the question that quantum control tries to answer is the *controllability* of a system. In other words, the possibility to reach a desired state by means of a control field and, as a consequence, the

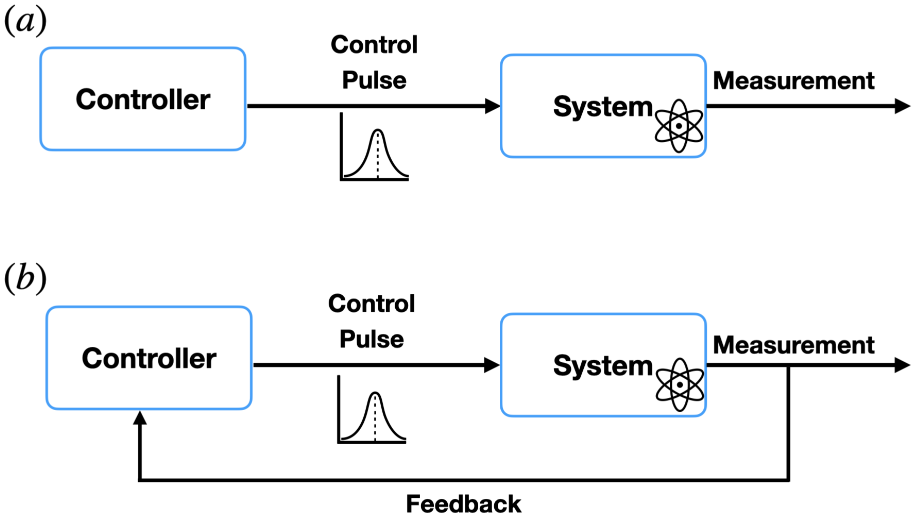

Figure 1.1: Quantum control strategies in (a) open-loop and in (b) close-loop. In the first approach, the controller generates a control pulse which is used to manipulate the dynamics of the system, e.g., atom or qubit, then a measurement is performed according to the desired operation. The second approach, instead, is similar to the one in (a), but the measurement is reported to the controller such that it can optimize the pulse according to the current state and the noise affecting the system.

feasibility of a real-life experiment. Once the system is controllable, the other question concerns the choice of the right strategy in order to control the system in an optimal way. The coherent control strategy is the set of techniques that are used to manipulate a quantum system using semiclassical sources, e.g., laser light, as mentioned before, such that the coherence is maintained. In this way, it is possible to exploit phenomena like superposition and entanglement which are based on constructive or destructive interference between states. In this context, we have two control strategies: open-loop and close-loop. The first technique is described in Fig. 1.1(a). The system is controlled by a controller which generates the proper control pulse to realize a specific quantum operation. After that, the system is measured and the wanted quantity is obtained. The second, strategy instead, represented in Fig. 1.1(b), is similar to the first one but there is a feedback operation that updates the controller in order to optimize in ″run time‟ the control pulse. Despite in the classical counterpart, this strategy works well, with quantum system it is more complicated. The reason lies in the fact that a measurement in such a system will destroy the information, as described by the laws of the quantum mechanics. Additionally, since we are working in an open quantum systems environment we will introduce further noise in the system. Nevertheless, there exist many strategies that address the problem and try to exploit the advantages of the open-loop control [19].

In this thesis, we concentrate on the first method, open-loop quantum control, and we will use various techniques according to the problem we want to address. In particular, among the several techniques that the quantum control theory provides, we will use, e.g., the one based on the Adiabatic Theorem (ATH).

ADIABATIC QUANTUM CONTROL A particular method to control quantum systems requires the use of the adiabatic theorem. Such a theorem has been formulated by Born and Fock already in 1928 [23] and was later extended by Kato in 1950 [24]. It states that, given an eigenstate of the initial Hamiltonian at time $t = t_0$ and a slowly change of the Hamiltonian, the system will follow the evolution of the same instantaneous eigenstate for $t > t_0$. The theorem is very useful especially in quantum control. Knowing the exact evolution of any initial state, allows one to engineer the system in order to obtained a specific target state. This particular type of control is used, e.g., in building adiabatic quantum gates [25, 26], realizing high-fidelity quantum state transfer [27]. It also gave birth to a new paradigm for quantum computation which is called, indeed, *adiabatic quantum computation* [28]. Although the adiabatic approach is a powerful method, one of its most important disadvantage is the very long evolution time required for the optimal performance. In fact, any physical quantum implementation has its own coherence time, according to the specific platform, during which the coherence of the system is preserved and we can perform quantum operation. This is due to the fact that a real quantum system is scarcely perfectly isolated and therefore the interaction with external environments causes decoherence effects. A high-fidelity adiabatic evolution requires infinite time to be performed, and this is in contrast with the limitations imposed by the coherence time of physical implementation. For this reason, techniques to overcome this problem have been developed and they are known as *shortcut-to-adiabaticity (STA)* protocols [29–31]. They allow the perfect adiabatic evolution in a shorter time with respect to the standard adiabatic one. Many protocols have been proposed [29–31] and among them the most famous and most used ones are the so-called Dynamical Invariants and Counterdiabatic Driving (CD) protocols [29]. While the first approach is based on finding the dynamical invariants of a system Hamiltonian $H(t)$, e.g., Lewis-Riesenfeld invariants [32], the second one acts on the system by adding extra terms in the Hamiltonian such that it eliminates the unwanted non-adiabatic transitions between instantaneous eigenstates [33, 34]. Indeed, in the present thesis, in Ch. 3 and 4, we will mostly use the latter method, which has already been experimentally realized [35–39], to optimize and analyze different control functions in close and open environment scenarios.

THIS THESIS In the present thesis, we use the quantum control tools in order to study and optimize quantum operations, especially quantum state/population transfer. Such a quantum operation is useful, e.g., in quantum information science [40] in order to perform basic gate operation as the bit flip (NOT gate) or to prepare specific initial states as in Grover's search algorithm [7, 8]. It is also used in controlling chemical reaction as, e.g., in [41]. In the first result shown in this thesis, we optimize the performance of all-optical spin switch, which exchanges the spin multiplicity character between singlet and triplet states of a molecule. This process is, indeed, realized through a quantum state transfer in a simplified molecular level structure. We will show that this is possible using different adiabatic control functions and that the performance can be further improved by introducing the auxiliary CD terms for accelerating the transfer. Our numerical study is conducted considering an isolated environment and, for this reason, we carried out an additional analysis of the accelerated adiabatic protocols which is the second major result of this thesis. In particular, we studied the effect of typical noise sources in an open quantum-system environment. The study is performed in a simple two-level system and then in a more complicated two-qubits entangling gate. We point out that the control functions can be further optimized according to the type of noise affecting the system. In our third part, instead, we assume the the population transfer, for instance in a bit-flip gate, is affected by errors generated by imperfections in the control parameters. The goal is then to correct such errors and improve the performance of the state transfer. For this purpose, we propose a two-qubit scheme that exploits the interaction between the two to compensate the effects of the error. We specifically considered the Rydberg platform, mentioned above, and the numerical and analytical studies show that it is indeed possible to tune the interaction in order to correct the effects of the errors.

THESIS ORGANIZATION The work starts with an introduction, in part i, on the background concepts needed for the subsequent sections. In particular, we review in detail the ATH mentioned above, the CD protocol, and the control functions that we used. Additionally, the Lindblad master equation is introduced. In part ii instead, Ch. 3 is dedicated to our first result on the optimized all-optical spin switch, while Ch. 4 contains the analysis of the accelerated adiabatic protocols in an open quantum system environment. In Ch. 5, our compensation scheme is described. Finally, in the last part of the thesis (part iv), we summarize the results extensively described in the previous chapters and we overview possible extensions. In particular, we focus on the implementation of adiabatic CZ gate using the quantum control tools described here.

Part I

BACKGROUND

2

THEORETICAL BACKGROUND

This second chapter of the thesis is dedicated to the main theoretical concepts useful for what is studied in the next chapters. As mentioned in Ch. 1, in our analysis we use well-known quantum control tools which can be collected in a more general framework which we call *quantum adiabaticity*. The two main results that we exploit in this thesis are the Adiabatic Theorem (ATH) and the Counterdiabatic Driving (CD). Although both theoretical ideas have been briefly introduced in the previous chapter, here we will present a more rigorous and explicit mathematical treatment. The first section, then, is devoted to the ATH and in particular we will analyzed an its important application in the Landau-Zener (LZ) model [42–45]. The second section, instead, shown the general theory of the CD in the formalism developed by Berry [34]. Then, we will apply it to the LZ problem and we will compare the results with the standard adiabatic case of the previous section. Other adiabatic protocols, besides the LZ one, can be used. In fact, the third section introduces all the sweep functions that are implemented in the next chapters of this thesis. The last part of this chapter, instead, presents another important tool, not only in quantum control theory but also in other fields of the physics, such as quantum optics [46, 47], which is the Lindblad master equation. It provides a general description of the evolution of a system when it is not isolated but it is coupled with the external environment, i.e., open quantum system.

2.1 ADIABATIC THEOREM

The ATH of quantum mechanics was formulated for the first time by M. Born and V. Fock in 1928 [23] and then restudied by Kato in 1950 [24]. The idea is: given a physical system described by a slowly varying Hamiltonian, it remains in its instantaneous eigenstate. In the following we will see the mathematical implications of this statement. We will follow the treatment by Sakurai and Napolitano in [48] which is useful to introduce quantities that we will use in the next sections.

Start by an Hamiltonian depending on a generic parameter $H(t)$. Since the applications of the ATH in this thesis require a time dependent Hamiltonian, from now on we assume that t represents the time. Thus, at every time t we can write

$$\hat{H}(t)|n(t)\rangle = E_n(t)|n(t)\rangle\,, \tag{2.1}$$

where $E_n(t)$ and $|n(t)\rangle$ are, respectively, the instantaneous eigenvalues and eigenstates. Considering the Scrödinger equation

$$\frac{d}{dt}|\psi(t)\rangle = -\frac{i}{\hbar}\hat{H}(t)|\psi(t)\rangle\,, \tag{2.2}$$

we can expand the state of the system $|\psi(t)\rangle$ onto the instantaneous basis of Eq. (2.1)

$$|\psi(t)\rangle = \sum_n c_n(t)|n(t)\rangle\,, \tag{2.3}$$

with time dependent coefficients $c_n(t)$. At this point, plugging Eq. (2.3) into the Eq. (2.2), we get a differential equation for the time dependent coefficients

$$\sum_n \left(\dot{c}_n(t)|n(t)\rangle + c_n(t)|\dot{n}(t)\rangle\right) = -\frac{i}{\hbar}\sum_n c_n(t)E_n(t)|n(t)\rangle \tag{2.4}$$

where we have used the Eq. (2.1) and, for the sake of readability, we have adopted the dot "·" notation for the time derivative.

Projecting onto the state $|m(t)\rangle$ and using the fact that $\langle m(t)|n(t)\rangle = \delta_{mn}$ we get

$$\dot{c}_m(t) = -\frac{i}{\hbar}c_m(t)E_m(t) - \sum_n c_n(t)\langle m(t)|\dot{n}(t)\rangle\,. \tag{2.5}$$

The next step is to find an expression for $\langle m(t)|\dot{n}(t)\rangle$. Then, if we differentiate both sides of the Eq. (2.1) and we take the inner product with $|m(t)\rangle$, we obtain

$$\langle m(t)|\dot{n}(t)\rangle = \frac{\langle m(t)|\dot{H}(t)|n(t)\rangle}{E_n(t) - E_m(t)}\,, \tag{2.6}$$

which holds only for $m \neq n$ such that the denominator of Eq. (2.6) is not 0. It represents the so called nonadiabatic couplings between the eigenstates. We would like to highlight this relation because it is strictly related with the CD tool, and we will find it also in the next section.

Now, if we separate the diagonal term from the off-diagonal one in Eq. (2.5), we can substitute Eq. (2.6) in it, obtaining

$$\dot{c}_m(t) = i\left(-\frac{E_m(t)}{\hbar} + i\langle m(t)|\dot{m}(t)\rangle\right)c_m(t) - \sum_{n\neq m} c_n(t)\frac{\langle m(t)|\dot{H}(t)|n(t)\rangle}{E_n(t) - E_m(t)}\,. \tag{2.7}$$

Now, by assumption, we consider that the Hamiltonian $\hat{H}(t)$ change very slowly in time and consequently the corresponding term is very small compared to the other. With this, we can neglect the nonadiabatic couplings resorting to the so called *adiabatic approximation*. Equation (2.7) now reads

$$\dot{c}_m(t) \simeq i\left(-\frac{E_m(t)}{\hbar} + i\langle m(t)|\dot{m}(t)\rangle\right)c_m(t)\,. \tag{2.8}$$

Integrating such an equation, we directly obtain the adiabatic theorem.

$$c_m(t) \simeq e^{i\theta(t)}e^{i\gamma(t)}c_m(0)\,, \tag{2.9}$$

where the phase

$$\theta(t) = -\frac{1}{\hbar}\int_0^t E_m(t')dt' \tag{2.10}$$

is the *dynamical phase* and

$$\gamma(t) = i\int_0^t \langle m(t')|\dot{m}(t')\rangle dt' \tag{2.11}$$

is the famous *Berry phase* or *geometric phase* [49].

The last step is to determine the nature of the two phases. The dynamical phase $\theta(t)$ is real, in fact, in Eq. (2.10) we are integrating an eigenvalue which is real, given the Hamiltonian $\hat{H}$ is Hermitian, and so the result is still real. For the geometric phase we need to perform one more step. Starting from the orthonormality of the eigenstates $1 = \langle m(t)|m(t)\rangle$, we can differentiate both sides getting

$$\begin{aligned} 0 &= \langle \dot{m}(t)|m(t)\rangle + \langle m(t)|\dot{m}(t)\rangle = \\ &= \langle m(t)|\dot{m}(t)\rangle^* + \langle m(t)|\dot{m}(t)\rangle = 2\,\Re\left(\langle m(t)|\dot{m}(t)\rangle\right), \end{aligned} \tag{2.12}$$

where $\Re$ is the real part of a complex number z, and we have used the relation $z + z^* = 2\Re(z)$. Equation (2.12) tells us that $\langle m(t)|\dot{m}(t)\rangle$ is purely imaginary. Therefore, in the Eq. (2.11), $i\langle m(t)|\dot{m}(t)\rangle$ is purely real.

Equation (2.9) show that the system remains approximately in its instantaneous eigenstate if the adiabatic approximation holds.

2.1.1 Example: *Landau-Zener model*

A typical example of the application of the ATH is the Landau-Zener (LZ) problem. It has been formulated from Landau, Zener, Stueckelberg and Majorana independently [42–45]. They derived an analytical formula to calculate the probability of nonadiabatic transitions in a two level system.

In this section we briefly review the model and then we will see the ATH implications on the transition probability. We will make use of this model also in the next chapters as a toy model to understand better the phenomena occurring in more complex systems.

Let us consider a two level system Hamiltonian

$$\hat{H}(t) = \hbar\alpha t\hat{\sigma}_z + \hbar\Omega\hat{\sigma}_x \tag{2.13}$$

where t is the time, α is a scaling parameter, Ω is the coupling between the two levels and $\hat{\sigma}_i$ with $i = (x, y, z)$ are the Pauli matrices. For a better comprehension of the problem, we describe the Fig. 2.1. It shows the instantaneous eigenstates vs. time of the Eq. (2.13) represents a typical situation of anticrossing (or Avoided Crossing (AC)) where the two instantaneous eigenstates never cross each each other during the whole duration of the evolution. To understand the process, let us consider the Eq. (2.13) without the coupling, so $\Omega = 0$. The time dependent eigenvalues, in this case, are $\pm\hbar\alpha t$ and they are represented by the dashed lines in the Fig. 2.1. When $\Omega \neq 0$, the two instantaneous eigenvalues become $|n_{\pm}(t)\rangle = \pm\hbar\sqrt{\alpha^2 t^2 + \Omega^2}$ represented by the solid lines in the figure 2.1. From the latter expression we can appreciate the meaning of the name *AC*, in fact, while in the case with $\Omega = 0$ the two

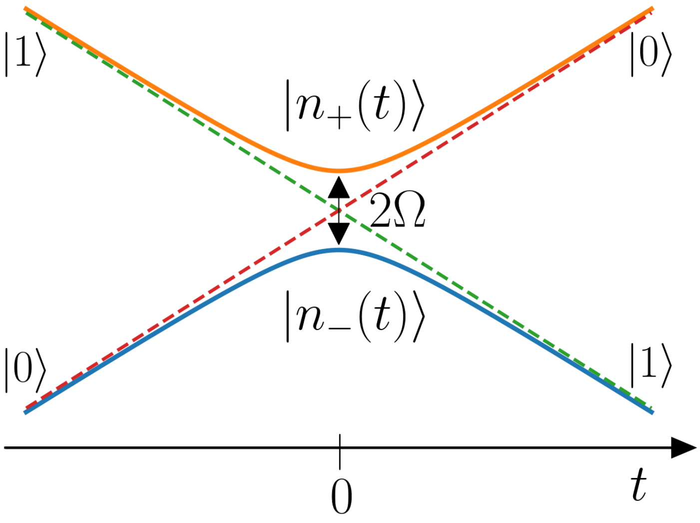

Figure 2.1: Typical example of an AC. It shows the instantaneous eigenvalues vs. time of the two level system in Eq. (2.13). At time $t \to -\infty$ the two instantaneous eigenstates tend to the bare eigenstates, namely $|n_+(t)\rangle \to |1\rangle$, $|n_-(t)\rangle \to |0\rangle$. If the Hamiltonian is slow enough in time, at time $t \to \infty$, the situation is inverted: $|n_+(t)\rangle \to |0\rangle$, $|n_-(t)\rangle \to |1\rangle$. If the Hamiltonian is not sufficiently slow, at final time the two instantaneous eigenstates are a mix between the two bare ones due to the non adiabatic transitions.

eigenvalues cross at $t = 0$, when $\Omega \neq 0$ they do not cross anymore, with a minimum gap occurring at $t = 0$ and it is twice the value of the coupling, $2\hbar\Omega$ in our case, as it can be observed in the figure.

The ATH allows us to exploit this situation to perform a population transfer. In fact, in the adiabatic approximation, we follow a specific eigenstate instantaneously. For instance, let us consider the Fig. 2.1, starting at $t \to -\infty$ in the bare state $|0\rangle$ and adiabatically following the eigenstate $|n_-(t)\rangle$, at time $t \to \infty$ we will end in the bare state $|1\rangle$. Therefore, the state transfer $|0\rangle \to |1\rangle$ is realized.

From a practical point of view, we have to deal with a finite evolution time. For the purpose, in the most general manner, we will assume that the protocol lasts a time $2t_f$ (from $t_I = t_c - t_f$ to $t_F = t_c + t_f$) and the AC occurs at time t_c. Now, we introduce a change of variables which will be also useful in the next sections. First we use a rescaled time $\tau = (t - t_I)/2t_f$ so that $\tau \in [0, 1]$, and then we chose the coupling $\hbar\Omega$ as the energy reference, so we have $T = 2t_f\Omega$ and $\alpha_\Omega = \alpha t_f/\Omega$. In this way, setting $\hbar = 1$, the Eq. (2.13) becomes

$$H(\tau) = 2\,\alpha_\Omega \left(\tau - \frac{1}{2}\right)\hat{\sigma}_z + \hat{\sigma}_x\,. \tag{2.14}$$

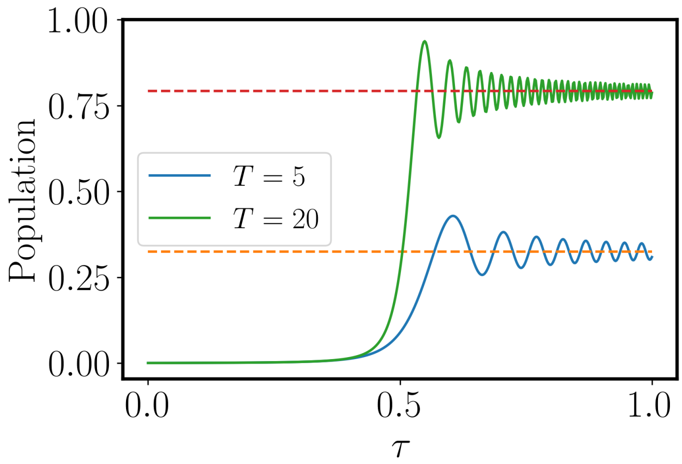

Figure 2.2: Solid lines indicate population of state $|1\rangle$ for two values of T, in particular $T = 5$ for the blue solid line and $T = 20$ for the green one. Before the AC at $\tau = 0.5$, the population is completely in the initial state, $|0\rangle$ in this case. After, it starts to occupy also the state $|1\rangle$ in an oscillatory manner, around a limit value determined by the formula (2.16) with $1 - P_{LZ}$ and represented by the dashed lines. In these simulations we set $\alpha_\Omega = 20$. Both the values of T do not satisfy the adiabatic approximation, but it can be done just by choosing a larger value. In that case, the transfer efficiency will be close to 100% and no oscillations are present anymore.

in dimensionless quantities. In this description, α_Ω is the control parameter acting on the gap at $\tau = 0$ (initial gap) between the eigenvalues and therefore larger is better. The corresponding Schödinger equation reads

$$i\partial_\tau \psi(\tau) = TH(\tau)\psi(\tau)\,. \tag{2.15}$$

where T is the only parameter controlling the time duration of the protocol. The theoretical formula for the probability of diabatic transitions with these parameters is [42–45]

$$P_{LZ} = e^{-\frac{\pi T}{2\alpha_\Omega}}\,. \tag{2.16}$$

The formula can be obtained following, e.g., the approach in [50] using tools from complex analysis.

We are going to show in Fig. 2.2 how the adiabaticity influences the probability in a population transfer and, in this case, it is controlled by the parameter T. The solid lines of Fig. 2.2 show the probabilities of the state $|1\rangle$, which we call *fidelity*, for two exemplary values of T. When $T = 5$ the evolution is too fast and therefore the diabatic transition dominates and the most of the probability remains in the state $|0\rangle$. Viceversa, when $T = 20$ the evolution is slower than the previous case, and in fact we reach better values of fidelity. We observe that the probabilities of both cases are zero before the AC, centered in $\tau = 0.5$, and then they start to grow. They present oscillations around the value $1 - P_{LZ}$ predicted by the theoretical formula of Eq. (2.16), represented by the dashed lines in the figure.

2.2 COUNTERDIABATIC DRIVING

In the previous chapter we have seen that in order to satisfy the adiabatic approximation and perfectly follow an instantaneous eigenstate, we need a very long evolution time. This condition could generate problems because of the short coherence time in a quantum systems. Therefore, shortcut to adiabaticity protocols have been developed and one of these is the *Counterdiabatic Driving (CD)* or *transitionless quantum driving*. It has been developed independently by [33] in 2003 and [34] in 2009.

In this section we review the idea behind the CD protocol presented in [34], and we adapt it to the LZ example.

As in the ATH, let us start with a system described by a time dependent Hamiltonian satisfying

$$H_0(t)|n(t)\rangle = E_n|n(t)\rangle\,, \tag{2.17}$$

where E_n and $|n(t)\rangle$ are the eigenvalues and eigenstates respectively. If the adiabatic approximation seen in the previous section holds, the state of the system simply follows the instantaneous eigenstate. Therefore it has the same form of the Eq. (2.9)

$$|\psi_n(t)\rangle = e^{i\theta(t)}e^{i\gamma(t)}|n(t)\rangle\,, \tag{2.18}$$

where $\theta(t)$ and $\gamma(t)$ are the same quantities defined in Eqs. (2.10) and (2.11) respectively. So far, the treatment seems very similar to the one we have seen in the ATH. However, here, we look for an Hamiltonian that drives the state of the system in a perfect adiabatic manner without resorting to any type of approximation. To do that, we start from the Schödinger equation for the evolution operator $U(t)$

$$i\hbar\partial_t U(t) = H(t)U(t)\,, \tag{2.19}$$

and exploiting the unitarity of $U(t)$ we can write

$$H(t) = i\hbar(\partial_t U(t))U^\dagger(t)\,. \tag{2.20}$$

Now, since we want to have a perfectly adiabatic evolution, we chose $U(t)$ such that

$$U(t) = \sum_n e^{i\theta(t)}e^{i\gamma(t)}|n(t)\rangle\langle n(0)|\,. \tag{2.21}$$

In this way we have built the unitary operator that evolves the state perfectly adiabatic. Now we want to derive the Hamiltonian which generates such an operator. Therefore, let us substitute Eq. (2.21) in the Eq. (2.20) to easily obtain

$$\hat{H}(t) = \sum_n E_n(t)|n(t)\rangle\langle n(t)| + i\hbar\sum_n |\partial_t n(t)\rangle\langle n(t)| - \langle n|\partial_t n(t)\rangle|n(t)\rangle\langle n(t)|\,. \tag{2.22}$$

In this description we can highlight the two parts of $H(t)$ as

$$\hat{H}(t) = \hat{H}_0(t) + \hat{H}_{CD}(t)\,, \tag{2.23}$$

where the first term $H_0(t)$ depends on the instantaneous eigenvalues and eigenstates, while the second one $H_{CD}(t)$ depends on the time variation of the instantaneous eigenstates.

We have already encountered the term $\langle n(t)|\partial_t n(t)\rangle$ in the previous section, in particular in the Eq. (2.6). Therefore, we can exploit the previous result to write $H_{CD}(t)$. Let us use the completeness relation and split the diagonal part from the off-diagonal one

$$\begin{aligned}\hat{H}_{CD}(t) &= i\hbar\sum_n\left(\sum_m |m(t)\rangle\langle m(t)|\partial_t n(t)\rangle\langle n(t)| - \langle n|\partial_t n(t)\rangle|n(t)\rangle\langle n(t)|\right)\\ &= i\hbar\sum_{m\neq n}\sum_n |m(t)\rangle\langle m(t)|\partial_t n(t)\rangle\langle n(t)|\,,\end{aligned} \tag{2.24}$$

where the last term in the first line cancels out with the diagonal terms of the sum on m. Substituting now the result in Eq. (2.6), we obtain

$$\hat{H}_{CD}(t) = i\hbar\sum_{m\neq n}\sum_n |m(t)\rangle\frac{\langle m(t)|\dot{H}(t)|n(t)\rangle}{E_n(t)-E_m(t)}\langle n(t)|\,. \tag{2.25}$$

This latter equation is the key result of the Demirplak-Rice's and Berry's idea. What is the difference with the formula in the ATH? The difference lies in the way the eigenstates of $H_0(t)$ are driven. Using the ATH we made the assumption of a very slow varying Hamiltonian, while in this case we have not made any type of assumption or approximation. Therefore, using the Eq. (2.25), $H(t)$ is able to drive in a perfectly adiabatic way the eigenstates of $H_0(t)$ in an arbitrary fast way. From here, the reason of the name *shortcut to adiabaticity*. The drawback of this approach is the necessity of introducing extra control fields which, usually, may be difficult to realize experimentally.

2.2.1 *Two-level system*

The theory just explained is very general and the only constraint is the non degeneracy of the eigenvalues. In order to evaluate the Hamiltonian $\hat{H}_{CD}(t)$ the whole systems (eigenvalues and eigenvectors) must be known and this could be a problem when one try to calculate $\hat{H}_{CD}$ analytically. In this section we compute the correction Hamiltonian $\hat{H}_{CD}(t)$ for a general two level system as our generic example. The result, then, will be applied to our Landau-Zener problem in the next section. Let us consider a generic Hamiltonian for a spin $1/2$ system, with $\hbar = 1$

$$\hat{H}(t) = f(t)\hat{\sigma}_z + g(t)\hat{\sigma}_x\,, \tag{2.26}$$

with $f(t)$ and $g(t)$ two generic time dependent functions. The instantaneous eigenvalues are $n_\pm = \pm\sqrt{f(t)^2 + g(t)^2}$ and the corresponding eigenvectors can be defined in the parametric form with the mixing angle

$$\tan\left(2\theta(t)\right) = \frac{g(t)}{f(t)} \Rightarrow \theta(t) = \frac{1}{2}\arctan\left(\frac{g(t)}{f(t)}\right) \tag{2.27}$$

such that we have

$$|n_+(t)\rangle = -\sin(\theta)|0\rangle + \cos(\theta)|1\rangle \tag{2.28}$$

$$|n_-(t)\rangle = \cos(\theta)|0\rangle + \sin(\theta)|1\rangle\,. \tag{2.29}$$

Now let us compute $\hat{H}_{CD}(t)$. Start from the time derivative of the Hamiltonian (2.26)

$$\partial_t \hat{H}(t) = \dot{f}(t)\hat{\sigma}_z + \dot{g}(t)\hat{\sigma}_x\,. \tag{2.30}$$

Then

$$\frac{\langle n_-(t)|\partial_t \hat{H}(t)|n_+(t)\rangle}{n_+ - n_-} = \frac{\dot{g}(t)f(t) - \dot{f}(t)g(t)}{f^2(t) + g^2(t)} = 2\,\partial_t\theta(t)\,. \tag{2.31}$$

Finally we have

$$\hat{H}_{CD}(t) = 2\,\partial_t\theta(t)\,\hat{\sigma}_y\,. \tag{2.32}$$

In this case, we can notice that the counterdiabatic field is orthogonal with respect to the operators composing the Hamiltonian (2.26). This property is extensively investigated in [51, 52]. In the following, we will exploit the well known result of Eq. (2.32) for our LZ problem seen in the previous section.

2.2.2 Example: *Counterdiabatic Landau-Zener*

In the previous section we have seen the analytical expression for the CD field in a spin $1/2$ system. Here, instead, we apply that result to compute $\hat{H}_{CD}$ for the LZ system introduced in the Sec. 2.1.1.

Recall the Hamiltonian (2.14) with mixing angle

$$\tan(2\theta(\tau)) = \frac{1}{2\alpha_\Omega\left(\tau - \frac{1}{2}\right)} \Rightarrow \theta(\tau) = \frac{1}{2}\arctan\left(\frac{1}{2\alpha_\Omega\left(\tau - \frac{1}{2}\right)}\right), \tag{2.33}$$

eigenvalues $\pm\sqrt{\alpha_\Omega^2\left(2\tau - 1\right)^2 + 1}$ (with $\hbar = 1$) and eigenstates defined in the Eqs. (2.28) and (2.29). Applying directly Eq. (2.32), we obtain

$$\hat{H}_{CD}(\tau) = h_{CD}(\tau)\hat{\sigma}_y = -\frac{\alpha_\Omega}{1 + 4\alpha_\Omega^2\left(\tau - \frac{1}{2}\right)^2}\,\hat{\sigma}_y\,. \tag{2.34}$$

The new Hamiltonian is then

$$\hat{H}_{tot}(\tau) = T\left[2\,\alpha_\Omega\left(\tau - \frac{1}{2}\right)\hat{\sigma}_z + \hat{\sigma}_x\right] - \frac{\alpha_\Omega}{1 + 4\alpha_\Omega^2\left(\tau - \frac{1}{2}\right)^2}\,\hat{\sigma}_y\,, \tag{2.35}$$

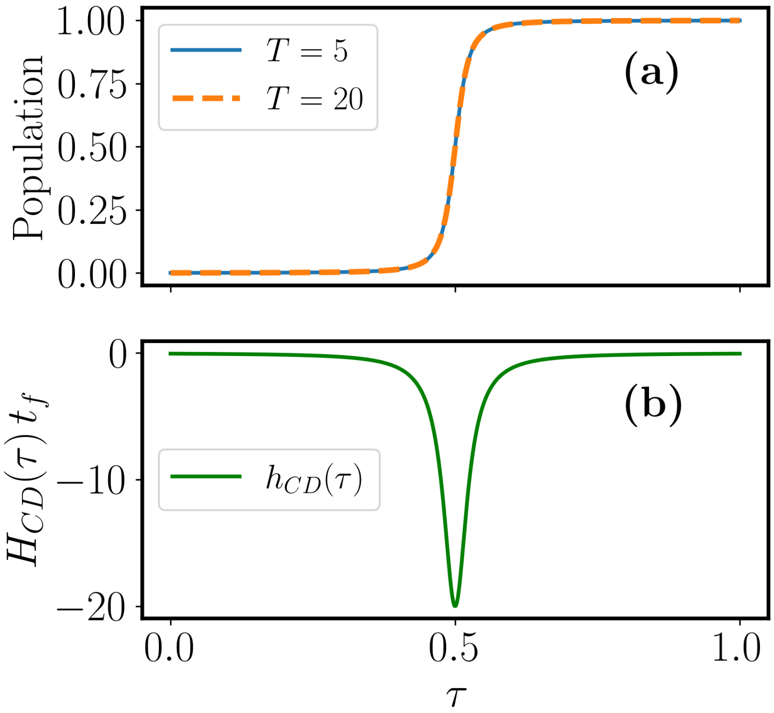

Figure 2.3: (a) Population of the state $|1\rangle$ vs. rescaled time τ for $T = 5$ (solid blue line) and $T = 20$ (orange dashed line). In the presence of the $\hat{H}_{CD}$ correction they show the very same behavior independent of the value of T. In contrast to the Fig. 2.2, in both cases they reach very high fidelities (very close to 1) after the AC. (b) Shape of the matrix element h_{CD} as a function of the rescaled time τ. We notice that the Lorenzian peak is centered at the AC which is where the non-adiabatic transitions are more probable. Other parameter used in these simulations is $\alpha_\Omega = 20$.

where T has been defined before Eq. (2.14). The effects of the Eq. (2.34) on the evolution are shown in Fig. 2.3. In particular, in Fig. 2.3(a) we simulate Eq. (2.35) for the same parameters of the Fig. 2.2. The result is that the Berry correction completely eliminates the non-adiabatic transitions, reaching in this way, a perfect transfer efficiency. In Fig. 2.3(b), instead, we can observe the Lorentzian shape of the matrix element, identified by the $h_{CD}(\tau)$ factor in the Eq. (2.34), of $\hat{H}_{CD}$. Its peak is centered on the AC, namely where the non-adiabatic transitions occur.

2.3 SWEEP FUNCTIONS

As we have seen in the previous sections, an ideal adiabatic evolution requires an infinite time in order to have a perfect following of the instantaneous eigenstate. However, real physical implementation of adiabatic protocols needs to be performed in a finite time. For this reason, the transition is not perfect and errors accumulate during the evolution. To mitigate such errors, one can optimize the variation rate of the Hamiltonian by designing specific functions with different characteristic. During the years many adiabatic protocols have been studied [53–56], each with its own characteristic. Here, we present different families of sweep functions that we use in the first part of this thesis according to the objective of the work. As we will see, each adiabatic protocol has its own shape based on the optimization method used. In particular, we chose the following adiabatic protocols: (i) Landau-Zener-like (linear time dependence) [53, 56], (ii) Polynomial [55, 56], (iii) Roland-Cerf [53, 56–58] and (iv) Arctan. They are found by exploiting different methods, i.e., (i) is not optimized and it is very similar to the Landau-Zener case that we have seen in the Ch. 2, (ii) is found with the Boundary Cancellation Methods (BCMs) [55] while (iii) is derived from Local Adiabatic Driving (LAD) methods [54, 57]. The sweep (iv), instead, is created ad-hoc to satisfy specific requirements that we will see in Ch. 3. Each function has been chosen for its different time-dependence and, consequently, behavior near the AC. In particular, the LZ ramp is the simplest one and it is characterized by a constant rate during the entire evolution. Then, the PL one is slow far away from the AC and very fast near it. On the contrary, the RC protocol is optimized such that it is very fast far away from AC and very slow close to it. Due to the requirements that we will see in Ch. 3, the ATAN function is designed with a "non-standard" approach. In detail, it is very fast at the beginning of the evolution and very slow once approached the avoided crossing. An exemplary plot of their temporal profile, which is not related to their use in the next chapters, can be seen in Fig. 2.4.

$$\text{(i)}\quad f_{LZ}(\tau) = f_0\,(1-2\tau) \tag{2.36}$$

$$\text{(ii)}\quad f_{PL}(\tau) = \frac{f_0}{13}\left(13 - 280\tau^3 + 490\tau^4 - 336\tau^5 + 140\tau^6 - 40\tau^7\right) \tag{2.37}$$

$$\text{(iii)}\quad f_{RC}(\tau) = \frac{f_0(1-2\tau)}{\sqrt{1+4\alpha_\Omega^2 f_0^2\tau(1-\tau)}} - c_1 \tag{2.38}$$

$$\text{(iv)}\quad f_{AT}(\tau) = f_0 \arctan\left(c_2\tau\right) - c_3\,, \tag{2.39}$$

where $f_0 = f(0) > 0$, τ and α_Ω are the dimensionless quantities defined in Sec. 2.1.1 and c_1, c_2, c_3 are parameters that we will use for optimizing the sweeps (iii) and (iv) in Ch. 3. In App. A we show how we adapted the functions (ii) and (iii), already derived in [55, 56] and [54, 56, 57], respectively, to our problem.

2.4 LINDBLAD MASTER EQUATION

So far, we have presented theoretical results describing closed quantum systems, meaning that they are isolated and they are not perturbed by the surrounding environment (also called *bath*). However, for measuring or controlling the system one has to interact with it from the external, and therefore other degrees of freedom are introduced. The system is then called "open", in the sense that other phenomena can influence its dynamics [59, 60]. For instance, the dynamics can be affected by *dissipation*, which causes the loss of information contained in the system, *memory* effects, such that the state of the

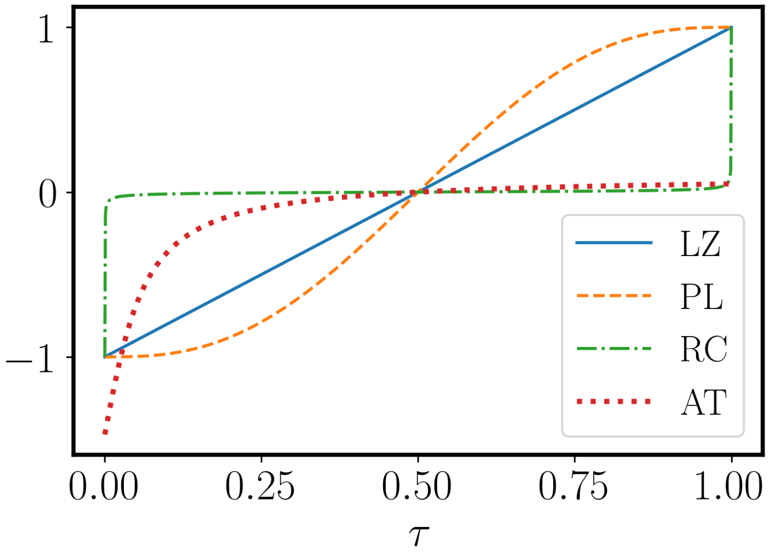

Figure 2.4: Temporal profile of the sweeps functions of Eqs. (2.36), (2.37), (2.38) and (2.39). In this plot we assume that the avoided crossing occurs at $\tau = 0.5$. In this condition, the LZ protocol has a linear behavior and it is represented by the solid blue line; the PL, the dashed orange line, is slow far away from the avoided crossing and fast near it; on the contrary, the RC, represented by the dash-dot green line, is slow far away from the avoided crossing and very slow near it; the ATAN sweep, instead, the dashed red line, is very fast at the beginning of the protocol and it becomes very slow approaching the AC. In the present vertical scale, the ATAN sweep does not reach 1 because it is optimized for the specific protocol in Sec. 3.3.

system depends on its previous history, and also *decoherence* which consists in the loss of the coherences between the system states. Therefore, the standard quantum theory is not sufficient anymore for a complete description of the system. To address this problem, a theory for open quantum systems has been developed [59, 60]. In general, the Hamiltonian of the system to be described is of the form

$$H_T = H_S \otimes \mathbb{1} + \mathbb{1} \otimes H_E + H_I \,, \tag{2.40}$$

where H_T is the total system, H_S is the Hamiltonian of the "target" quantum system, H_E is the environment Hamiltonian and H_I is the term describing the interaction between the two. As mentioned before, the open quantum system description is useful to study an experimental situation where the system interacts with the external environment. In this scenario, however, the information about a quantum state is not perfect and there are some uncertainties. For this reason, a more complete description of the system state is given by the density matrix, which is defined as

$$\rho = \sum_i p_i |\psi_i\rangle\langle\psi_i| \,, \tag{2.41}$$

where p_i is the probability of being in the i-th state and $\sum_i p_i = 1$. Two properties of ρ are: (i) it has unit trace, that is $Tr[\rho] = 1$ and (ii) it is a positive matrix, i.e., $\rho > 0$. Given this, the most important missing part is an equation describing the temporal dynamics of the system H_S. For this purpose, one of the most famous equation is the so called Lindblad equation (or Gorini-Kossakowski-Sudarsahan-Lindblad equation) [61, 62]. Its derivation is quite long and it is extensively addressed in, e.g., [60, 63]. In contrast, in this section we limit our analysis on its validity conditions without entering in detailed calculations. The Lindblad equation is derived under three strong approximations:

(i) The first approximation is called *Born approximation* and it consist in assuming that the coupling between the system and environment is very weak. This means that environment has a small influence on the system and the state at time t can be approximated as

$$\rho(t)_T \approx \rho_S(t) \otimes \rho_E \,. \tag{2.42}$$

(ii) The second approximation is the *Markov approximation* which requires that the time scales over which the system varies are much slower than those of the environment. Together with (i), they are called *Born-Markov approximation* [60].

(iii) The third is the Rotating-Wave Approximation (RWA) which allows to neglect terms oscillating faster than the frequencies of the phenomena considered in the system. We use such an approximation also in other context in this thesis, for instance when we derive Eq. (3.4) in app. B.1.1.

Now, using this three approximations, one can derive the Lindblad master equation which reads [60, 63]

$$\frac{d\rho(t)}{dt} = -\frac{i}{\hbar}\left[H(t), \rho(t)\right] + D[\hat{c}]\rho(t) \,, \tag{2.43}$$

where $\rho(t)$ is the density matrix describing the state of the system, $[H(t), \rho(t)] = H(t)\rho(t) - \rho(t)H(t)$ is the commutator, $\hat{c}$ is the jump or collapse operator and $D[\hat{c}]\rho(t)$ is the dissipator which is defined as

$$D[\hat{c}]\rho(t) = \hat{c}\rho(t)\hat{c}^\dagger - \frac{1}{2}\left\{\hat{c}^\dagger\hat{c}, \rho(t)\right\} \,, \tag{2.44}$$

being $\left\{\hat{c}^\dagger\hat{c}, \rho(t)\right\} = \hat{c}^\dagger\hat{c}\rho(t) + \rho(t)\hat{c}^\dagger\hat{c}$ the anticommutator.

In this thesis, we consider typical scenario from the quantum optics where, in general, all three conditions are satisfied and the Lindblad master equation can be used.

2.5 REMARKS

In this chapter, we have reviewed some important well-known theoretical results that are used for studying the problems in the next chapters. In particular, in Sec. 2.1, we started with the ATH as a powerful tool for controlling a quantum system. Then, we have seen its application to one of the most famous avoided crossing problem, that is the LZ. However, as showed in Fig. 2.2, for obtaining an optimal state transfer fidelity and reducing the non-adiabatic transitions probability, we need a very long evolution time which is unfeasible in a real implementation. The solution for this is presented, then, in Sec. 2.2 where the STA protocol is introduced. In particular, we have reviewed the theory of the CD developed by Berry [34] and we have applied it to the same LZ problem of the previous section. We analytically computed the extra H_{CD} term and Fig. 2.3 showed that it is able to perfectly eliminate the non-adiabatic transitions and obtaining a fidelity, ideally, 1 in a shorter time compared to the standard adiabatic evolution. In Sec. 2.3, instead, we have shown that the changing rate of the Hamiltonian can be optimized by properly design the sweep functions. We have introduced four different adiabatic protocols, each with its own characteristics. In the next chapters (Ch. 3 and 4), we will see that such sweeps can be accelerated with the CD. In the latter Sec. 2.4, instead, we introduced the Lindblad master equation for solving the dynamic of an open quantum system. Such an equation will be useful for studying the behavior of the sweep functions under the effects of decoherence and decay, typical of open quantum system scenarios.

Part II

ACCELERATED ADIABATIC DRIVING

3

OPTIMIZATION OF POPULATION TRANSFER

In this chapter, we presents our first result about the application of the quantum control techniques showed in the previous Ch. 2. In particular, we will use the ATH and CD tools to perform an high-fidelity population transfer in a multi-level system. In the following, first, in Secs. 3.1 and 3.2, we introduce the scientific context and then the system together with the adiabatic protocol used for the evolution, referring to those presented in Sec. 2.3. Then we compare the performance of the sweep functions in two different regimes: in Sec. 3.4, a reduced three-level model and in Sec. 3.5 the complete four-level one.

3.1 INTRODUCTION TO THE CONTEXT

Quantum control tools have been applied not only in simple few levels systems but also in more challenging scenarios as, e.g., the molecules [20, 21, 64–67]. Due to the complex level structure of a molecule, controlling the transfer between any state is not an easy task in non-relativistic quantum mechanics. However, in the latter years, the relativistic phenomena have been exploited using, for instance, the spin-orbit coupling which creates a mixing between electronic states. This has been observed in several systems, e.g., [68–70] and being able to control it can allow, for instance, the access to otherwise inaccessible system states (see, e.g., [71, 72]). A number of theoretical studies have been performed in the subject [73–76] using resonant and nonresonant laser field. One of the techniques for controlling the spin-orbit coupling exploits the Autler-Townes effect [77, 78]. It generates a shift of the energy level when an oscillating electric field is applied in resonance to that level. This has been used in [79] for controlling the spin-orbit coupling in lithium dimer (Li_2). This has been possible since, in contrast to other molecules which have been characterized, as Na_2 [80], K_2 [81], Rb_2 [82] and Cs_2 [83] (see [84] for a more complete list), the spin-orbit coupling in Li_2 is weak and therefore easier to control. Its characterization has been done in [85] while in [84] a simplified four-level structure is provided in their Fig. 2. The considered states have singlet and triplet spin character mixed by the spin-orbit coupling. With those states, in [84] the authors realize an all-optical spin switch [74, 86, 87] by using a continuous-wave field exploiting the Autler-Townes effect. In our work, instead, the objective is to improve the protocol using a time dependent control driving. In this way, we aim at realizing an all-optical switch faster than theirs and with higher efficiency based on the quantum control tools introduced in Ch. 2. Unlike in [84], where the authors studied the all-optical switch with an effective two level system, we realize it in the simplified four-level which is still more similar to the experimental realization in [79]. Such a

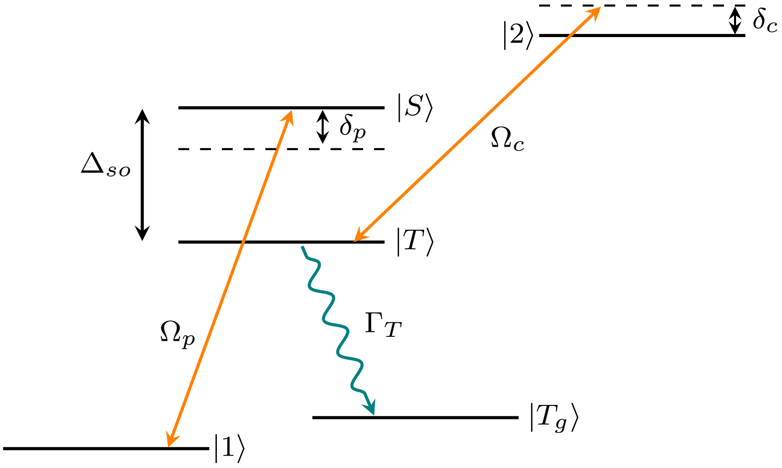

Figure 3.1: Level scheme of the bare states of the system. There are two lasers with Rabi frequencies Ω_p, with detuning δ_p, and Ω_c, with detuning δ_c, controlling the transitions $|1\rangle \to |S\rangle$ and $|T\rangle \to |2\rangle$ respectively. The level $|T\rangle$, separated from $|S\rangle$ by the energy $\hbar\Delta_{so}$, decays towards the level $|T_g\rangle$, which is the target level that will be measured, with a rate of Γ_T indicated by the wavy arrow in the figure.

treatment is valid also for other quantum systems experiencing the spin-orbit coupling.

3.2 SYSTEM SETUP

The system, already experimentally investigated in [79, 84, 88] and theoretically in [73], consists of a complex level structure. However, for our purposes, we use the simplified four levels model, as mentioned above, labeled $|1\rangle, |S\rangle, |T\rangle$ and $|2\rangle$, plus an extra level $|T_g\rangle$ needed for the experimental measures. The scheme is shown in Fig. 3.1 where we can distinguish two lasers driving the transitions $|1\rangle \to |S\rangle$ and $|T\rangle \to |2\rangle$ with Rabi frequency Ω_p and Ω_c and detunings $\delta_p = \omega_p - (E_S - E_1)$ and $\delta_c = \omega_c - (E_2 - E_T)$ respectively. In our case, as represented by the dashed lines in the Fig. 3.1, δ_c is blue detuning, since it assumes only positive values, while δ_p is red detuning, since is mainly negative. The all-optical switch is realized through a population transfer, that is, so, our objective.

We want to prepare a triplet state which translate into realizing the population transfer from the state $|1\rangle$ to the triplet state $|T\rangle$ without populating the singlet state $|S\rangle$. As studied in [73], the spin-orbit coupling between two original unperturbed singlet and triplet states $|S_0\rangle$ and $|T_0\rangle$, separated by energy $\hbar\Delta_0$, generates the two perturbed states $|S\rangle$ and $|T\rangle$ with energy separation $\hbar\Delta_{so}$. The spin-orbit coupling V is written in the form ($\hbar = 1$)

$$H_{so} = V\left(|S_0\rangle\langle T_0| + |T_0\rangle\langle S_0|\right) , \tag{3.1}$$

and the two perturbed states read

$$|S\rangle = \alpha|S_0\rangle - \beta|T_0\rangle \qquad\qquad |T\rangle = \beta|S_0\rangle + \alpha|T_0\rangle , \tag{3.2}$$

where $|\alpha|^2 + |\beta|^2 = 1$. Moreover, the relations between the spin-orbit coupling V and the energy $\hbar\Delta_0$ with $\hbar\Delta_{so}$ can be derived, as in App. B.2 and are (with $\hbar = 1$)

$$\Delta_0 = (\alpha^2 - \beta^2)\Delta_{so} \qquad\qquad V = \alpha\beta\Delta_{so}\,. \tag{3.3}$$

Taking into account the spin-orbit coupling in the dynamics of the system allow to use the manifold $|S\rangle - |T\rangle$ as a gateway to realize the wanted population transfer $|1\rangle \to |T\rangle$. In our work, we use the same experimental values found in [79], that are $\Delta_{so} = 2\pi \cdot 0.75$ GHz or equivalently $4.71\ \mathrm{ns}^{-1}$, $\alpha^2 = 0.87$, $\beta^2 = 0.13$ and Rabi frequencies $\Omega_p = 0.24\ \mathrm{ns}^{-1}$ and $\Omega_c = 3.8\ \mathrm{ns}^{-1}$. Then, the system is governed by the four-level Hamiltonian written in the basis $\{|1\rangle, |S\rangle, |T\rangle, |2\rangle\}$

$$H^{(4)} = \begin{pmatrix} \delta_p + \Delta_{so} & \alpha\Omega_p/2 & -\beta\Omega_p/2 & 0 \\ \alpha\Omega_p/2 & \Delta_{so} & 0 & \beta\Omega_c/2 \\ -\beta\Omega_p/2 & 0 & 0 & \alpha\Omega_c/2 \\ 0 & \beta\Omega_c/2 & \alpha\Omega_c/2 & -\delta_c \end{pmatrix}, \tag{3.4}$$

where all the elements have been introduced before in this section. The levels $|S\rangle$ and $|T\rangle$ have a very short life times that are represented by the two parameters $\Gamma_S = 0.06\ \mathrm{ns}^{-1}$ and $\Gamma_T = 0.1\ \mathrm{ns}^{-1}$.

While in [79, 84] the author studied the system in the Autler-Townes regime, which means $\delta_c \approx 0$, in our work we explored two regimes: the first, is obtained by supposing $|\delta_c| \gg \Omega_c$, so that the state $|2\rangle$ can be adiabatically eliminated obtaining, in this way, an effective three-level problem (the procedure is shown later in Sec. 3.4); the second one, is in the Autler-Townes regime with δ_c comparable with Ω_c. In this latter case, the complete four-level system must be studied and, obviously, the treatment is more complicated than in the first case.

3.3 ADIABATIC PROTOCOLS

For realizing the wanted population transfer $|1\rangle \to |T\rangle$ we resort to the generalized idea of the Landau-Zener (LZ) model [53, 56–58, 89] assuming δ_p a time-dependent function, which reads as

$$\delta_p(\tau) = a f(\tau)\,, \tag{3.5}$$

where $a = 10\ \mathrm{ns}^{-1}$ and the dimensionless sweep functions $f(\tau)$ have been defined in the Ch. 2. In particular, in this chapter we will use the driving functions (i), (iii) and (iv) of Eqs. (2.36), (2.38) and (2.39) respectively. The LZ is chosen since its the simplest ramp derived from the Landau-Zener problem. Then, unlike the LZ sweep which has a constant rate during the entire evolution, the ATAN has a non linear shape, being very fast before the avoided crossing and very slow after it. As we will see, this feature will produce better performance than the LZ one. This has been specifically designed such that a second avoided crossing is not created. The latter sweep, the RC, as mentioned in Sec. 2.3, is designed by optimizing the local adiabaticity condition (further detail are shown in App. A.1). This results in a very fast evolution far away from the avoided crossing and a very slow one in its vicinity. As we will see, this produces the best performance among the three protocols. In the following simulations, we fix the parameter $f_0 = 1$ and we use the change of variable $\alpha_\Omega = \frac{2a}{\beta\Omega}$.

For measuring the efficiency of the population transfer, we define the fidelity as

$$\mathcal{F} = |\langle T|\psi(t = t_f)\rangle|^2 , \tag{3.6}$$

where $|\psi(t = t_f)\rangle$ is the state of the system at the end of the evolution, that is at time t_f.

We will see that, the very fast decay rate of the target state $|T\rangle$ represents a problem for our adiabatic (slow) evolution. The solution to this is the application of the CD protocol, introduced in Sec. 2.2, which speed up the adiabatic evolution.

In the following, we investigate the sweep functions first in the simpler reduced three level system and then in the complete four-level one. In both cases, we study the accelerated evolution and the standard adiabatic one.

3.4 REDUCED THREE-LEVEL SYSTEM

As mentioned before, the complex molecular model presented in Sec. 3.2 can be reduced to an effective three-level one by adiabatically eliminating the state $|2\rangle$. In this section, we indeed study such a case which is simpler with respect to the four-level system.

For the purpose, we consider $|\delta_c| \gg \Omega_c$ such that the state $|2\rangle$ is not involved in the evolution anymore. In this regime, the state $|2\rangle$ can be adiabatically eliminated using the standard adiabatic elimination procedure studied, e.g., in [90] and shown in the following lines. Starting from the matrix in Eq. (3.4), we can write the corresponding differential equations for the time dependent coefficients with $\hbar = 1$

$$\begin{cases} i\dot{C}_1 = (\delta_p + \Delta_{so})C_1 + \alpha\frac{\Omega_p}{2}C_S - \beta\frac{\Omega_p}{2}C_T \\ i\dot{C}_S = \alpha\frac{\Omega_p}{2}C_1 + \Delta_{so}C_S + \beta\frac{\Omega_c}{2}C_2 \\ i\dot{C}_T = -\beta\frac{\Omega_p}{2}C_1 + \alpha\frac{\Omega_c}{2}C_2 \\ i\dot{C}_2 = \beta\frac{\Omega_c}{2}C_S + \alpha\frac{\Omega_c}{2}C_T - \delta_c C_2 \rightarrow \dot{C}_2 = 0 \Rightarrow C_2 = \frac{\Omega_c}{2\delta_c}\left(\beta C_S + \alpha C_T\right) . \end{cases} \tag{3.7}$$

Starting from $|1\rangle$ and recalling that $|\delta_c| \gg \Omega_c$, the state $|2\rangle$ remains essentially unpopulated. In this way, we can impose that its population does not change in time and we can find the condition for C_2, highlighted in red in Eq. (3.7). Now, plug the expression of C_2 into the other coefficients, we obtain

$$\Rightarrow \begin{cases} i\dot{C}_1 = (\delta_p + \Delta_{so})C_1 + \alpha\frac{\Omega_p}{2}C_S - \beta\frac{\Omega_p}{2}C_T \\ i\dot{C}_S = \alpha\frac{\Omega_p}{2}C_1 + \Delta_{so}C_S + \beta\frac{\Omega_c^2}{4\delta_c}\left(\beta C_S + \alpha C_T\right) \\ i\dot{C}_T = -\beta\frac{\Omega_p}{2}C_1 + \alpha\frac{\Omega_c^2}{4\delta_c}\left(\beta C_S + \alpha C_T\right) \end{cases} \tag{3.8}$$

$$\Rightarrow \begin{cases} i\dot{C}_1 = (\delta_p + \Delta_{so})C_1 + \alpha\frac{\Omega_p}{2}C_S - \beta\frac{\Omega_p}{2}C_T \\ i\dot{C}_S = \alpha\frac{\Omega_p}{2}C_1 + (\Delta_{so} + \beta^2\frac{\Omega_c^2}{4\delta_c})C_S + \alpha\beta\frac{\Omega_c^2}{4\delta_c}C_T \\ i\dot{C}_T = -\beta\frac{\Omega_p}{2}C_1 + \alpha\beta\frac{\Omega_c^2}{4\delta_c}C_S + \alpha^2\frac{\Omega_c^2}{4\delta_c}C_T \end{cases} \tag{3.9}$$

The latter equation can be written in matrix form so that we obtain the effective three level matrix describing the reduced system in the basis $\{|1\rangle, |S\rangle, |T\rangle\}$

$$H^{(3)} = \begin{pmatrix} \delta_p + \Delta_{so} & \alpha\frac{\Omega_p}{2} & -\beta\frac{\Omega_p}{2} \\ \alpha\frac{\Omega_p}{2} & \Delta_{so} + \beta^2\frac{\Omega_c^2}{4\delta_c} & \alpha\beta\frac{\Omega_c^2}{4\delta_c} \\ -\beta\frac{\Omega_p}{2} & \alpha\beta\frac{\Omega_c^2}{4\delta_c} & \alpha^2\frac{\Omega_c^2}{4\delta_c} \end{pmatrix}. \tag{3.10}$$

In this representation, the light-shift of the level $|T\rangle$ induced by the Autler-Townes process is evidently

$$\delta_{ls} = \alpha^2\frac{\Omega_c^2}{4\delta_c}, \tag{3.11}$$

which in this case is small since $|\delta_c| \gg \Omega_c$. It is worth noting that by neglecting the small "second order" terms proportional to β^2, α^2 and $\alpha\beta$, we obtain the same matrix of Eq. (5) in [73]. Now, we can study such a system using the adiabatic protocols introduced above.

3.4.1 *Adiabatic and Counterdiabatic Evolution*

As mentioned in Sec. 3.3, we want to realize the quantum state transfer $|1\rangle \to |T\rangle$ by using different temporal profiles for the probe detuning δ_p. Figure 3.2 shows the instantaneous eigenvalues, as a function of the rescaled time t/t_f, for the three chosen sweep functions that we have introduced in Sec. 3.3. In particular, in Fig. 3.2(a) the LZ ramp is represented and two avoided crossings, the first $|1\rangle - |T\rangle$ occurring at $t/t_f \approx 0.25$ and the second $|1\rangle - |S\rangle$ at $t/t_f \approx 0.5$, are visible. Since we are interested only in the first one, the sweep function can be terminated before the second. This problem is discussed in detail in App D. In Fig. 3.2(b), instead, the ATAN sweep is optimized, with the parameters $c_2 = 20$ (dimensionless) and $c_3 = 19.2$ ns^{-1}, such that only the first avoided crossing, around $t/t_f \approx 0.45$, between $|1\rangle$ and $|T\rangle$ is generated. Finally, the third case in Fig. 3.2(c) is represented by the RC sweep. Also in this case we observe only the wanted avoided crossing created very early in time and we will see that its performance are the best one. We recall that the temporal shape of the three sweep functions is depicted in Fig. 2.4.

The drawback of all the three adiabatic driving protocols is the very long time required for reaching high fidelities. For this reason we also introduce

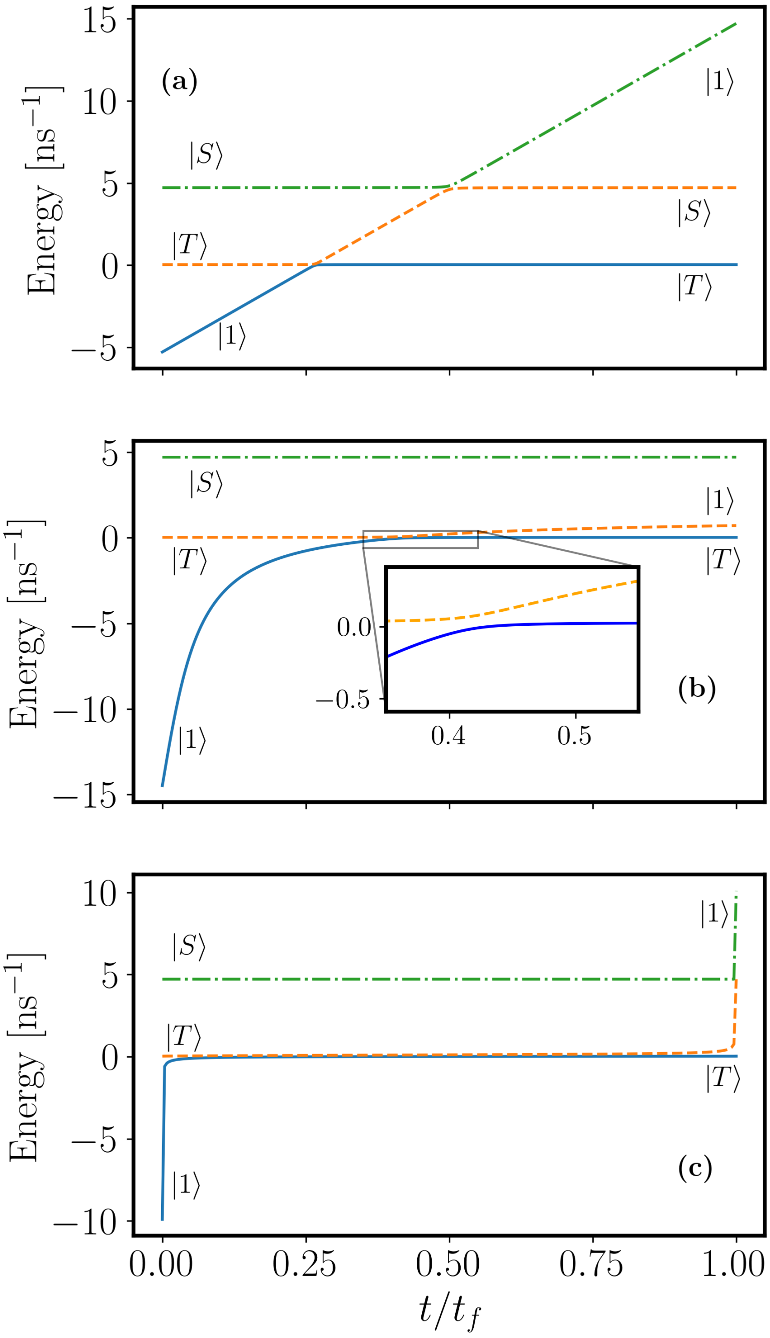

Figure 3.2: Instantaneous eigenvalues as a function of rescaled time for the three driving functions in the case of the reduced three-level model. (a) LZ sweep of Eq. (2.36) creates two avoided crossing, $|1\rangle - |T\rangle$ and $|1\rangle - |S\rangle$. However, we are interested only in the first one and we would like to have the state $|S\rangle$ unpopulated. (b) ATAN sweep of Eq. (2.39) with $c_2 = 20$ and $c_3 = 19.2$ ns^{-1}. Such a sweep function is designed ad-hoc in order to avoid the creation of the second avoided crossing with the state $|S\rangle$. (c) Similar to the case in (b), the RC sweep, with $c_1 = 4.68$ ns^{-1}, generates only the wanted avoided crossing $|1\rangle - |T\rangle$. In each figure, the three instantaneous eigenvalues are represented by the solid/blue line, dashed/orange line and dash-dot/green line. In the three figures we can distinguish the starting eigenstates on the left and the final one on the right. Other simulation parameters are $a = 10$ ns^{-1}, $\delta_c = 30$ ns^{-1}. (Figure adapted from [91])

the CD correction in order to accelerate the adiabatic evolution and to obtain very high fidelity in a time that is shorter than the life time $1/\Gamma_T$ of the target state $|T\rangle$. In the following, we will compare the two results.

3.4.2 *Results*

In the previous section we have introduced the three adiabatic protocols that we used to perform the population transfer $|1\rangle \rightarrow |T\rangle$. Here, instead, we show the comparison of their performance in the case of the standard adiabatic dynamics and of the accelerated one with the CD correction.

Figure 3.3 shows the populations of the three states $|1\rangle$, $|S\rangle$ and $|T\rangle$ for the three chosen sweep functions. In particular, in Fig. 3.3(a) we the LZ case is depicted. It has the worst performance with respect to the other protocols, reaching a fidelity around 50% with a total evolution time of $t_f = 1000$ ns. It presents also coherent oscillations between the states $|1\rangle$ and $|T\rangle$ due to the early termination of the LZ function, before the second avoided crossing (see App. D for details). Figure 3.3(b) shows the populations for the ATAN protocol. It reaches better fidelities than the LZ case, with a value around 98%. This is the result of the optimization of the ATAN function by means of the parameters $c_2 = 20$ (dimensionless) and $c_3 = 19.2$ ns^{-1}. In the latter, Fig. 3.3(c), the populations corresponding to the RC function are shown. We see that, its almost constant rate around the avoided crossing, represented in Fig. 3.2(c), generates a linear behavior in the populations change. Additionally, the fidelity reached in this case is approximately 99.97%, producing the best performance among the driving protocols that we have studied.

Although the fidelity has been improved, the adiabatic protocols discussed above require a very long total evolution time, $t_f = 1000$ ns in the case of Fig. 3.3. Therefore, in order to accelerate the evolution and eliminating all the non adiabatic transitions between the eigenstates, we resort to the CD correction term. Using the Hamiltonian H_{CD} introduced in Sec. 2.2, we obtain the populations shown in Fig. 3.4. As we can appreciate, the three sweep functions, LZ in Fig. 3.4(a), ATAN in Fig. 3.4(b) and RC in Fig. 3.4(c), reach fidelities very close to 1. The total evolution time used in these simulations is $t_f = 1$ ns, confirming the reduction of the time required to reach high fidelities in the presence of the CD term. Additionally, the oscillations that were present in the Fig. 3.3, here are completely eliminated in all the three sweep functions. Once the state $|T\rangle$ has been populated, we can transfer its population to the state $|T_g\rangle$, which will be measured, either with a π pulse, or waiting a sufficient time such that it decays completely by spontaneous emission. This latter solution can be adopted only with the CD protocol, since it requires an evolution time shorter than the time decay $1/\Gamma_T \approx 10$ ns, in our case.

In the following, we investigate the three sweep functions in the case of the four level model in the similar way that we have done in this section.

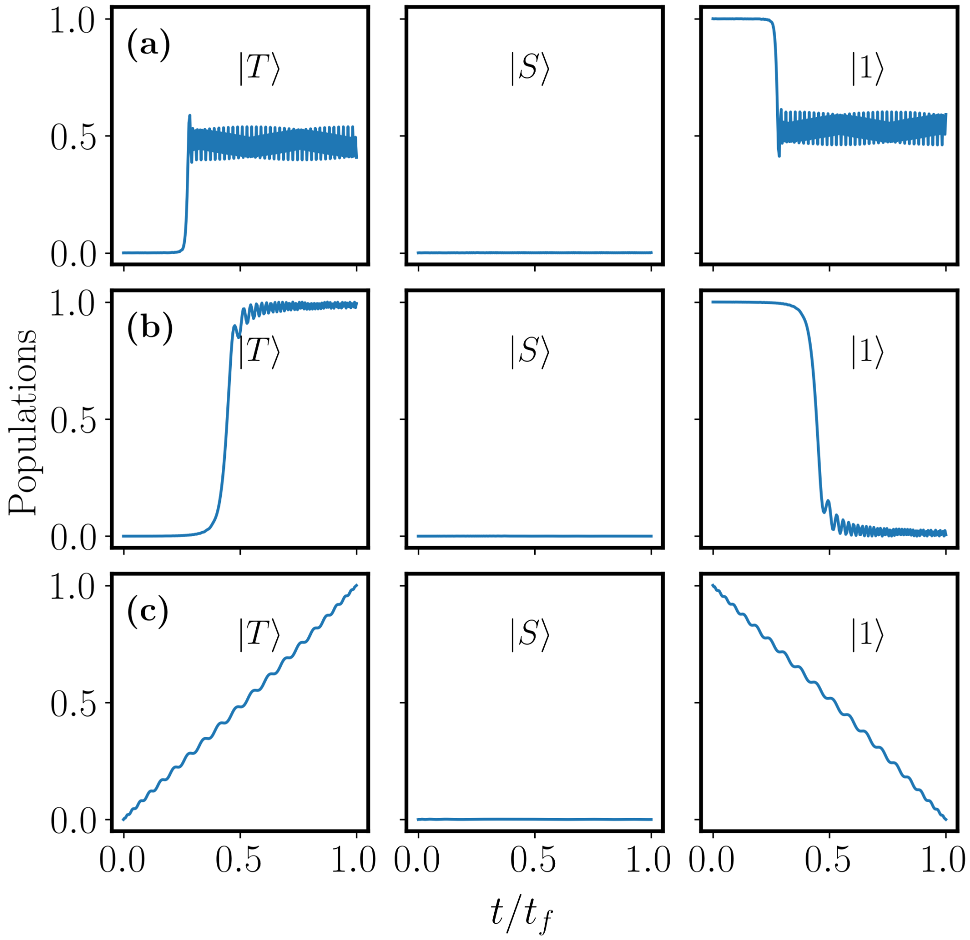

Figure 3.3: Populations of the three states in the case of the standard adiabatic evolution of the chosen sweep functions. In (a) it is represented the LZ protocol, in (b) the ATAN and in (c) the RC one. The simulations have been performed for a total evolution time of $t_f = 1000\ \text{ns}^{-1}$, much longer than the decoherence time of the state $|T\rangle$. At that fixed evolution time, the LZ sweep has the worst performance reaching a fidelity slightly below 50%. The coherent oscillations observed here are discussed in App. D. The ATAN protocol reaches much higher fidelities with a value oscillating around 98%. The latter RC one, instead, is the best one with a fidelity of 99.97%. In all the three cases (a), (b) and (c), the state $|S\rangle$ remains unpopulated. Other simulations parameters are $\delta_c = 30\ \text{ns}^{-1}$, $a = 10\ \text{ns}^{-1}$, $c_1 = 4.68\ \text{ns}^{-1}$, $c_2 = 20$ (dimensionless) and $c_3 = 19.2\ \text{ns}^{-1}$. (Figure taken from [91])

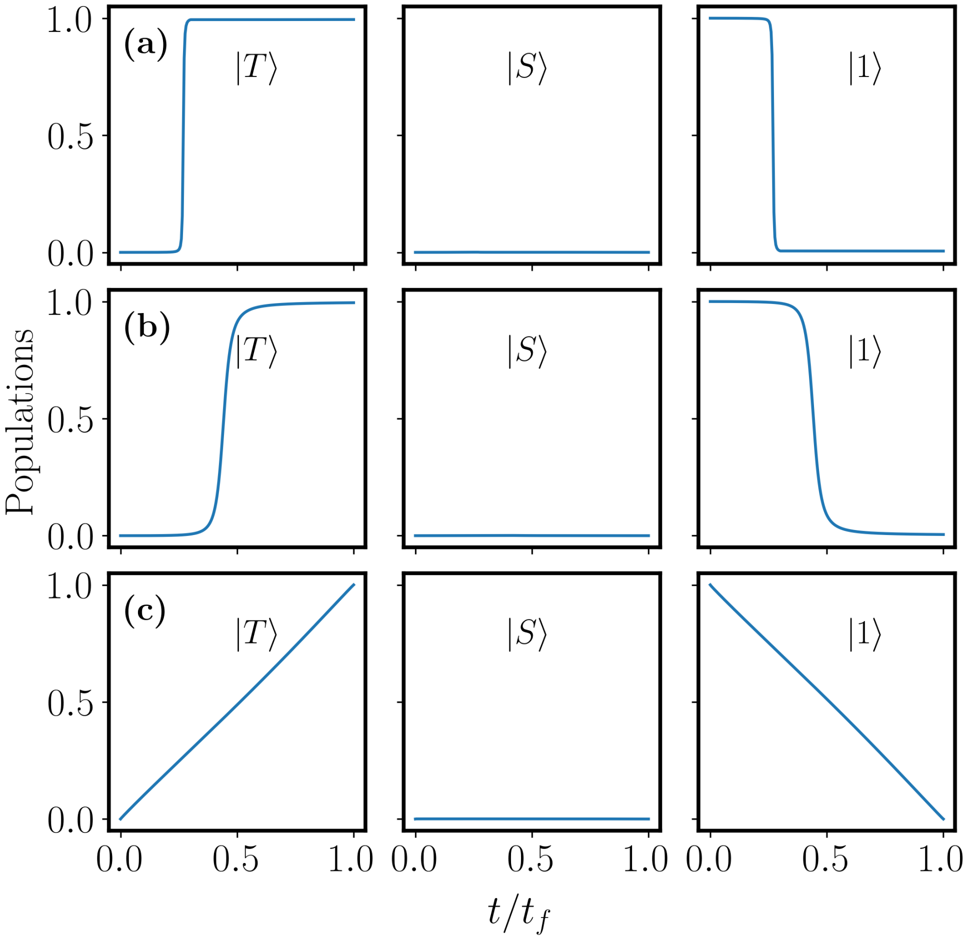

Figure 3.4: Populations of the three states in the case of the accelerated adiabatic evolution using the CD correction. As in Fig. 3.3, case (a) represents the LZ sweep, case (b) the ATAN and (c) the RC one. All the three accelerated protocols reach fidelities very close to 1 at the end of the evolution. We also notice that the oscillations visible in the Fig. 3.3, here are completely eliminated by the CD term in all the three sweep functions. In this case, the total time evolution is $t_f = 1\ \text{ns}^{-1}$, that is much shorter than the life time $1/\Gamma_T$ of the state $|T\rangle$. Other simulation parameters are the same as in Fig. 3.3.

3.5 AUTLER-TOWNES REGIME

In the section, we discuss the regime of small $|\delta_c|$, in particular when it is comparable with Ω_c. This case is part of the Autler-Townes regime which is a particular AC Stark effect realized with resonance conditions, that is $\delta_c = 0$ in this case. Here, we do not consider the exact resonant case because of the degeneracy problems that can arise in the CD term, as discussed in 2.2. Hence, we work with the value $\delta_c = 1\ \mathrm{ns}^{-1}$ such that the Autler-Townes effect cannot be neglected and the adiabatic approximation cannot be used. Therefore, the dynamics is described by Eq. (3.4). Also in this regime we study the efficiency of the population transfer $|1\rangle \to |T\rangle$ using the chosen sweep functions of Sec. 3.3.

As in the reduced model case, Fig. 3.5 shows the instantaneous eigenvalues for the three adiabatic protocols. In Fig. 3.5(a) the LZ sweep creates three avoided crossings, one with each levels. Since we are interested in the second one, in this case occurring around $t/t_f = 0.35$, the LZ ramp can be terminated before reaching the level $|S\rangle$. This produces effects similar to the one discussed in App. D. Figure 3.5(b), instead, shows the instantaneous eigenvalues for the ATAN case. Here, as in the three-level model, the anticrossing $|1\rangle \to |S\rangle$ is avoided by optimizing the parameters c_2 and c_3, which in this case are $20\ \mathrm{ns}^{-1}$ and $18\ \mathrm{ns}^{-1}$, respectively. The latter case in Fig. 3.5(c) depicts the RC sweep function which creates the long avoided crossing with $|T\rangle$ due to its very slow rate.

The standard adiabatic evolution requires evolution times longer than the life time of the state $|T\rangle$, as in the reduced model examined in Sec. 3.4.2. Therefore, in the following, we concentrate only in the CD driving.

3.5.1 *Counterdiabatic Evolution*

This section is dedicated to the strategy that we adopted for realizing the evolution with CD term. Referring to Fig. 3.5, we see that before reaching the avoided crossing $|1\rangle - |T\rangle$, we encounter the very little $|1\rangle - |2\rangle$ one. This means that using the CD correction, we will follow the solid/blue eigenvalue and we will end up in the state $|2\rangle$. Therefore, the idea is to turn on the CD term only *after* the first avoided crossing. In this way, we can *diabatically* cross the anticrossing $|1\rangle - |2\rangle$ and then we *adiabatically* follow the dashed/orange eigenvalues. This strategy is valid for the LZ and ATAN sweep functions while the RC is already optimized in order to be fast at the beginning and slow right after. In this case we will show, as example, only the accelerated ATAN protocol. In Fig. 3.6(a) we can see the population distributions after the CD evolution in the *bare* basis $\{|1\rangle, |S\rangle, |T\rangle, |2\rangle\}$ just explained. The state $|T\rangle$ reaches a fidelity of $\approx 65\%$ at the end of the evolution and this is already an improvement in controlling the spin-orbit coupling with respect to the experimental results in [79], where they obtained a fidelity of 30%. However, we also notice that a large part of the population, $\approx 33\%$, is contained in the state $|2\rangle$. This is an indication that the states $|T\rangle$ and $|2\rangle$ are coupled. This feature is not apparently visible in the instantaneous eigenvalues picture of Fig.

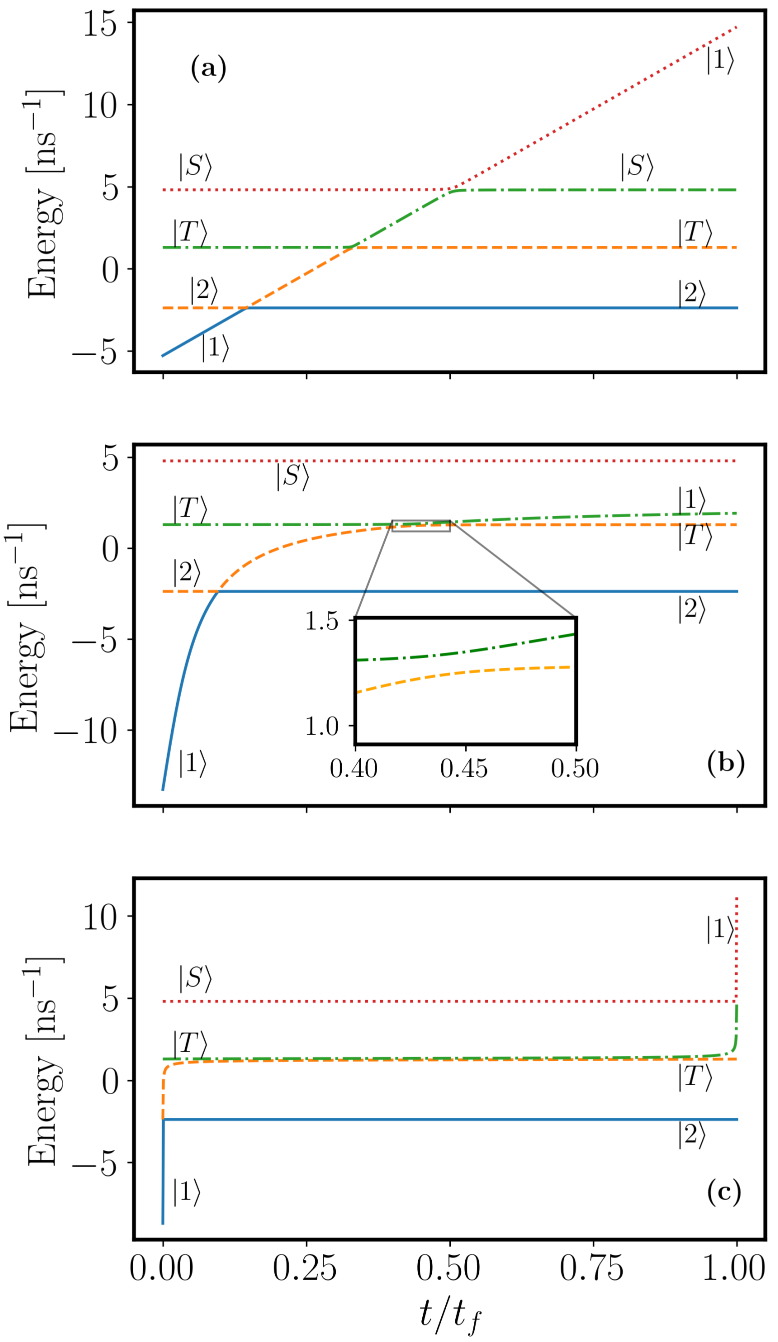

Figure 3.5: Instantaneous eigenvalues as a function of rescaled time for the three driving functions in the case of the complete four-level model. In particular, in (a) it is shown the LZ protocol, in (b) the ATAN and in (c) RC one. In each figure the four instantaneous eigenstates are denoted with the solid/blue line, dashed/orange, dash-dot/green and dotted/red one. In (a), the LZ ramp generates three avoided crossing but, as in the reduced model case, we are interested only in the $|1\rangle - |T\rangle$ one occurring approximately at $t/t_f = 0.35$, that in this case is the second one. Therefore, the sweep can be terminated before reaching the state $|S\rangle$. The ATAN protocol in (b), with $c_2 = 20$ (dimensionless) and $c_3 = 18$ ns^{-1}, creates only two avoided crossings and the $|1\rangle - |T\rangle$ occurs around $t/t_f = 0.45$. In (c), instead, with the RC sweep, with $c_1 = 3.41$ ns^{-1}, the wanted avoided crossing is created very soon after the beginning of the evolution. In these simulations $\delta_c = 1$ ns^{-1}, $a = 10$ ns^{-1}. (Figure adapted from [91])

3.1(b). However, a further confirmation can be obtained by looking at Fig. 3.7, where the imaginary part of the Berry pulses are plotted as a function of the rescaled time t/t_f. Here, we can observe two large pulses in correspondence of the avoided crossing $|1\rangle - |T\rangle$ at $t/t_f = 0.45$. They represents the CD pulses needed to compensate the non-adiabatic transitions occurring between the eigenstate that we are following and other two eigenstates. They are identified by the matrix elements $H_{CD}^{(1,3)}$ and $H_{CD}^{(1,4)}$ respectively. This means that we are preparing a state that is a superposition of the basis states, in particular $|T\rangle$ and $|2\rangle$ by looking at Fig. 3.4(a).

For this reason, we try to improve the fidelity by resorting to the following approximation. The states $|T\rangle$ and $|2\rangle$ are not eigenstate of the system. Hence, we assume that the almost resonant δ_c driving generates two eigenstates $|\pm\rangle$ that are superposition of $|T\rangle$ and $|2\rangle$

$$\begin{aligned} |+\rangle &= a|T\rangle + b|2\rangle \\ |-\rangle &= b|2\rangle - a|T\rangle\,, \end{aligned} \tag{3.12}$$

with eigenvalues

$$\lambda_{\pm} = -\frac{-\delta_c \pm \sqrt{\delta_c^2 + \Omega_c^2}}{2}\,. \tag{3.13}$$

They are found by diagonalizing the 2×2 submatrix in the bottom right angle of the matrix in Eq. (3.4). The next step is to change the old *bare* basis $\{|1\rangle, |S\rangle, |T\rangle, |2\rangle\}$, into the new *dressed* one $\{|1\rangle, |S\rangle, |+\rangle, |-\rangle\}$. Figure 3.6(b) represents the population distribution obtained from the evolution of the *bare* base and by a projective measurement onto the new *dressed* basis. The high population in the state $|+\rangle$ confirms that we were looking at the system in the wrong basis. In fact, in Fig. 3.6(a) we are mostly preparing the state $|+\rangle$, with a low population in $|-\rangle$, which is a superposition of $|T\rangle$ and $|2\rangle$ as in Eq. (3.12).

Performing the evolution in the *dressed* basis, instead, we obtain the CD pulses depicted in Fig. 3.7(b). We notice that this time only one of the pulses is large, therefore the CD driving optimized for the *dressed* basis is different from that of the *bare* basis case. In fact, population distribution of Fig. 3.8(a) shows that, unlike the evolution in the *bare* basis, the state $|T\rangle$ has a population of 97% and also that the state $|2\rangle$ is not populated. Additionally, Fig. 3.8(b) shows the population obtained by a projective measurement onto the *dressed* basis. In this case, preparing the state $|T\rangle$ in the *bare* basis means to prepare the corresponding superposition of $|+\rangle$ and $|-\rangle$.

Therefore, it is convenient studying the complete system, in the Autler-Townes regime, using the *dressed* basis. If, instead, $|\delta_c|$ is large the complete system can be investigated in the *bare* basis since it can be approximated by the reduced three-level model. In the next section, we discuss the validity of the approximation obtained by the adiabatic elimination method comparing the fidelities of the reduced model with the complete one in the large $|\delta_c|$ regime.

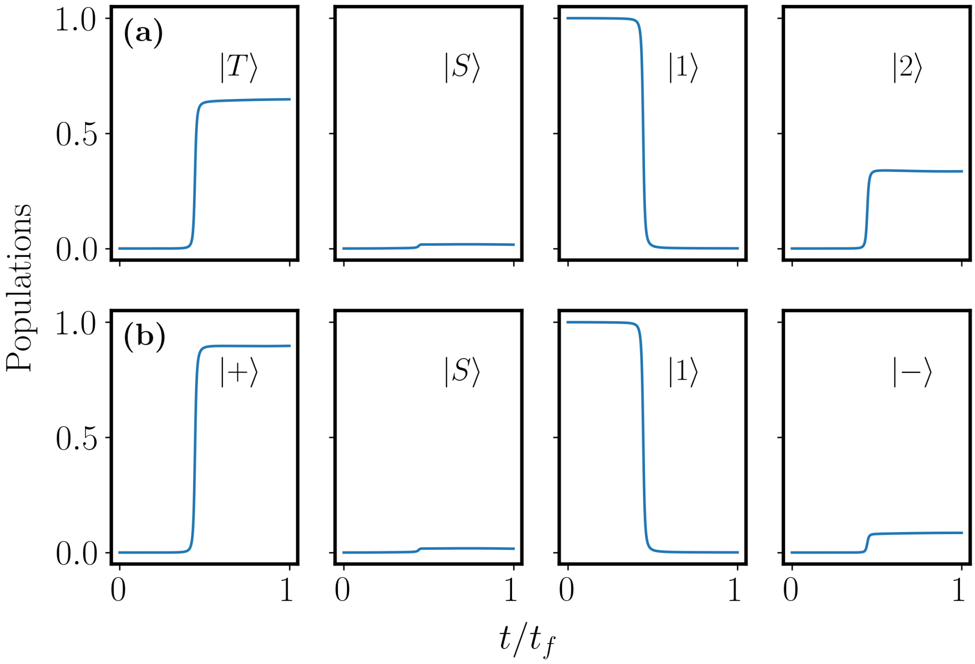

Figure 3.6: Populations of the four levels in the case of ATAN protocols accelerated with the CD driving. The evolution in these simulations is performed in the *bare* basis $\{|1\rangle, |S\rangle, |T\rangle, |2\rangle\}$. The case (a) is obtained by a projective measurement onto the bare basis. The fidelity of $|T\rangle$ is $\approx 65\%$ and population of the state $|2\rangle$ reaches $\approx 33\%$. The remaining 2% is in the state $|S\rangle$ but for our purposes it can be neglected since it is very low. Case (b), instead, is obtained with a projective measurement onto the *dressed* basis with the states of Eq. (3.12). In this case we can notice that the population is mostly in the state $|+\rangle$, confirming that it is a superposition of $|T\rangle$ and $|2\rangle$. Simulation parameters are $t_f = 1$ ns, $a = 10$ ns^{-1}, $\delta_c = 1$ ns^{-1}.

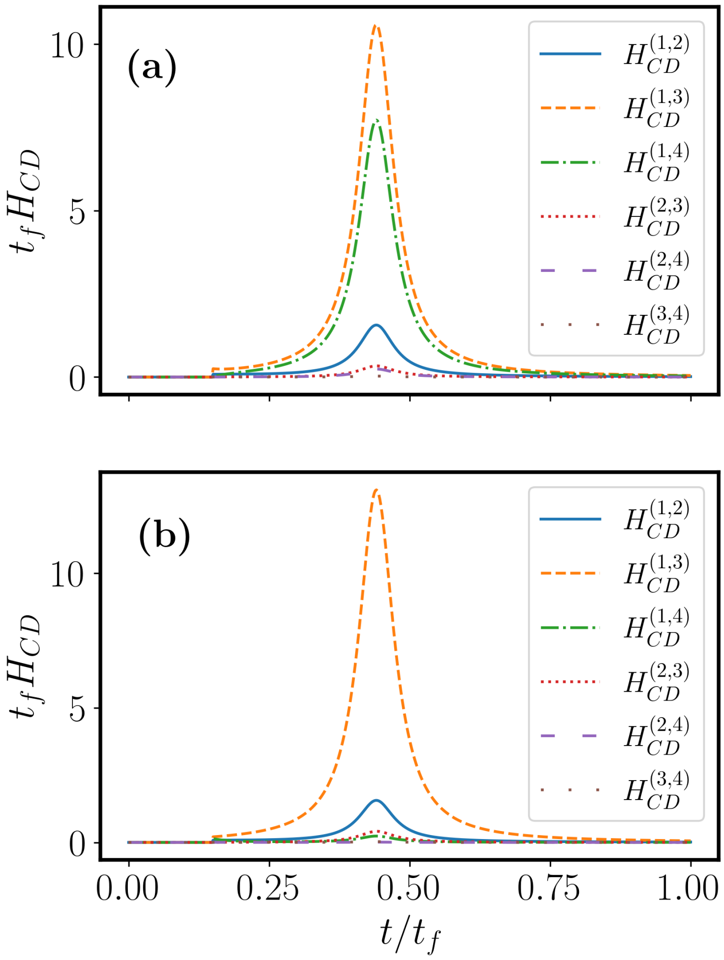

Figure 3.7: Imaginary part of the CD pulses for the matrix elements $H_{CD}^{(i,j)}$ with $i, j = 1, 2, 3, 4$ in the case of ATAN sweep. The CD driving is applied after the threshold time $t/t_f = 0.15$ such that the first avoided crossing is *diabatically* crossed. The peaks are in correspondence of the avoided crossing $|1\rangle - |T\rangle$ occurring at $t/t_f = 0.45$. In (a), the three pulses dashed/orange, dash-dot/green and solid/blue are evaluated for the evolution with the *bare* basis $\{|1\rangle, |S\rangle, |T\rangle, |2\rangle\}$, and they corresponds to the matrix elements $H_{CD}^{(1,3)}, H_{CD}^{(1,4)}$ and $H_{CD}^{(1,2)}$ in ascending order. This is an indication that the eigenstates we are following is mostly coupled with two other eigenstates. In (b), instead, the same pulses are computed from the evolution with the *dressed* basis $\{|1\rangle, |S\rangle, |+\rangle, |-\rangle\}$. Although the shape is the same, the peak height is different from the case (a) and in this case only one peak is relevant. Simulations parameters are $\delta_c = 1$ ns^{-1}, $a = 10$ ns^{-1}.

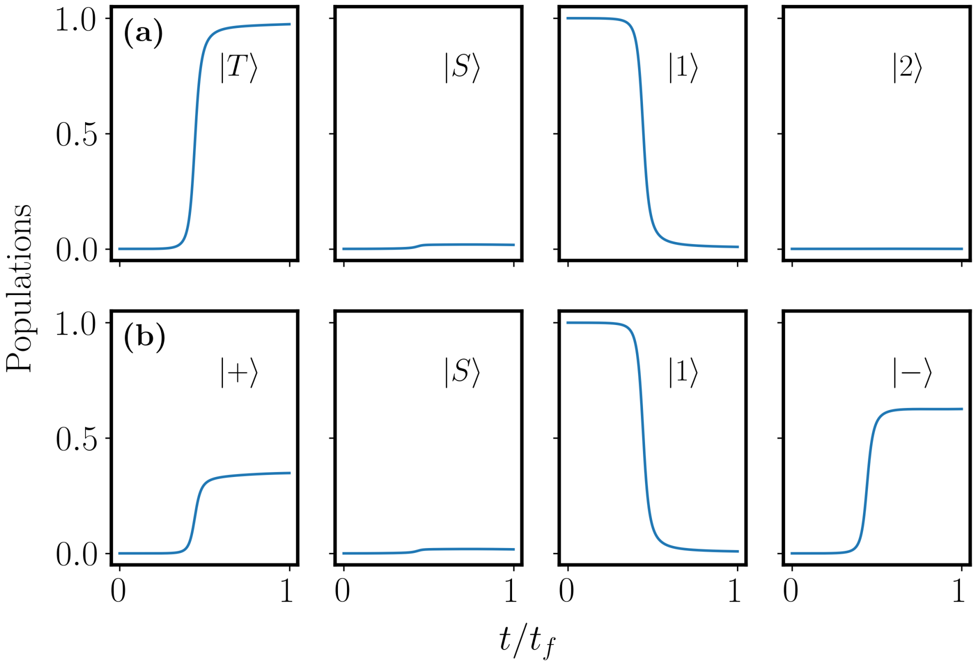

Figure 3.8: Populations of the four levels in the case of ATAN protocols accelerated with the CD driving. The evolution in these simulations is performed in the *dressed* basis $\{|1\rangle, |S\rangle, |+\rangle, |-\rangle\}$. The case (a) is obtained by a projective measurement onto the bare basis. The fidelity of $|T\rangle$ is $\approx$ 97% and the state $|2\rangle$ is essentially unpopulated. The remaining population is in the state $|S\rangle$ but for our purposes it can be neglected since it is very low. Case (b), instead, is obtained with a projective measurement onto the *dressed* basis with the states of Eq. (3.12). In this case we can notice that the state of the system at the end of the evolution is a superposition of $|+\rangle$ and $|-\rangle$. This confirms that the state $|T\rangle$, found in (a), is a their superposition. Simulation parameters are $t_f = 1$ ns, $a = 10$ ns^{-1}, $\delta_c = 1$ ns^{-1}.

3.6 VALIDITY OF THE ADIABATIC ELIMINATION

In the Sec. 3.4, we have studied the effective three-level system in the regime $|\delta_c| \gg \Omega_c$. In this section, we answer the question about the minimum value of δ_c to use in order to satisfy the adiabatic elimination condition. We compare the approximation using three different values of δ_c, that are $10, 30, 100$ ns^{-1}. In Fig. 3.9, we can see the fidelities of the three sweep functions as a function of the total evolution time t_f. Figure 3.9(a) corresponds to the case $\delta_c = 10$ ns^{-1} and we can observe that the adiabatic elimination approximation does not approximates very well the complete system, especially in the ATAN case. This is due to the fact the adiabatic elimination condition mentioned above is weakly satisfied. In fact, increasing the value of δ_c, we see that the approximation becomes better and better for the cases $\delta_c = 30$ and $\delta_c = 100$ ns^{-1} which is the best one. In Sec. 3.4, we have shown the results for the case with $\delta_c = 30$ ns^{-1}, which is a good approximation, but other larger values can be used, e.g., $\delta_c = 100$ ns^{-1} as in Fig. 3.9(c).

3.7 APPROXIMATION OF THE COUNTERDIABATIC DRIVING

In the previous sections, we have taken for granted that the CD fields needed for speed up the evolution, can all be experimentally realized. However, introducing many extra term in a Hamiltonian, especially for a complex multilevel system is not an easy task. Therefore, in this section, following the approach in [56], we resort to an effective CD driving. The objective is to reduce the number of matrix elements needed for reaching high-fidelity levels in a very short time. We consider, as exemplary case, the CD ATAN protocol for the reduced three-level system of Sec. 3.4.2, but the same idea can be applied for other sweep.

Let us consider the Berry pulses of Fig. 3.10(a) related to matrix elements of the CD field for the ATAN sweep function in the three-level system. The application of such a correction produces the infidelity, as function of time, corresponding to the circled solid blue line of Fig. 3.10(b). However, by looking at the pulses of Fig. 3.10(a), we notice that the pulse corresponding to the matrix element $H_{CD}^{(1,3)}$ is much larger than the others. Hence, we neglected the two pulses corresponding to the elements $H_{CD}^{(2,3)}$ and $H_{CD}^{(1,2)}$ and we obtain the square orange curve and the triangles green one of Fig. 3.10. The first is obtained by evolving the system eliminating only the $H_{CD}^{(2,3)}$ term and the second one by removing both the small pulses $H_{CD}^{(2,3)}$ and $H_{CD}^{(1,2)}$. The results show that in both cases the approximation does not degrade the performance in an appreciable way. Therefore, in this case, in a real physical implementation, we can realize only one pulse instead of three without losing the high fidelity regime, and simplify in this way the additional experimental cost.

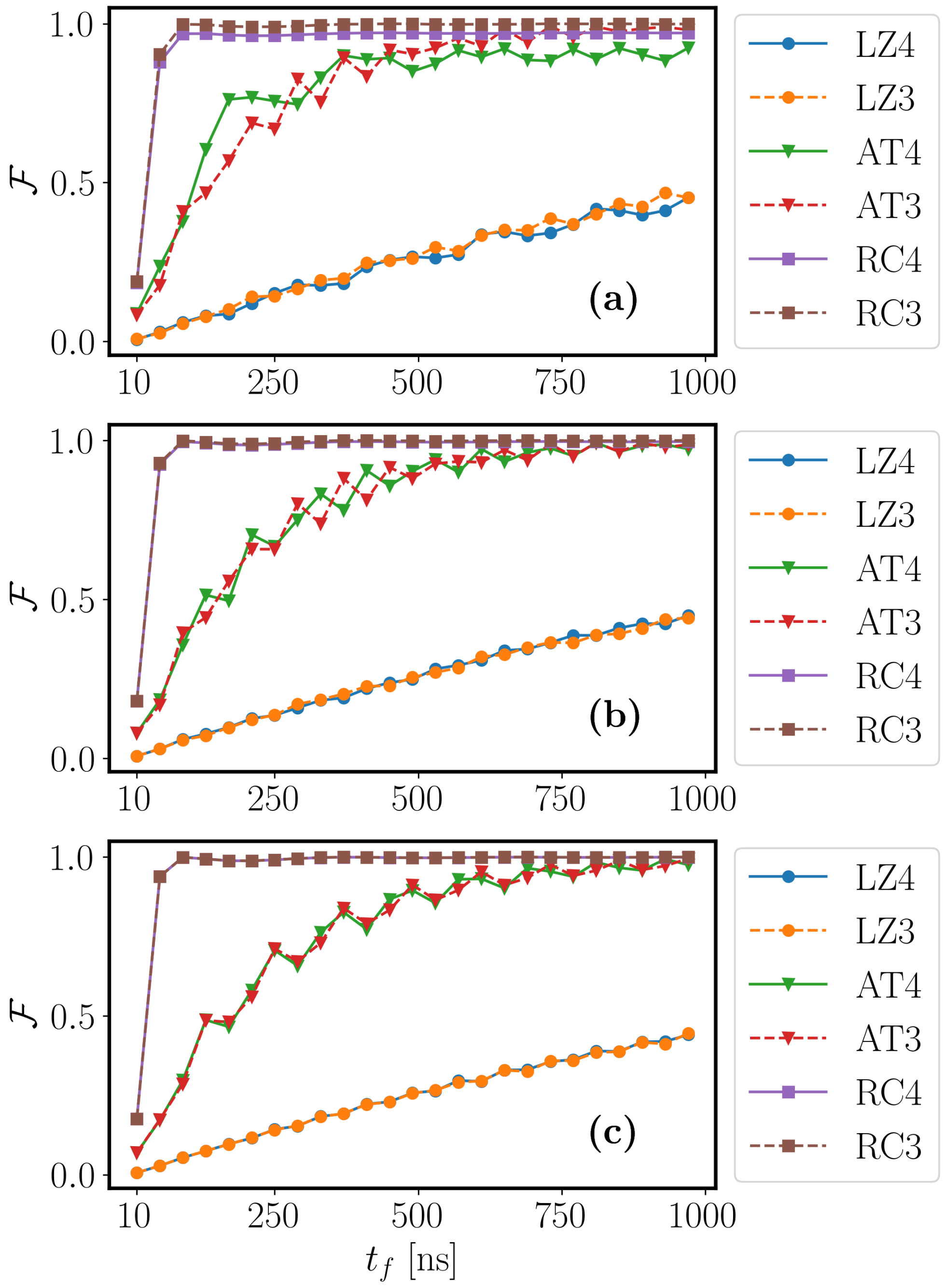

Figure 3.9: Comparison between fidelities of the three sweep functions LZ, ATAN and RC, as a function of the total evolution time t_f, for (a) $\delta_c = 10$ ns^{-1}, (b) $\delta_c = 30$ ns^{-1} and (c) $\delta_c = 100$ ns^{-1}. In all the three plots, the reduced three level system is identified by the dashed lines, while the complete one by the solid lines. Additionally, each sweep function is denoted with different markers, circles for the LZ, triangles for the ATAN and squares for RC. The δ_c driving modifies the energy splitting between the states $|T\rangle$ and $|2\rangle$ and consequently also the avoided crossing. Therefore, the parameters c_1, c_2 and c_3 have been optimized in order to approximately obtain the same type of avoided for the reduced system and the complete one. The case in (a) is the worst approximation among the three chosen values of δ_c, since it considers a small value of δ_c and the adiabatic elimination condition $|\delta_c| \gg \Omega_c$ is weakly satisfied. Then, as the value of δ_c increases, we see that also the approximation becomes better and better, as shown in the cases (b) and (c). Other simulation parameters are the same as in the other figures.

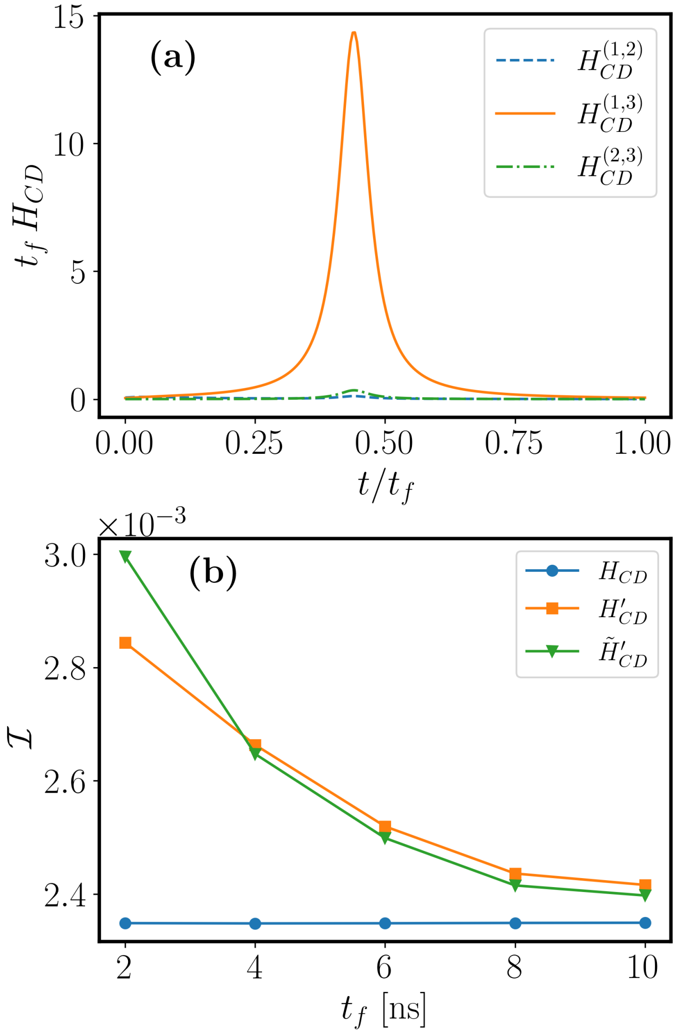

Figure 3.10: (a) Imaginary part of the CD pulses for the ATAN protocol in the reduced model of Sec. 3.4. The important feature is the fact that the pulse related to the matrix element $H_{CD}^{(1,3)}$ is more relevant for the good realization of the CD driving. Parameters are $\delta_c = 30$ ns^{-1}, $c_2 = 20$ (dimensionless) and $c_3 = 19.2$ ns^{-1}. (b) represents the infidelity of the accelerated ATAN protocol. The blue line with circles is obtained by the evolution of the complete set of CD pulses of Fig. 3.10. The orange line with squares is obtained by evolving the system without the $H_{CD}^{(2,3)}$ term, while the latter green curve with triangles represents the case without both the elements $H_{CD}^{(1,2)}$ and $H_{CD}^{(2,3)}$. Thus, removing the non relevant pulses does not produce any significant change in the fidelity. (Figure taken from [91])

3.8 REMARKS

This chapter was dedicated to the optimization of a population transfer in a simplified multi-level system, using our quantum control tools introduced in Ch. 2. In Sec. 3.2 we have studied the level structure of the system with all the physical quantities required for our purpose and we have introduced the matrix describing its dynamics. Then, in Sec. 3.3 we have defined the adiabatic protocols that we have chosen to realize the wanted population transfer. We have seen that the problem can be studied in its natural complete four-level description and also in a simplified three-level version by adiabatically eliminating one of the levels. This latter case, has been discussed in Sec. 3.4 where the fidelities of the chosen sweep functions have been shown. We observed that the simple LZ protocol has the worst performance and therefore other sweep functions have been implemented. In particular, the optimized ATAN and RC driving functions can produce much better fidelity. However, the very slow adiabatic evolution is in contrast with the typical short life time of the target state. Therefore, we resort to the CD theory introduced in Sec. 2.2 to accelerate the adiabatic evolution and reaching fidelities very close to 1 in a very short time. In Sec. 3.5, instead, the complete system was investigated. In this case, we directly studied the accelerated version of the adiabatic protocols. We have seen that, although the fidelity was doubled with respect to the experimental one [79], a proper change of basis can improve the performance. This is possible because of the different optimization of the CD driving which depends on the chosen basis. We showed this for the ATAN function but the same idea holds also for the other sweep protocols. After that, we dedicated a short section, Sec. 3.6, to compare different regimes of validity of the adiabatic elimination approximation used before in Sec. 3.4. We have seen that for sufficiently large δ_c, the performance of the reduced system matched very well those of the complete one. Finally, we dedicated the next section to the discussion of the experimental realization of the CD protocol. We have used the idea in [56] to reduce the number of CD pulses to be realized experimentally, such that the fidelity would not be significantly affected. The results showed that, in the case of the ATAN sweep for the reduced model, we could reduce from three to one the pulses needed for an optimal accelerated adiabatic evolution.

Our study has shown that it is possible to optimize the quantum control strategies to improve the performance of a specific quantum operation in complex scenarios. In our case, the fidelity reached in the experiment was about 30% but using our tools we were able to reach very high fidelities, $> 97\%$, in both the reduced and complete scheme.

4

NOISY SHORTCUT TO ADIABATICITY

As we have seen in the previous chapters, one of the most used quantum control technique is the adiabatic control [18, 19]. The method allows to reach a target state, at time t_f, of the Hamiltonian $H_0(t_f)$ starting from an eigenstate of the initial Hamiltonian $H_0(t_0)$ and slowly following the instantaneous eigenstate. We have seen that this type of control, although it is very powerful, for optimal performance it requires ideally infinite evolution time, which is unfeasible in a real experimental implementation. For this reason, by evolving the system in a finite time we introduce errors and imperfections in the evolution, as presented, e.g., in Sec. 2.1.1 and in particular in Fig. 2.2. For this reason, protocols for optimizing the finite evolution have been designed [53–55]. We have already presented, in Sec. 2.3, the adiabatic protocols that we have chosen for the analysis in this thesis. Despite the optimization of the sweep functions, the evolution time might be still longer with respect to the typical coherence times of a quantum system. Therefore, we have introduced, in Sec. 2.2, the CD protocol for accelerating the evolution and reaching fidelities, ideally, 1. Indeed, in the previous Ch. 3 we have seen an application of the CD to improve the efficiency of a population transfer, counteracting also the limitation of the very short life time of the level of interest. However, the control of a quantum system is not a perfect operation but rather it is affected by many sources of errors and noise. In this direction, similar studies have been performed in open quantum systems scenario [92–94] or in experimental setup [95]. In contrast, in this chapter, we aim at studying the behavior of different adiabatic protocols accelerated with the CD theory of Sec. 2.2, subjected to noise and decoherence channels. For the purpose, we investigate two systems configurations: two-level one, in Sec. 4.2, and a four-level one in the form of two qubit entangling gate, in Sec. 4.3. For both cases, we first analyze static errors in the control parameters and then we introduce dissipative and dephasing phenomena, typical of an open quantum system scenario. In the end, will be able to indicate which sweep function is most robust, under the CD evolution, depending on the type of decoherence channels.

4.1 THEORETICAL BACKGROUND

In this first section, we briefly recall the theoretical basis introduced before in Ch. 2. In particular, we will provide further detail about three of the four sweep functions presented in Sec. 2.3 and about the Lindblad evolution already introduced in Sec. 2.4.

4.1.1 *Adiabatic protocols*

One of the key ingredients for our study is the adiabatic protocol driving the system. Among those presented in Sec. 2.3, here we choose to work with the LZ (i), PL (ii) and RC (iii), since they belong to three different families of sweep functions. As already explained in Sec. 2.3 and Ch. 3, the ATAN(iv) is optimized for the specific requirements of the problem and here it is not taken into account. The three sweep functions are applied to a generic system which can be written in the form

$$\hat{H}_0(t) = f(t)\hat{H}_1 + \hat{H}_2\,, \tag{4.1}$$

where $f(t)$ represents the sweep function and $\hat{H}_1$ and $\hat{H}_2$ describe the dynamics of the system. For the one qubit case they reproduce the system we have already seen in Ch. 2, i.e., $\hat{H}_1 = \alpha\hat{\sigma}_z$ and $\hat{H}_2 = \Omega\hat{\sigma}_x$. Using the rescaled time and units that we have introduced in the Sec. 2.1.1 and setting $c_1 = 0$, the analytical expressions of the three sweep functions are the same defined Sec. 2.3. The two qubits model, instead, realizes a similar implementation of the entangling gate in [56] and, therefore, this allows us to use the same sweep functions which are already optimized for the two-qubits entangling gate.

Each sweep is then accelerated using the CD protocol presented in Sec. 2.2. We will see that, for both systems presented in this chapter, the Hamiltonian H_{CD} can be computed analytically.

The evolution is governed by the Lindblad master equation of Eq. (2.43) introduced in Sec. 2.4. In particular, the problems addressed in this chapter, are typical of quantum optics where the three validity conditions are, in general, all satisfied. We, indeed, deal with a weak coupling and a non-correlation regime between the system and the environment. Additionally, the carrier frequency of the driving is much greater than the one of the phenomena taken into account. Hence, the RWA can be used as we have done previously in App. B.1.1. Details on the systems are provided in the corresponding sections.

4.2 ONE QUBIT MODEL

As we have usually done so far, one of the first example to have an initial comprehension of the phenomena occurring into the system is the two level system. In this case, the Hamiltonian reads

$$\hat{H}_0(t) = \frac{\alpha f(t)}{2}\hat{\sigma}_z + \frac{\Omega}{2}\hat{\sigma}_x \tag{4.2}$$

where α is the scaling parameter and Ω is the coupling constant, as seen in in Sec. 2.1.1. The Hamiltonian is expressed in the rotating frame of the drive and in the RWA, and it can describe, e.g., a two level system driven by a resonant electromagnetic field. Using the same variables definition that we adopted in Ch. 2, the system Hamiltonian becomes

$$\hat{H}_0(\tau) = T\left[\alpha_\Omega f(\tau)\hat{\sigma}_z + \hat{\sigma}_x\right]\,, \tag{4.3}$$

with $T = \alpha_\Omega t_f$, $\alpha_\Omega = \alpha t_f/\Omega$ and $\tau = (t - t_I)/t_f$.

For the complete description of the evolution, we need to add the CD term to the Eq. (4.3). We analytically derived $\hat{H}_{CD}$ for this case, and it has the form

$$\hat{H}_{CD}(\tau) = -\frac{\alpha_\Omega \dot{f}(\tau)}{1 + f^2(\tau)}\frac{1}{2}\hat{\sigma}_y \,. \tag{4.4}$$

This expression remind us the one that we have already found in Eq. (2.32) and (2.34) in Sec. 2.2. In Fig. 4.1(b) the matrix CD element for the three sweep are depicted. We observe the peaks where the probability of non adiabatic transitions is higher.

Thus, finally, the Hamiltonian corrected by the Berry elements to be used in the Lindblad master equation of Eq. (2.43) is then

$$\hat{H}(\tau) = \hat{H}_0(\tau) + \hat{H}_{CD}(\tau) \,. \tag{4.5}$$

In this case, the considered two level system is a well-known model used in quantum optics [47, 60] where the Lindblad formalism is suitable for its description. In particular, the system is assumed to be weakly coupled and also non-correlated with the external environment. In this way, the first two conditions for the Lindblad master equation treatment, introduced in the Sec. 2.4, are satisfied. Then, as previously mentioned in Sec. 4.1.1, the frequency of the phenomena considered here are much smaller than the driving frequency such that the RWA can be applied. Additionally, the adiabatic protocols used to drive the system are sufficiently strong to perform the population transfer but also sufficiently weak to keep valid the conditions for the Lindblad treatment. We must only be cautious not to exaggerate the driving frequency such that not to invalidate the Markovian assumption [97]. To study the system we define the two basis states, represented in basis of the eigenvector of the Pauli matrix σ_z, as $|0\rangle \hat{=} \begin{pmatrix} 0 \\ 1 \end{pmatrix}$ and $|1\rangle \hat{=} \begin{pmatrix} 1 \\ 0 \end{pmatrix}$. Assuming, then, that the system is prepared in the state $|0\rangle$, in order to measure the effects of the errors on the various adiabatic protocols, we define the fidelity as

$$\mathcal{F}_1 = |\langle \psi(\tau = 1)|1\rangle|^2 \,, \tag{4.6}$$

namely the probability of ending the evolution in the state $|1\rangle$. In Fig. 4.1(c) the fidelities generated by the corrected Hamiltonian of Eq. (4.5), without any type of perturbation, as a function of the rescaled time are plotted. We observe that the LZ and PL sweeps have a very similar behavior since they create a similar form of the avoided crossing, while the RC one is completely different. This will be crucial in the study of dephasing and spontaneous emission. The similarity between the LZ and PL fidelities can be understood from Fig. 4.2. We can notice a similar narrow (in time) avoided crossing for the LZ and PL cases in Figs. 4.2(a) and 4.2(b) respectively, and very long avoided crossing for the RC sweep of Fig. 4.2.

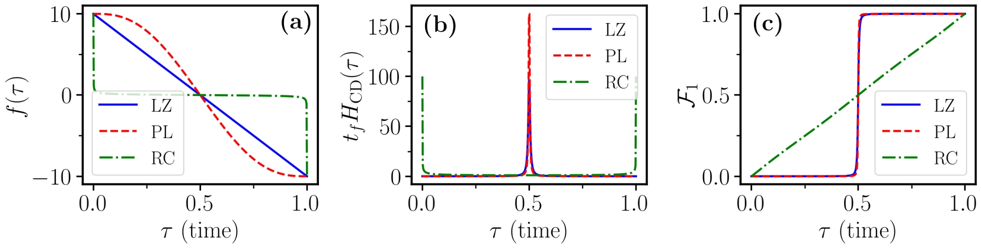

Figure 4.1: For the one-qubit case, temporal profile of (a) the three sweep functions considered. In particular Landau-Zener (LZ) (solid blue line), Polynomial (PL) (dashed red line) and Roland-Cerf (RC) (dashed dotted green line); (b) the matrix elements of the Counterdiabatic Driving (CD) term for the three sweeps; (c) fidelity in Eq. (4.6) generated by the Hamiltonian $\hat{H}(\tau)$ for the sweeps considered. Parameters of simulation are $\alpha_\Omega = 10$, $T = 10$, $f_0 = 10$. (Figure adapted from [99]).

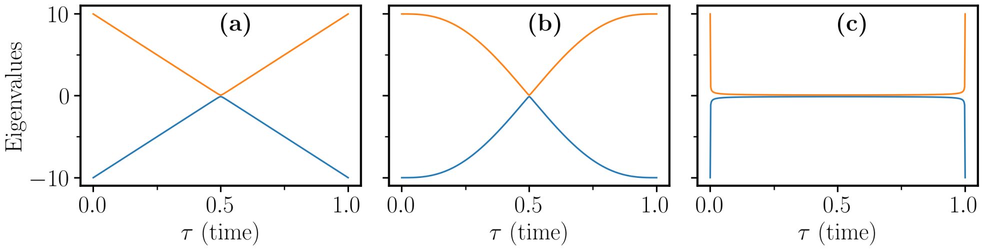

Figure 4.2: Instantaneous eigenvalues of the three sweep functions: (a) LZ, (b) PL and (c) RC. We observe that the first two have a very similar avoided crossing form around $\tau = 0.5$, which is narrow, and, therefore, the similarity is found also in the temporal shape of the fidelity as in Fig. 4.1(c). In (c), instead, the avoided crossing is very long in time and for this reason the fidelity has not a rapid change as in the other two cases. The simulation parameters are the same of Fig. 4.1.

4.2.1 *Relative parameter error*

The first problem we consider is the imperfection in the control parameters. In particular, we introduced a relative error in the parameter α_Ω in order to consider the lacking of knowledge of the coupling strength of the levels and of their initial and final energy gap. Examples of these situation can be found in experiments for controlling the collisional dynamics in cold-atom setup [100–102], where the gap of the atoms follows a broad thermal distribution and thus is subjected to a large error values. Therefore, while keeping fixed the CD Hamiltonian, we compute the fidelity for the affected parameter $\alpha_\Omega^\epsilon = \alpha_\Omega(1+\epsilon)$, where ϵ is the relative error. Figure 4.3 shows the fidelities of the three sweep functions as a function of the error ϵ and of the parameter T. We can appreciate the stability of the CD protocol with respect to the parameter error, in particular Figs. 4.3(a) and (b), corresponding to the LZ and PL drivings. They exhibit very similar behavior because of their similarities in the temporal dependence of the fidelity, as explained in the previous Sec. 4.2. In particular, the two protocols fidelities remain very stable for an error lower than 100%, whereas start decreasing for grater values of ϵ. In this

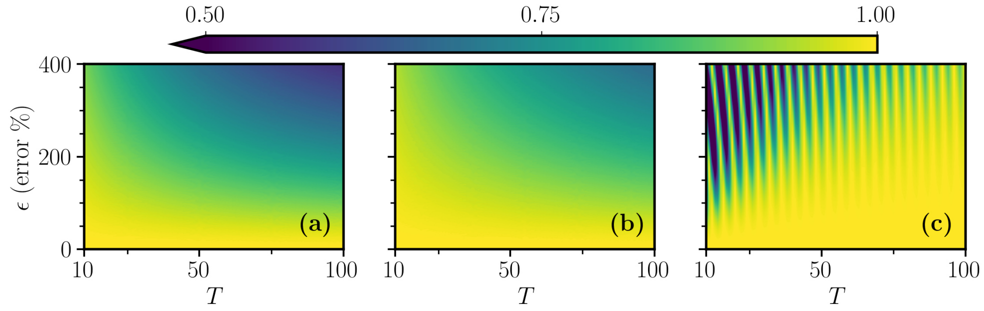

Figure 4.3: Colormap of the fidelity in Eq. (4.6) in the (ϵ, T) plane for the adiabatic protocols, with the parameter error ϵ, (a) Landau-Zener, (b) Polynomial, (c) Roland-Cerf accelerated with the Berry Counterdiabatic Driving Hamiltonian. Plots (a) and (b) have very similar behavior because their fidelity has also very similar temporal shape, as we can observe in Fig. 4.1(c). Plot (c), instead, shows typical oscillations in the fidelity [56, 58], due to the accidentally resonance that cancel high-order non-adiabatic process. Parameters simulation are $\alpha_\Omega = 10$ and $f_0 = 10$. (Figure taken from [99]).

case, the error is too large and CD field is not optimized anymore. Whereas, in Fig. 4.3(c), the RC sweep is still very stable for errors $\epsilon < 100\%$ but for greater values it is characterized by typical oscillations [56, 58] due to the accidentally cancellation of high-order non-adiabatic processes. Overall, the CD implementation is very stable, in fact, in the three protocols we need errors greater that 100% in order to have an appreciable degradation of the fidelity.

4.2.2 *Dephasing and Spontaneous Emission*

After studying the static error in the previous section, here we open the system introducing typical effects such as dephasing and decay due to spontaneous emission. For the purpose we define a collapse or jump operator as

$$\hat{c} = \sqrt{\gamma}\left[\cos(\theta)\hat{\sigma}_z + \sin(\theta)\hat{\sigma}_x\right] , \qquad (4.7)$$

where γ is the rate measured in $1/t_f$ and $\hat{\sigma}_z$ and $\hat{\sigma}_x$ the two Pauli matrices identifying the two decoherence processes. Changing the value of θ we can analyze the two limiting effects of pure dephasing for $\theta = 0$ and dephasing with population relaxation for $\theta = \pi/2$ or a mixture of the two for intermediate values of θ. A similar jump operator can be found, in general, in a quantum computing context [4]. For instance, the case with $\theta = 0$ is typical in scenarios when the interaction between the system and the environment is strongly off-resonant or it can also describe the backaction resulting from a quantum nondemolition measurement of the system state [103–105]. In our simulations, we considered values of γ typical of quantum platform such as Rydberg atoms [106] and superconducting qubits [107] that have $\gamma \propto 0.1$ and $\gamma \propto 1$, respectively, in our units.

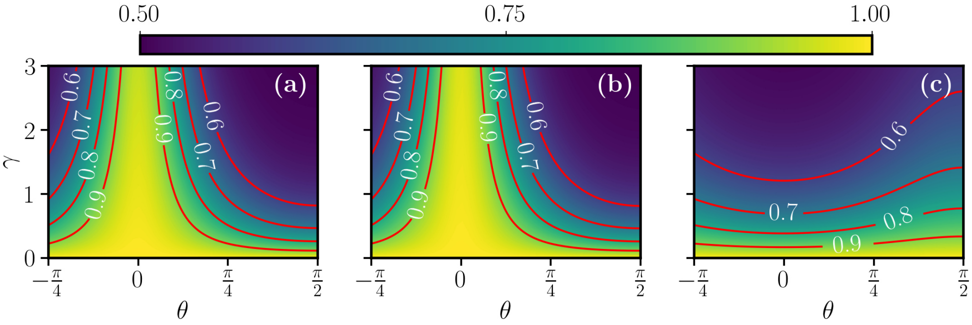

Figure 4.4: Colormap of the fidelity at the end of the evolution, as a function of θ and decay rate γ, for the three protocols (a) Landau-Zener, (b) Polynomial and (c) Roland-Cerf. The simulations are obtained by numerically solving the master equation in Eq. (2.43) with jump operator of Eq. (4.7). Figures (a) and (b) show similar behavior due to their similar temporal dependence of the fidelity (see the text for further detail). They are very stable if the system is subject to pure dephasing, that is $\theta = 0$ and $\hat{c} = \hat{\sigma}_z$ because it is very close to an eigenstate of the collapse operator $\hat{c}$. (c), on the contrary, is more stable for $\theta = \pi/2$ namely for $\hat{c} = \hat{\sigma}_x$. Other simulation parameters are the same of the Fig. 4.1. (Figure taken from [99]).

We numerically solved the Eq. (2.43) with the jump operator in Eq. (4.7) for the three sweep functions, and the results are depicted in Fig. 4.4. We first observe that the LZ protocol and the PL one, in Fig. 4.4(a) and (b) respectively, have a very similar behavior since, as in the static error case, their fidelities follow an analogous time dependence. In particular, they are very robust against pure dephasing effect. This can be understood by the fact that a $\hat{\sigma}_z$ operator induces a decay of the coherences in the density matrix but it leaves the populations unchanged. In particular, if we look at the two corresponding fidelities in Fig. 4.1(c), we notice that, the most of the evolution time, the eigenstate of the system that we follow is in one of the two basis state $|0\rangle$ or $|1\rangle$. For this reason, the pure dephasing does not affect in an appreciable way the performance of the fidelity. In other words, the linear and polynomial sweeps, generate a population transfer which is faster than the time scale $1/\gamma$ of the dephasing. However, as θ grows towards the value of $\pi/2$, the two protocols became very sensitive to the population relaxation, and in fact the fidelity fall very fast as γ increases. On the contrary, the fidelity of RC sweep function is more sensitive to the pure dephasing. Thinking in the eigenstate formalism, we are following an eigenstate of $H_0(\tau)$ which, the most of the time, is in a superposition with the basis states $a|0\rangle + b|1\rangle$. Therefore, the decay of the coherences in the density matrix strongly degrade the performance of the protocol. Such a behavior, however, allows the RC to be less sensitive to the population relaxation effect, since the population transfer is slower compared to the time scale. $1/\gamma$.

The other effect we consider in the open quantum system scenario, is the spontaneous emission which is modeled by the jump operator $\hat{c} = \sqrt{\gamma_-}\sigma_-$, where σ_- is the spin-lowering operator, and it is a situation that we can find,

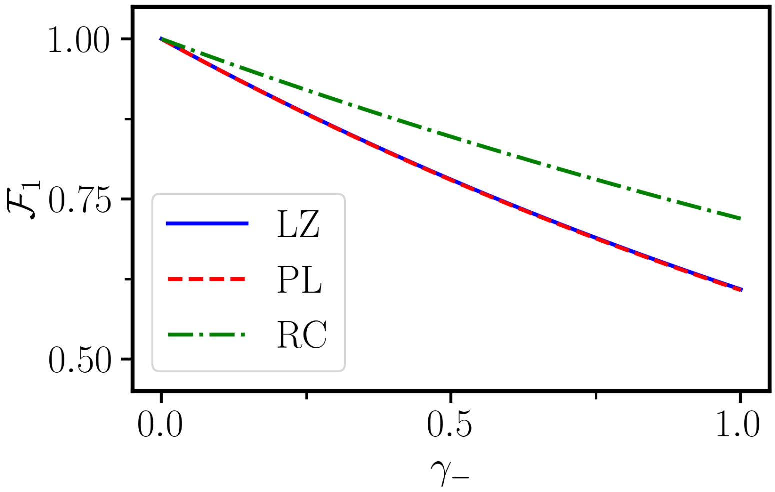

Figure 4.5: Fidelity $\mathcal{F}_1$ at the end of the protocols as a function of the decay rate γ_-, for the sweeps LZ (solid blue line), PL (dashed red line) and RC (dashed dotted green line). LZ and PL have the same trend, for the reason showed above in the other figures, and they are more sensitive to the decay because they populate the state $|1\rangle$ much earlier than the RC protocol. Other simulation parameters are the same of Fig. 4.1. (Figure adapted from [99]).

e.g., when we have a thermal bath at zero temperature, so that the absorption probability is practically eliminated.

Figure 4.5 reports the results of the fidelity of the three protocols as a function of the decay rate γ_-. Before explaining what we see from the curves, it worth to point out that the decay process involves only the level $|1\rangle$, when it is occupied. Therefore, since the LZ and PL adiabatic drivings generate a faster population transfer with respect to the RC protocol, they populate very quickly the state $|1\rangle$ and therefore they are more sensitive to the spontaneous emission decay. For this reason, they have lower fidelity with respect to RC sweep which instead, requires longer times to populate the state $|1\rangle$. The LZ and PL have the very same behavior for the same reason we have explained previously for the other figures.

4.3 TWO QUBITS MODEL

In the previous section we have investigated static error and decoherence and decay channels for one qubit platform. Here, instead, we study the same effects but in a two interacting qubits model, relevant in superconducting qubits platform, for instance, for two-qubit gates [4, 56]. The Hamiltonian describing the system in the basis $\{|00\rangle, |01\rangle, |10\rangle, |11\rangle\}$ reads as

$$\hat{H}_{2q}(t) = \frac{\omega_1}{2}\hat{\sigma}_1^z + \left(\frac{\omega_1}{2} + \alpha f(t)\right)\hat{\sigma}_2^z + \Omega\left(\hat{\sigma}_1^+ \otimes \hat{\sigma}_2^- + \hat{\sigma}_1^- \otimes \hat{\sigma}_2^+\right), \tag{4.8}$$

where $\{\hat{\sigma}_k^x, \hat{\sigma}_k^y, \hat{\sigma}_k^z\}$ and $\{\hat{\sigma}_k^\pm = \frac{1}{2}\left[\hat{\sigma}_k^x \pm i\hat{\sigma}_k^y\right]\}$ are the Pauli matrices and the spin raising and lowering operators respectively, for the two qubits $k = 1, 2$, ω_1 is the transition frequency of the qubit levels and Ω is the interaction strength. This type of system can be used to realize an entangling two-qubits gate, which is the one investigated in this part of the thesis. In particular, in this case, we apply the driving only to the second qubit and we leave the first one fixed. In this way, the sweep function represents a modulation between the two qubits and when it is large they do not interact since they are strongly off-resonance, but when it is approaching to 0 they start interacting, according to Eq. (4.8), and the states $|10\rangle$ and $|01\rangle$ form an avoided crossing with a gap of 2Ω. This type of interaction may arise, e.g., in superconducting qubits coupled to a cavity [11, 12, 108].

As we have done for the other Hamiltonians, we write Eq. (4.8) in dimensionless form so that it is written as

$$\hat{H}_{2q}(\tau) = T\left[\frac{\omega_{1\Omega}}{2}\hat{\sigma}_1^z + \left(\frac{\omega_{1\Omega}}{2} + \alpha_\Omega f(\tau)\right)\hat{\sigma}_2^z + \left(\hat{\sigma}_1^+ \otimes \hat{\sigma}_2^- + \hat{\sigma}_1^- \otimes \hat{\sigma}_2^+\right)\right], \tag{4.9}$$

where $\omega_{1\Omega} = \omega_1/\Omega$ and $T = \alpha_\Omega t_f$ and $\alpha_\Omega = \alpha t_f/\Omega$ being defined in the previous sections. The interaction does not involve the states $|00\rangle$ and $|11\rangle$ but only the states $|01\rangle$ and $|10\rangle$. We can better appreciate this feature from the matrix form of the Hamiltonian (4.9) which is

$$\hat{H}_{2q}(\tau) = \begin{pmatrix} \omega_{1\Omega} + \alpha_\Omega f(\tau) & 0 & 0 & 0 \\ 0 & -\alpha_\Omega f(\tau) & 1 & 0 \\ 0 & 1 & \alpha_\Omega f(\tau) & 0 \\ 0 & 0 & 0 & -\omega_{1\Omega} - \alpha_\Omega f(\tau) \end{pmatrix}. \tag{4.10}$$

We see, thus, that only the states $|01\rangle$ and $|10\rangle$ are coupled and for this reason such an Hamiltonian can be used to build an entangling gate, resulting then in the creation of the Bell states $|\mathrm{Bell}_\pm\rangle = \frac{1}{\sqrt{2}}[|01\rangle \pm |10\rangle]$. Therefore, the natural definition of the fidelity, in this case, is the probability to be in one of the Bell states at the end of the evolution. In this case, assuming that we start from the state $|01\rangle$, the fidelity is computed as the probability to end in the state $|\mathrm{Bell}_+\rangle$ at $\tau = 1$. In formula it reads

$$\mathcal{F}_2 = |\langle\psi(\tau=1)|\mathrm{Bell}_+\rangle|^2. \tag{4.11}$$

In order to perfectly follow the instantaneous eigenstate of the system we are interested in, we need to compute the CD terms that, in this particular case, can be done analytically. Thus, in the following, we will show the main steps of the calculation.

As a starting point, we calculate the time dependent eigenvalues and eigenvectors, that are respectively $E_{0,3} = \pm\left(\alpha_{\Omega} f(\tau) + \omega_{1\Omega}\right), E_{1,2} = \pm\sqrt{1+\alpha_{\Omega}^2 f(\tau)^2}$ and

$$|\psi_0\rangle = \begin{pmatrix} 1 \\ 0 \\ 0 \\ 0 \end{pmatrix}, \qquad |\psi_1(\tau)\rangle = \frac{1}{N_2}\begin{pmatrix} 0 \\ -\alpha_{\Omega}\left(f(\tau) + \sqrt{1+\alpha_{\Omega}^2 f^2(\tau)}\right) \\ 1 \\ 0 \end{pmatrix},$$
$$|\psi_2(\tau)\rangle = \frac{1}{N_3}\begin{pmatrix} 0 \\ -\alpha_{\Omega} f(\tau) + \sqrt{1+\alpha_{\Omega}^2 f^2(\tau)} \\ 1 \\ 0 \end{pmatrix}, \qquad |\psi_3\rangle = \begin{pmatrix} 0 \\ 0 \\ 0 \\ 1 \end{pmatrix}. \tag{4.12}$$

where N_2 and N_3 are the corresponding normalization constants $N_2 = \sqrt{\left(\alpha_{\Omega} f(\tau) + \sqrt{1+\alpha_{\Omega}^2 f^2(\tau)}\right)^2 + 1}$ and $N_3 = \sqrt{\left(-\alpha_{\Omega} f(\tau) + \sqrt{1+\alpha_{\Omega}^2 f^2(\tau)}\right)^2 + 1}$. Then we compute the time derivative of the Hamiltonian

$$\frac{d\hat{H}(\tau)}{d\tau} = \alpha_{\Omega}\dot{f}(\tau)\begin{pmatrix} 1 & 0 & 0 & 0 \\ 0 & -1 & 0 & 0 \\ 0 & 0 & 1 & 0 \\ 0 & 0 & 0 & 1 \end{pmatrix} \tag{4.13}$$

where the dot notation represents the time derivative. Thus, recalling the Eq. (2.25), the $\hat{H}_{CD}$ matrix for this system is

$$\begin{aligned} \hat{H}_{CD}(\tau) &= i\hbar \sum_{m\neq n}\sum_{n} |\psi_m(\tau)\rangle \frac{\langle\psi_m(\tau)|\dot{H}|\psi_n(\tau)\rangle}{E_n(\tau) - E_m(\tau)} \langle\psi_n(\tau)| = \\ &= i\hbar \frac{\alpha_{\Omega}\dot{f}(\tau)}{2\left(1+\alpha_{\Omega}^2 f^2(\tau)\right)}\begin{pmatrix} 0 & 0 & 0 & 0 \\ 0 & 0 & -1 & 0 \\ 0 & 1 & 0 & 0 \\ 0 & 0 & 0 & 0 \end{pmatrix} = \\ &= -\hbar \frac{\alpha_{\Omega}\dot{f}(\tau)}{4\left(1+\alpha_{\Omega}^2 f^2(\tau)\right)}\left(\hat{\sigma}_1^x \otimes \hat{\sigma}_2^y - \hat{\sigma}_1^y \otimes \hat{\sigma}_2^x\right). \end{aligned} \tag{4.14}$$

In this particular case, we were able to find an analytical expression for the CD term because, as we have mentioned before, the interaction acts only on the two states $|01\rangle$ and $|10\rangle$, and the treatment is similar to the one-qubit model. In Fig. 4.6, similarly to the one qubit case, the characterization of the system is represented. In particular, Fig. 4.6(a) represents the temporal shape of the sweep functions, Fig. (b) the matrix element of the $\hat{H}_{CD}$ for the three protocols, while Fig. (c) the corresponding fidelities.

In the following we study the robustness of the protocols against dephasing, decoherence and decay.

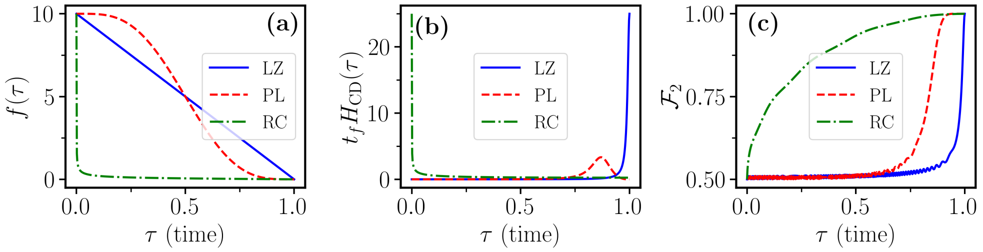

Figure 4.6: For the two qubits configurations, temporal profile of (a) the three sweep functions LZ (solid blue line), PL (dashed red line) and RC (dashed dotted green line); (b) the imaginary part of the matrix element computed for the corresponding sweep function; (c) fidelity defined in Eq. (4.11) generated by the three accelerated driving protocols, without any type of external errors. Simulation parameters are $\omega_{1\Omega} = 30$, $T = 10$, $\alpha_\Omega = 10$, $f_0 = 10$, $\gamma = 0$ and $\gamma_- = 0$. (Figure adapted from [99]).

4.3.1 *Dephasing and Spontaneous Emission*

Following the same treatment of the one qubit case, the master equation for the two qubits model is written as (with $\hbar = 1$)

$$\frac{d\rho(\tau)}{d\tau} = -i\left[H_{2q}(\tau), \rho(\tau)\right] + D\left[\hat{c}_1(\theta)\right]\rho(\tau) + D\left[\hat{c}_2(\theta)\right]\rho(\tau), \tag{4.15}$$

where $\hat{c}_k = \sqrt{\gamma}\left[\cos(\theta)\hat{\sigma}_k^z + \sin(\theta)\hat{\sigma}_k^x\right]$, with $k = 1, 2$, is the jump operator associated to the k-th qubit.

In Fig. 4.7 the final fidelity, that is the fidelity $\mathcal{F}_2$ in Eq. (4.11), is shown for the three sweep protocols. As we can observe in the Fig. 4.7, the LZ in (a) is much more robust against the dephasing than the other two sweeps. This is due to the fact that the time spent by the system in a superposition of states is very short compared to the other two protocols. In fact the LZ one, is in the state $|01\rangle$ for the most of the time and approaching the end of the evolution it has a very steep state transfer. By looking, then, at the Figs. 4.7(b) and (c) corresponding to the PL and RC protocols respectively, we see they have different behaviors. In particular the RC sweep has the worst performance among the three driving protocols. This is related to the different temporal shape of their state transfer, showed in Fig. 4.6(c). in which we observe that the RC spends more time in a superposition of states.

Figure 4.8, instead, shows the final fidelity $\mathcal{F}_2$ in the presence of different decay rates for the two qubits, $\gamma_-^{(1)}$ and $\gamma_-^{(2)}$ respectively. It can be noticed that the three sweeps have different performance due to their different temporal shape of the fidelity. The behavior in Fig. 4.8 can be understood by considering the effect of the spontaneous emission on one of the two qubits at a time. In fact, if we look at the Fig. 4.8(a) corresponding to the LZ protocol, we see that it is very robust against the decay on first qubit. Recalling that the initial state is $|01\rangle$, the first qubit is in the state $|0\rangle$ for the most of the evolution time, since the temporal shape of the LZ fidelity has an abrupt change of the state transfer at the end of the evolution. On the contrary, the second qubit that starts in $|1\rangle$ is subject to the spontaneous emission effect. Using similar

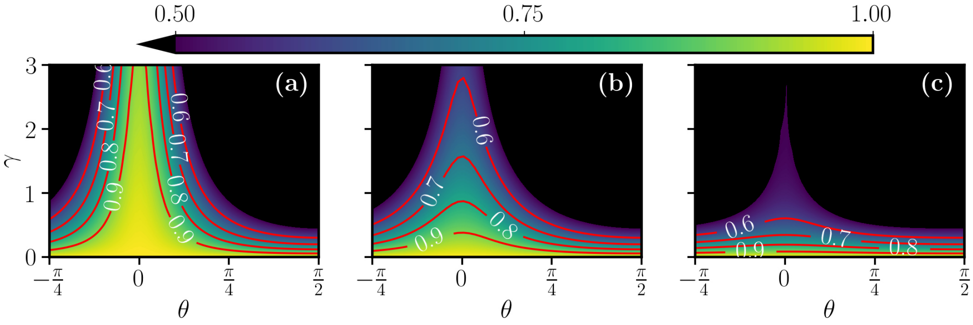

Figure 4.7: Colormap of the fidelities $\mathcal{F}_2$ at the end of the evolution for the three sweeps (a) Landau-Zener, (b) Polynomial and (c) Roland-Cerf as a function of θ. The LZ protocol is more robust against the pure dephasing, that is $\theta = 0$ and $\hat{c}_k = \hat{\sigma}_k^z$, with respect to the other two. The reason is found by looking at the temporal profile of the fidelity in Fig. 4.6(c) in which the LZ one is the steepest one. Other simulation parameters are the same used in the Fig. 4.6. We considered the same rate γ for both the qubits. (Figure taken from [99]).

argument, the behavior of the fidelities in Figs. 4.8(b) and (c), associated to the PL and RC sweeps, can be explained. It is worth noting that in all the three adiabatic protocol, the behavior of the fidelity when $\gamma_-^{(1)} = \gamma_-^{(2)}$, namely on the main diagonal of the colormaps, is the same.

4.3.2 *Relative Parameter error*

In this section, as we have done for the two-level system in Sec. 4.2, in Fig. 4.9 we report the robustness analysis for the two-qubit system of Eq. (4.8). As mentioned before, the range of errors analyzed here are typical of experimental setup as in [100–102], where the error on the initial and final energy gap of the system can reach very high values. Since we are investigating a different qubit model, we expect different results with respect to the two-level case. In particular, the LZ protocol of Fig. 4.9(a) is the less robust among the three sweep functions. It shows great stability for error $\epsilon < 50\%$ but it is very sensitive for greater values. The PL protocol, instead, apart from a narrow low fidelity region for small values of T, presents a very stable behavior for larger error values. The RC sweep is very insensitive to the error and in contrast to the case of Fig. 4.3. In this case, such a behavior can be understood by looking at the temporal shape of the sweep functions in Fig. 4.6(a). We recall that the two qubits are in resonance when the sweep $f(\tau)$ is 0. Indeed, the RC function reaches the 0 value faster than the other two sweeps and therefore the two qubits are in resonance for longer time.

4.4 REMARKS

In this chapter, we have explored different adiabatic protocols subject to dephasing, decoherence and decay by spontaneous emission. For the study they

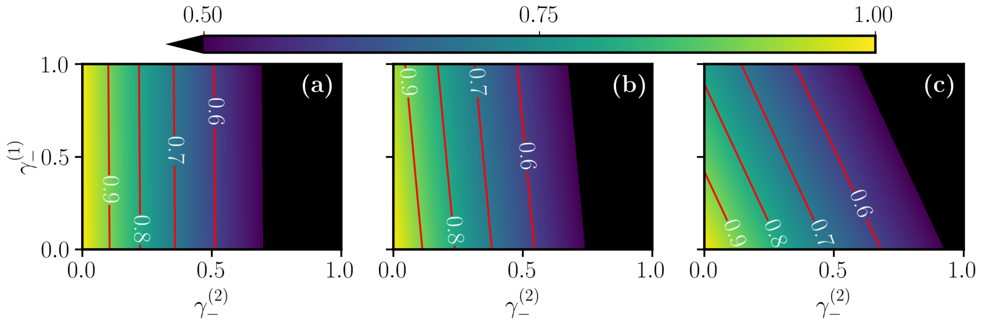

Figure 4.8: Colormap of the fidelity $\mathcal{F}_2$ as a function of different decay rates $\gamma_-^{(1)}$ and $\gamma_-^{(2)}$ associated to the two qubits. (a) represents the Landau-Zener protocol, (b) the Polynomial one and (c) the Roland-Cerf. The three driving protocols have different behavior and this is related to the different state transfer that we can appreciate in Fig. 4.6(c). Their behavior is understood by considering the effect of the spontaneous emission of one qubit at a time. More detail are given in the main text. The other simulation parameters are the same of Fig. 4.6. (Figure taken from [99]).

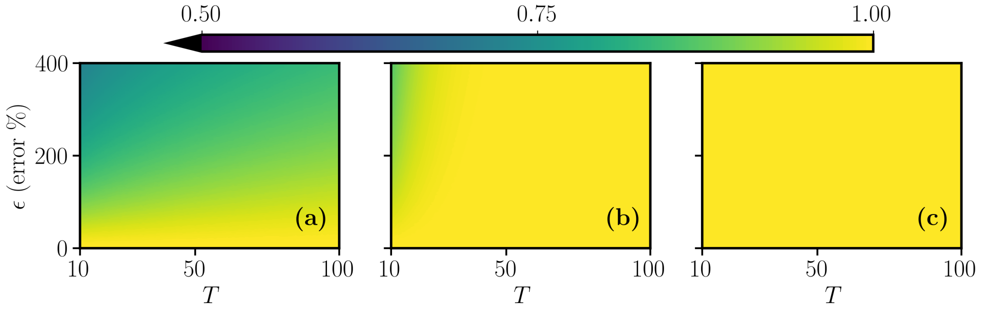

Figure 4.9: Colormap of the fidelity in Eq. (4.11) in the (ϵ, T) plane for the adiabatic protocols, with the parameter error ϵ, (a) Landau-Zener, (b) Polynomial, (c) Roland-Cerf accelerated with the Berry Counterdiabatic Driving Hamiltonian. In this case, the LZ protocol exhibit worsen performance than the other two sweeps. The PL protocol, apart from a lower fidelity at small values of T, it shows a very robust behavior for the rest of the values. RC sweep, instead, is very insensitive to error and it shows the greatest stability among the driving protocols. Parameters simulation are the same as in Fig. 4.6.

have been accelerated using the specific STA technique of the CD driving [33, 34]. The three sweep functions have been applied to two different systems: a one qubit model, in Sec. 4.2, and a two qubits one realizing an entangling gate, in Sec. 4.3. For the first case, we studied the robustness of the STA protocol in the presence of static error, and the results show a very high stability for all three adiabatic protocols. Then, in both cases it is studied the influence of dephasing and decoherence on the chosen drivings, in Sec. 4.2.2 and 4.3.1 respectively. In this case, we could notice that each sweep function behave differently according to the decoherence and decay channels affecting the system. This indicates that, adiabatic protocols used in operations like quantum state transfer or quantum gates can be optimized also for mitigating noise in open system environment. In Sec. 6.2, we provide an overview on the STA protocol applied to an adiabatic quantum CZ gate in anisolated environment. Basing on our findings in this chapter, the study of the CZ gate could be extended to an open scenario and the accelerated adiabatic protocol could be further optimized. In the next Ch. 5, instead, we provide a different perspective for optimizing quantum state transfer which is not based on adiabatic evolution but rather it exploit the atomic interaction as a compensation tool.

Part III

ERROR COMPENSATION WITH INTERACTION

5

INTER-ATOMIC INTERACTION FOR ERRORS COMPENSATION

Experimental quantum operations, e.g., quantum gates, quantum state transfer or quantum control in general, are often affected by errors due to the imperfect experimental apparatus or by the external environment, as we have seen in the previous chapter, which limit their performance. During the years, many strategies and protocols have been investigated for counteracting the problem. Some examples are quantum error correction codes [4, 16, 17] which are based on the idea to protect the qubit information using the redundancy, as in the classical analogous, or composite pulses [109, 110] which is a technique based on a sequence of pulses for reaching a target fidelity, or also robust protocols [29, 111] like those studied in the previous chapters of this thesis (STA). In this direction, in our study, we analyze Rydberg atoms being a very promising platform for quantum computing and simulation [14, 112]. In particular, we aim at compensating accumulated phase [113, 114], in a periodic laser driving, generated, e.g., by the imperfection in the control parameters [115]. Our scheme avoid the propagation of the error during the periods, that is an idea similar to the fault-tolerant paradigm for quantum computation [4, 16, 17]. In fact, since we implement a sequence of pulses, our approach could seems similar to the composite pulses technique [109, 110]. However, the substantial difference between the two methods is that, while the composite pulse aim at obtaining high fidelity at the end of the evolution, we, in contrast, aim at obtaining high fidelity for all the periods.

The correcting scheme presented in this chapter, relies on the Rydberg inter-atomic interaction between two interacting qubits. In principle, such an interaction could be experimentally controlled [14], e.g., by an electric field in the presence of F$'$orster resonance [114, 116–118]. The phase errors that we consider affect also the population of the qubit-levels. We show that the interaction tuning feature is relevant for our protocol because the phase correction will compensate also the errors affecting the levels population.

In this chapter, we first introduce the details of the protocol in Sec. 5.1. Then, we analyze two different excitation processes: single photon in Sec. 5.2 and two photons in Sec. 5.3. For the first case, synchronous and asynchronous driving configurations have been investigated, in Secs. 5.2.3 and 5.2.2 respectively, and for each of them we study the performance in the presence of rotation-angle and rotation-axis error. For the two-photon excitation case, instead, first we introduce the Stimulated Raman Adiabatic Passage (STIRAP) protocol [119] in Sec. 5.3.1 and then it has been studied in a synchronous driving configuration, in Sec. 5.3.2, as exemplary scenario.

5.1 SYSTEM SETUP

For the compensation scheme described in Fig. 5.1(a), we consider two qubits realizable using Rydberg atoms [14] which interact with a nearest-neighbor interaction V. The two qubits, which we call *computational* and *correction* qubits, are excited by a periodic laser field of period $T = 2T_1 + 2T_2$ with a temporal profile Ω as in Fig. 5.1(b). During the time T_1, a bit flip operation is performed using a π pulse, resulting in a population transfer; whereas, during T_2, the laser is off and only the interaction V drives the dynamic of the system. After that, another π pulse is performed in order to reinitialize the system to its initial state and the T_2 time concludes the cycle. This defines our period T such that the probability that the system is in the initial state, e.g. ground state, assumes the temporal behavior shown in Fig. 5.1(c).

We want to anticipate that, for most of the results presented in this chapter, we neglect the interaction during T_1 because we assume, that $T_1 \ll T_2$. This means that the duration T_1 of the π pulse is much shorter than the time T_2. Such an assumption, will help us in the analytical treatment of the system dynamics.

In the following, we also assume that the bit flip operations described above are repeated a certain number of times, which we chose to be $n = 50$. Moreover, at each period an error occurs in the system which, accumulating, reduces the performance (fidelity) of the system. Using the interaction experienced by the two atoms, we aim at compensating the unwanted phase which is generated by the errors.

For all the cases examined in this chapter, the interaction is described by the Hamiltonian

$$H_V = V|e_1\rangle|e_2\rangle\langle e_1|\langle e_2|\,, \tag{5.1}$$

where the state $|e_k\rangle$ is the excited state of the k-th qubit and V is the interaction strength. In Rydberg atoms the interaction can have different forms according to the atomic states considered [14]. In particular, in our work we use qubits of the *gr* type, which means that the qubit consists in weakly-interacting ground state $|g\rangle$ and a strongly-interacting excited one which we call $|e\rangle$. The strong interaction given by the excited state is obtained by reaching states with a very high principal quantum number, typically $n > 60$ [14]. The interaction can be controlled by the Förster resonances and the scaling law of the interaction varies according to the coupling between the Rydberg states of the two qubits, i.e., if they are resonantly or non-resonantly coupled [14, 26, 116]. For instance, in the resonant case, the dipole-dipole interaction scales as $V \propto n^4/R^3$ [120] where R is the distance between the qubits.

The Hamiltonian describing the remaining part of the dynamics change according to the system considered. Therefore, they are introduced in the corresponding sections in the following.

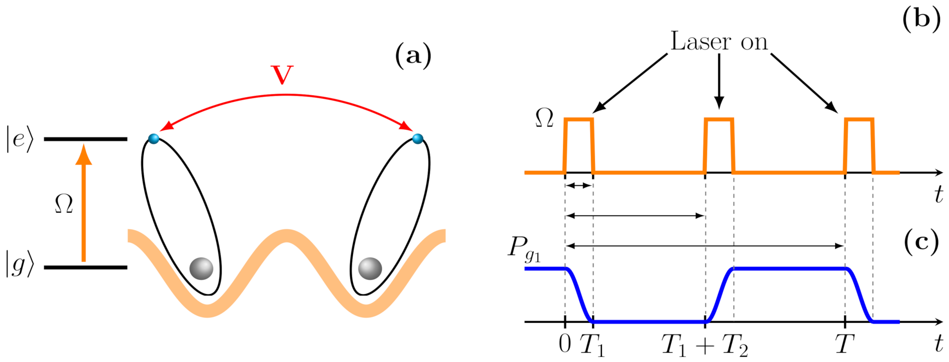

Figure 5.1: (a) Qubits scheme for compensation. Two qubits subject to a periodic potential and experiencing a nearest-neighbor interaction V are excited by a periodic optical field, depicted in (b). The laser is turned on for a time T_1 during which a π pulse is performed, and then is turned off for a time T_2 during which the interaction V governed the evolution. In such a way, the laser period is $T = 2T_1 + 2T_2$ and the occupation probability of the ground state as a function of time is shown in (c). (Figure adapted from [121]).

5.2 SINGLE-PHOTON EXCITATION

For the single-photon case we consider a two qubits system governed by the single-atom Hamiltonian ($\hbar = 1$)

$$H_{0k} = -\delta|e_k\rangle\langle e_k| + \frac{\Omega}{2}\left(|g_k\rangle\langle e_k| + |e_k\rangle\langle g_k|\right) , \tag{5.2}$$

where $\delta = \omega_L - \omega_0$ is the detuning between the laser frequency ω_L and the ground state energy ω_0, Ω is the Rabi frequency of the laser and $k = 1, 2$ the two qubits. Equation 5.2 is written in the RWA which, in this case, holds for $\Omega \ll \omega_L$. Moreover, although it is not specified in the equation, the Rabi frequency Ω is time dependent with temporal profile as in the Fig. 5.1(b).

5.2.1 *Static Errors*

The aim of this work is to show that the interaction between two atoms can be used to compensates unwanted effects that reduce the performance of the system. For this purpose, we consider two kind of static errors (i) *rotation-angle error* and (ii) *rotation-axis error*. Both the errors can be generated by imperfections in the control parameters that, at each quantum operation, can accumulate a small amount of unwanted phases. In detail, the two errors are

(i) *Rotation-angle error*. We have seen that during the time T_1 a bit flip operation is performed using a π pulse. This means that the condition $\Omega T_1 = \pi$ must be satisfied in order to guarantee a perfect population transfer from the ground state $|g_j\rangle$ to the excited state $|e_j\rangle$ of the j-th qubit. Visualizing the state of the qubit on the Bloch sphere, as depicted in Fig. 5.2(a), it represents a perfect rotation from one pole to the other represented by the dotted blue trajectory in the figure. In this sense,

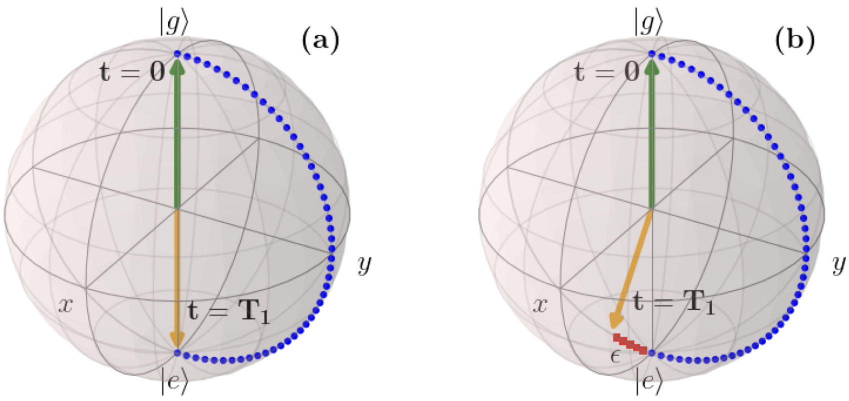

Figure 5.2: State vector on the Bloch sphere in the case of perfect excitation (a) and excitation with rotation-angle error, of Eq. (5.3)(b). In (a), the initial state vector at time $t = 0$ is represented by the green arrow pointing in the north direction at the state $|g\rangle$, the final one at time $t = T_1$, instead, is represented by the yellow arrow pointing in the south direction at the state $|e\rangle$. The trajectory is represented by the dotted blu line denoting the perfect rotation of the vector. In (b), instead, the initial state vector is the same as in (a), while the final one is not pointing at the state $|e\rangle$ anymore but it is slightly rotated of a quantity ϵ. This extra rotation is represented by the red part in the trajectory line and it denotes the error in the control parameter.

we introduce a relative error ϵ on the rotation angle which generates an extra rotation of the Bloch vector, represented by the red part of the trajectory of Fig. 5.2(b). In formula, it reads as

$$\Omega T_1 = \pi(1 + \epsilon)\,. \tag{5.3}$$

We will see that such an error generates an extra phase in the evolution of the state of the system, and we aim at compensating it using the inter-atomic interaction introduced above.

(ii) *Rotation-axis error*. In analogy with the angle error, the axis error is defined during the bit flip operation. In this case, the error affects the detuning δ and it is of the form σ_z. In formula, it is written as

$$\delta \times T_1 = \pi\epsilon\,. \tag{5.4}$$

where the dot notation ($\times$) represents the multiplication operation. This error produces a more complicated effect than the angle error because it affects also the Rabi frequency of the driving. In fact, the Bloch vector undergoes a rotation of

$$\Omega_{\text{eff}} T_1 = \sqrt{(\Omega T_1)^2 + (\delta T_1)^2} = \sqrt{\pi^2 + (\pi\epsilon)^2} \approx \pi\left(1 + \frac{1}{2}\epsilon^2\right) \tag{5.5}$$

where in the last step we have expanded the relation assuming $\epsilon \ll 1$. With respect to the angle rotation in Eq. (5.3), here the perturbation on the Rabi frequency is less effective since it is a second order effect.

Now that we have described the errors we considered in our system, in the following we analyze their effects on the performance of different scenarios.

5.2.2 *Asynchronous driving*

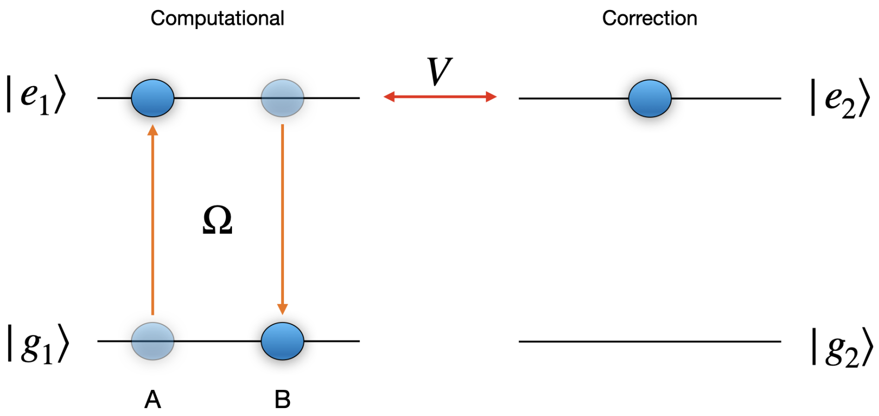

Figure 5.3: Sketch of the two qubits in the asynchronous driving configuration for one period T. The computational qubit is subjected to a first operation, denoted with the letter A, from the state $|g_1\rangle$ to $|e_1\rangle$, then interacts with the correction qubit through the excited state, and finally in the second operation, denoted with B, it is returned to its initial state. The operations are performed using laser pulses with Rabi frequency Ω. The correction qubit, instead, is prepared in the excited state and it is left there for the entire duration of the protocol.

The first case of single-photon excitation that we consider is the asynchronous driving. In this case, the two atoms are driven separately and this assumes the ability to individually address the single atoms, or qubits, in an experiments. Rydberg atoms is a suitable platform for realizing such a system [14]. In the following, we will see that this scenario is also much simpler to study than the others because the two qubits problem can be reduced to a one qubit one. This is possible by considering the correction qubit addressed independently of the computational one and, therefore, it can be prepared in its excited state $|e_2\rangle$ without perturbing the other qubit. In this way, the effect of the interaction generated by the correction qubit acts as an energy shift on the computational one. For this reason, the problem can be practically treated as a two level model. In an experimental scenario, this can be realized by choosing two Rydberg atoms with different resonance frequencies, so that when one is excited the other is strongly off-resonance and therefore the two atoms are addressed separately. A sketch of the configuration is shown in Fig. 5.3. We see that only the computational qubit is subjected to the driving field, while the correction one is insensitive to the laser and it is fixed in its excited state $|e_2\rangle$.

For measuring the performance of the system, we use the concept of the fidelity that we have encountered in the previous chapters. In this case, it is defined as the probability of finding the computational qubit in its ground state $|g_1\rangle$ at time nT, that is at the end of each period. For the present two level case, it has the expression

$$\mathcal{F}_1(t = nT) = |\langle g_1|\psi_1(t = nT)\rangle|^2 , \tag{5.6}$$

where $|\psi_1(t = nT)\rangle$ is the wavefunction of the computational qubit at the time nT. In the following plots, for a better visualization, we also use the infidelity $\mathcal{I}_1(t = nT) = 1 - \mathcal{F}_1(t = nT)$.

5.2.2.1 Results: Rotation-Angle Error

In this section we present the results for the asynchronous case. This particular situation can be modeled as a two level system and, although it is a simplification, the analytical treatment will be very useful to understand also more general cases.

We now show the main steps to derive the analytical expression of the fidelity introduced in Eq. (5.6). In the limit $T_1 \ll T_2$, we start from the Eq. (5.2) and, for simplifying the calculations, we change the zero of the energy such that the computational qubit Hamiltonian during T_1 reads

$$H_{01} = \frac{\delta}{2}\sigma_z + \frac{\Omega}{2}\sigma_x . \tag{5.7}$$

During T_2, instead, the laser is off and the interaction is on. Therefore the system is driven by $H_{01} = \frac{\delta}{2}\sigma_z$ and $H_V = V|e_1\rangle\langle e_1|$. Now, to calculate the fidelity we consider only the state of the system at time nT. However, an analytical treatment for arbitrary number of periods is not easily feasible. For this reason, we compute the fidelity only for one period, that is $n = 1$. For the purpose, we evaluate the evolution operators $U_1(t = T_1) = e^{-iH_{01}T_1}$ and $U_2(t = T_2) = e^{-i(H_{01}+H_V)T_2}$. Then, using the known relation for the exponential of Pauli matrices we can write

$$\begin{aligned} U_1(T_1) =& \mathbb{1}\cos\left(\frac{1}{2}\sqrt{\Omega^2+\delta^2}\right) + \\ & - i\left(\frac{\Omega T_1}{\sqrt{\Omega^2+\delta^2}}\sigma_x + \frac{\delta T_1}{\sqrt{\Omega^2+\delta^2}}\sigma_z\right)\sin\left(\frac{1}{2}\sqrt{\Omega^2+\delta^2}\right) . \end{aligned} \tag{5.8}$$

$$U_2(T_2) = e^{-i\frac{\delta T_2}{2}} e^{-iVT_2|e_1\rangle\langle e_1|} . \tag{5.9}$$

Thus, the state of the system at time $t = T$ is found by

$$|\psi(T)\rangle = U_2(T_2)U_1(T_1)\left[U_2(T_2)U_1(T_1)|\psi_0\rangle\right] , \tag{5.10}$$

where $\psi_0 = \psi(t = 0)$ is the initial state. Now that we have the general expression of the unitary operator when $T_1 \ll T_2$ holds, we can compute the fidelity for the error cases separately. Let us consider the system affected only by the angle error, so we put $\underline{\delta = 0}$ in the evolution operators in Eqs. (5.8) and (5.9). Assuming that the initial state is $|\psi_0\rangle = \begin{pmatrix} 1 \\ 0 \end{pmatrix}$ and using Eq. (5.10) and the related expressions for the evolution operators in Eqs. (5.8) and (5.9), we obtain

$$\begin{aligned} |\psi(T)\rangle =& C_g(T)|g_1\rangle + C_e(T)|e_1\rangle = \\ =& \left[\cos^2\left(\frac{\Omega T_1}{2}\right) + \sin^2\left(\frac{\Omega T_1}{2}\right) e^{-iVT_2}\right] |g_1\rangle + \\ & + i\sin\left(\frac{\Omega T_1}{2}\right)\cos\left(\frac{\Omega T_1}{2}\right)\left[1 + e^{iVT_2}\right] e^{-iVT_2}|e_1\rangle \,. \end{aligned} \tag{5.11}$$

Now, to compute the probability of being in the ground state $|g_1\rangle$ it is convenient to consider the coefficient C_e of the state $|e_1\rangle$. Therefore, after some algebraic manipulation we arrive at

$$\mathcal{F}_1(T) = |C_g|^2 = 1 - |C_e|^2 = 1 - \frac{1}{2}\sin^2\left(\frac{\Omega T_1}{2}\right)\left[1 + \cos\left(VT_2\right)\right] \,. \tag{5.12}$$

Recalling that $\Omega T_1 = \pi(1+\epsilon)$, being ϵ the rotation-angle error, the final expression of the fidelity is

$$\begin{aligned} \mathcal{F}_1(T) =& 1 - \frac{1}{2}\sin^2\left(\pi\epsilon\right)\left[1 + \cos\left(VT_2\right)\right] \\ \approx& 1 - \frac{1}{2}\left(\pi\epsilon\right)^2\left[1 + \cos\left(VT_2\right)\right] \,, \end{aligned} \tag{5.13}$$

where in the latter line we have expanded the expression for small ϵ in order to highlight the quadratic dependence of the fidelity on the error. Equation (5.13) shows also a key result for the rotation-angle error case, that is

$$\boxed{VT_2 = (2k+1)\pi \,,} \tag{5.14}$$

for integer k. From the first line of Eq. (5.13) we notice that the magic value in Eq. (5.14) produces a perfect correction of the error, as shown in the App. C. We will see that the magic condition is valid also in the synchronous driving case, although in an approximated way.

Figure 5.4 shows the infidelity $\mathcal{I}_1$, as a function of the error ϵ and dimensionless interaction VT_2, for the periods $n = 1$ in 5.4(a) and $n = 50$ in 5.4(b). Both the plots show that the best compensation region is around the magic value of the interaction found in Eq. (5.14). In particular, in Fig. 5.4(b), after 50 periods the region of high fidelity becomes narrower with respect to the one in the plot (a). This, would require a more precise control of the interaction in a real experiment.

5.2.2.2 *Results: Rotation-Axis Error*

In this section, we investigate the effects of the only rotation-axis error, so we have $\delta \neq 0$. As in the previous case, we want to compute the fidelity in order to study the performance of the system. For the purpose, we can use

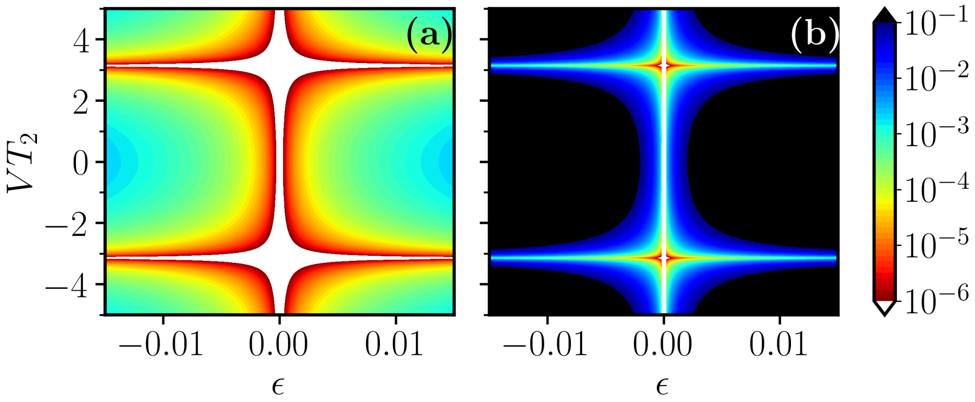

Figure 5.4: Colormap of the infidelity $\mathcal{I}_1$, in logarithmic scale, as a function of dimensionless ϵ and VT_2 for the asynchronous driving case. Figure (a) reports the infidelity after one period, $\mathcal{I}_1(t = T)$. While, the case (b) is the infidelity after 50 periods, namely $\mathcal{I}_1(t = 50T)$. In these plots we assume that the interaction V during T_1 is negligible. In both the cases, (a) and (b), we can identify the magic value of the interaction, $VT_2 = \pm\pi$, where the fidelity is maximum. Other simulation parameters are $\delta = 0$. (Figure adapted from [121]).

the unitary evolution operators defined in Eqs. (5.8) and (5.9), and the $|\psi(T)\rangle$ in Eq. (5.10). In this case, the expressions generated by such an evolution are much more complicated than the angle error case. This is because, as we have seen in the Sec. 5.2.1, the axis error affects not only the axis, but also the angle. However, recalling that $\delta T_1 = \pi\epsilon$ and $\Omega T_1 = \pi$, for small ϵ we can find a more readable fidelity which is

$$\mathcal{F}_1(T) \approx 1 - 2\epsilon^2 \left[1 - \cos(VT_2)\right] - \pi\epsilon^3 \left(2T_2 + 1\right) \sin(VT_2) . \tag{5.15}$$

The sin function in Eq. (5.15) indicates a different symmetry with respect to the angle error case. In fact, the infidelity, which is depicted after $n = 1$ and $n = 50$ periods in Fig. 5.5, in this case shows a different symmetry along the horizontal axis. As in the angle error case, the one period infidelity in Fig. 5.5(a) and the fifty periods one in (b) have very similar behavior. The diagonal trend that we can appreciate in both the Figs. 5.5(a) and (b) is also found, although with some differences, in the synchronous driving case in the next section.

5.2.3 *Synchronous driving*

In this section, we investigate the single-photon excitation case in which the two qubits are simultaneously driven. A sketch of the configuration is depicted in Fig. 5.6, where we see that two qubits are simultaneously driven by the same laser pulse with Rabi frequency Ω. Notice the similarity with adiabatic CZ gate scheme in Sec. 6.2.2. We will see that, in this case, the four-level initial model can be reduced to a three-level one, with a proper change of basis. As in the previous sections, in the limit for which $T_1 \ll T_2$, the evolution during T_1 is generated by H_{0k} with $V = 0$, while during T_2 the system

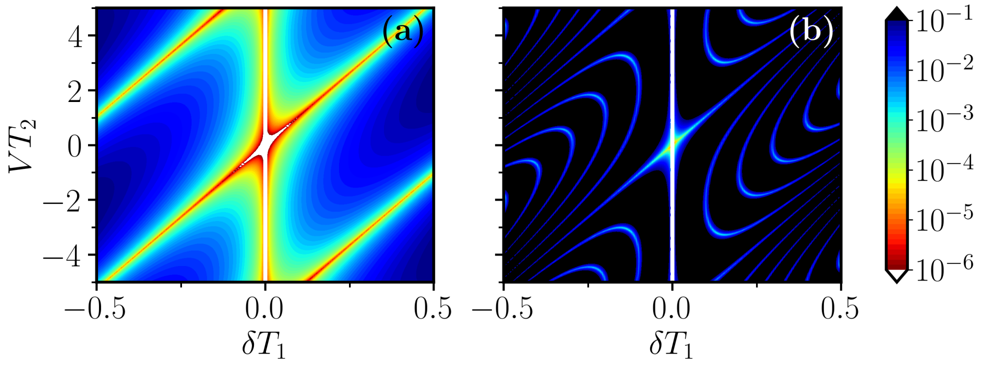

Figure 5.5: Colormap of the infidelity $\mathcal{I}_1$, in logarithmic scale, as a function of dimensionless δT_1 and VT_2 for the asynchronous driving case. Figure (a) reports the infidelity after one period, $\mathcal{I}_1(t = T)$. While, the case (b) is the infidelity after 50 periods, that is $\mathcal{I}_1(t = 50T)$. In these plots we assume $V = 0$ during T_1. Other simulation parameters are $\Omega T_1 = \pi$.

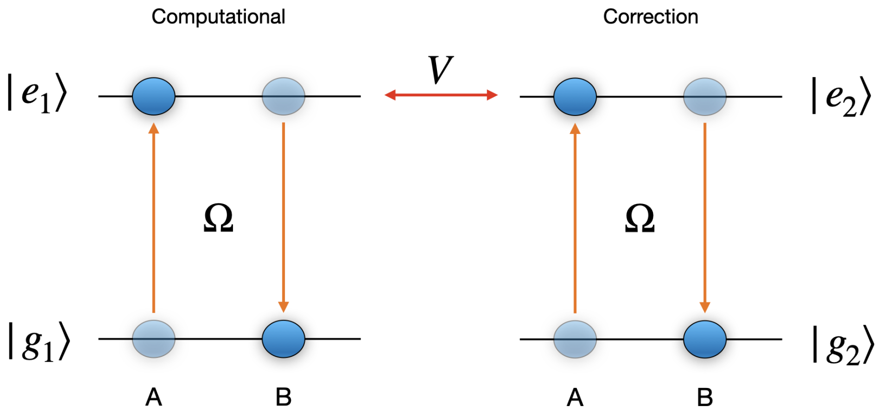

Figure 5.6: Sketch of the two qubits in the synchronous driving configuration for one period T. In contrast to the Fig. 5.3, here both qubits are subjected to the driving field, with Rabi frequency Ω, which excites the qubits from the ground state to the excited state simultaneously during the operation denoted with A, and takes back the qubits to the initial ground state during the operation denoted with B. The interaction, as before, occurs when both qubits are in the excited state.

is governed only by the interaction. Thus, starting from the complete matrix for the time T_1 system in the basis $\{|g_1, g_2\rangle, |g_1, e_2\rangle, |e_1, g_2\rangle, |e_1, e_2\rangle\}$, $(\hbar = 1)$

$$H = H_{01} \otimes \mathbb{1} + \mathbb{1} \otimes H_{02} = \frac{1}{2} \begin{pmatrix} 0 & \Omega & \Omega & 0 \\ \Omega & \delta & 0 & \Omega \\ \Omega & 0 & \delta & \Omega \\ 0 & \Omega & \Omega & \delta \end{pmatrix}, \tag{5.16}$$

we can apply a unitary transformation using the Dicke states [122–125]

$$\begin{aligned} |g_1, g_2\rangle_D &= |g_1, g_2\rangle_S & \quad |s\rangle_D &= \frac{1}{\sqrt{2}} \left(|g_1, e_2\rangle_S + |e_1, g_2\rangle_S\right) \\ |e_1, e_2\rangle_D &= |e_1, e_2\rangle_S & \quad |a\rangle_D &= \frac{1}{\sqrt{2}} \left(|g_1, e_2\rangle_S - |e_1, g_2\rangle_S\right) \end{aligned} \tag{5.17}$$

where we have distinguished the Dicke and the starting basis states with the two subscripts D and S, respectively. As a useful notation, we denote the states $|s\rangle$ and $|a\rangle$ symmetric and antisymmetric. The unitary transformation, then, reads as

$$U = \begin{pmatrix} 1 & 0 & 0 & 0 \\ 0 & 1/\sqrt{2} & 1/\sqrt{2} & 0 \\ 0 & 1/\sqrt{2} & -1/\sqrt{2} & 0 \\ 0 & 0 & 0 & 1 \end{pmatrix}. \tag{5.18}$$

Choosing the basis $\{|g_1, g_2\rangle_D, |s\rangle_D, |a\rangle_D, |e_1, e_2\rangle_D\}$, the system Hamiltonian in the new representation is given by

$$H_D = UHU = \begin{pmatrix} 0 & \frac{\Omega}{\sqrt{2}} & 0 & 0 \\ \frac{\Omega}{\sqrt{2}} & \delta & 0 & \frac{\Omega}{\sqrt{2}} \\ 0 & 0 & \delta & 0 \\ 0 & \frac{\Omega}{\sqrt{2}} & 0 & 2\delta \end{pmatrix}. \tag{5.19}$$

We notice that, in our particular case in which the initial state of the system is $|g_1, g_2\rangle$, the antisymmetric state $|a\rangle$ does not participate to the evolution of the system and, therefore, we can neglect it obtaining a reduced three level one. Finally, the two matrices generating the evolution in T_1 and T_2 read as

$$H_D = \begin{pmatrix} 0 & \frac{\Omega}{\sqrt{2}} & 0 \\ \frac{\Omega}{\sqrt{2}} & \delta & \frac{\Omega}{\sqrt{2}} \\ 0 & \frac{\Omega}{\sqrt{2}} & 2\delta \end{pmatrix}, \qquad H_V = \begin{pmatrix} 0 & 0 & 0 \\ 0 & 0 & 0 \\ 0 & 0 & V \end{pmatrix}. \tag{5.20}$$

In this way, the general wavefunction can be expressed as

$$|\psi_{tot}(t)\rangle = C_{gg}(t)|g_1, g_2\rangle + C_s(t)|s\rangle + C_{ee}(t)|e_1, e_2\rangle\,. \tag{5.21}$$

We can, now, define the fidelity as the probability that the computational qubit is in the ground state after a time period nT. Given the wavefunction in Eq. (5.21), the fidelity reads

$$\begin{aligned}\mathcal{F}_2(t=nT) &= \mathrm{Tr}\left[\left(|g_1\rangle\langle g_1|\otimes\mathbb{1}\right)\left(|\psi_{tot}\rangle\langle\psi_{tot}|\right)\right] \\ &= |C_{gg}(nT)|^2+\frac{1}{2}|C_s(nT)|^2\end{aligned} \quad , \tag{5.22}$$

where Tr is the trace operation [4], $|\psi_{tot}\rangle\langle\psi_{tot}|$ is the density operator of the system and $\mathbb{1}$ is the identity matrix. Using Eq. (5.20) with $\delta=0$ and initial state $|g_1,g_2\rangle$, we can compute the fidelity in Eq. (5.22) which is expressed in the Dicke basis. We point out that, as mentioned before, since we start from the pure state $|g_1,g_2\rangle$, the antisymmetric state is never populated and it can be neglected from the treatment.

5.2.3.1 *Results: Rotation-Angle Error*

As in the asynchronous case, we first consider the angle-error case. Therefore, we set $\delta=0$ in the Hamiltonian H_D of Eq. (5.20). Thus, diagonalizing the matrix in Eq. (5.20) and computing the state of the system at time T, we arrive at coefficients

$$\begin{aligned}|C_{gg}(T)|^2 =&\frac{1}{4}\Big[(1-\cos(2\Omega T_1))-\frac{1}{2}(1-\cos(\Omega T_1))^2\times \\ &\times(1-\cos(VT_2))\Big]^2+\frac{1}{16}\left[1-\cos(\Omega T_1)\right]^4\sin^2(VT_2)\end{aligned} \tag{5.23}$$

$$\begin{aligned}|C_s(T)|^2 =&\frac{1}{4}\sin^2(\Omega T_1)\Big[\cos^2(\Omega T_1)\left(5+3\cos(VT_2)\right)+ \\ &+\left(2\cos(\Omega T_1)+1\right)\left(1-\cos(VT_2)\right)\Big]\,.\end{aligned} \tag{5.24}$$

Therefore, using Eq. (5.22) we obtain the fidelity

$$\begin{aligned}\mathcal{F}_2(t=nT) =&\frac{1}{8}\Big(-2\sin(\Omega T_1)\Big(\sin^2\left(\frac{VT_2}{2}\right)\sin(2\Omega T_1)+ \\ &+\cos(VT_2)\sin(\Omega T_1)\Big)+3\cos(2\Omega T_1)+5\Big)\,.\end{aligned} \tag{5.25}$$

As in the previous section, we can expand the latter equation considering small ϵ getting

$$\mathcal{F}_2(t=nT)\approx 1-\frac{1}{2}(\pi\epsilon)^2\left[1+\cos(VT_2)\right]\,. \tag{5.26}$$

The nice feature of Eq. (5.26) is that, at second order approximation, it is equal to the Eq. (5.13) for the asynchronous setup, although they are obtained from different equation. Figure 5.7 shows exactly this behavior. In particular, we can notice that Fig. 5.7(a), which represents the infidelity $1-\mathcal{F}_2(t=T)$ after one period, is very similar to the one seen before in Fig. 5.4(a). This confirms the similarity between the analytical approximation of the two fidelities. However, after 50 periods, they change their behavior. In fact, Fig. 5.7(b) is different from Fig. 5.4(b). However, Fig. 5.7(b) still shows better performance around the magic value found previously in Eq. (5.14). Therefore,

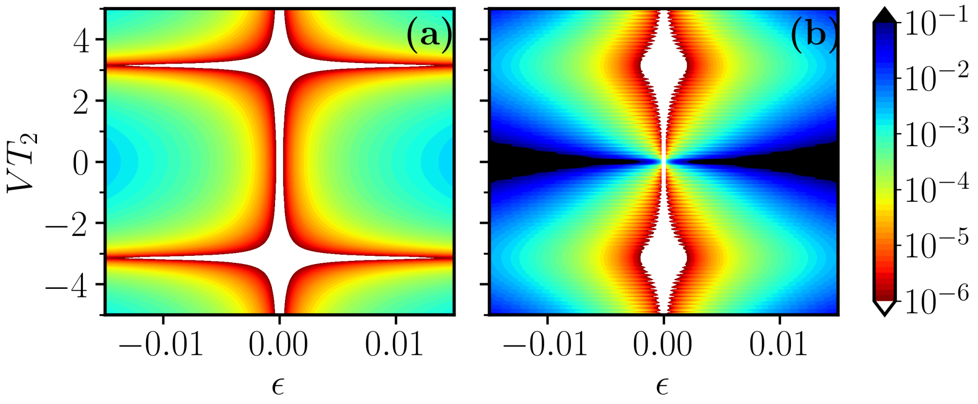

Figure 5.7: Colormap of the infidelity $\mathcal{I}_2$, in logarithmic scale, as a function of dimensionless ϵ and VT_2 for the asynchronous driving case. Figure (a) reports the infidelity after one period, $\mathcal{I}_2(t = T)$. While, the case (b) is the infidelity after 50 periods, namely $\mathcal{I}_2(t = 50T)$. In these plots we assume $V = 0$ during T_1. Figure 5.7(a) is very similar to the Fig. 5.4(a), as anticipated by the Eqs. (5.26) and (5.13). Other simulation parameters are $\delta = 0$. (Figure (b) adapted from [99]).

the analysis of the asynchronous driving is turned out to be useful also for the synchronous driving case.

As last result for this type of error, we analyze the case in which the interaction is not neglected during T_1. As shown by Fig. 5.8, which represents the infidelity $\mathcal{I}_2(t = 50T)$, the system assumes a different behavior with respect to the previous one. We can not identify the magic value compensation for the interaction anymore. However, other values of the interaction, that are $VT_2 = \pm 2.8$ and $VT_2 = \pm 3.9$, show that it is still possible to obtain good fidelity independently of the value of error ϵ. Moreover, increasing the ration $\frac{T_2}{T_1}$, one can find results similar to the case when $V = 0$ in T_1. Unfortunately, analytical results in this case are not feasible, therefore we limit our attention on the numerical simulations just showed.

5.2.3.2 *Results: Rotation-Axis Error*

Likewise the asynchronous model, also for the synchronous driving case we investigate the axis error. We recall that in this case the following relation hold: $\Omega T_1 = \pi$ and $\delta T_1 = \pi\epsilon$. We have seen in the two level model, that the axis error produces effects on the axis and on the angle rotation. The results of numerical simulations are shown in Fig. 5.9. In particular, Fig. 5.9(a) reports the infidelity after 50 periods when $V = 0$ during T_1, therefore, in this case, the relation $T_1 \ll T_2$ holds. Most of the best compensation region can be found in the interval $|\delta T_1| \leq 0.2$ and, in particular, for $|\delta T_1| \lesssim 0.05$ the local diagonal response (in red color in the figure) can be observed as in the asynchronous driving case of Fig. 5.5. A global diagonal behavior, instead, is shown in Fig. 5.9(b). In this case, $V \neq 0$ in T_1 and the plot of the infidelity after 50 periods is very different from the case in (a). However, its global diagonal behavior, together with the previous local one, is a symptom of

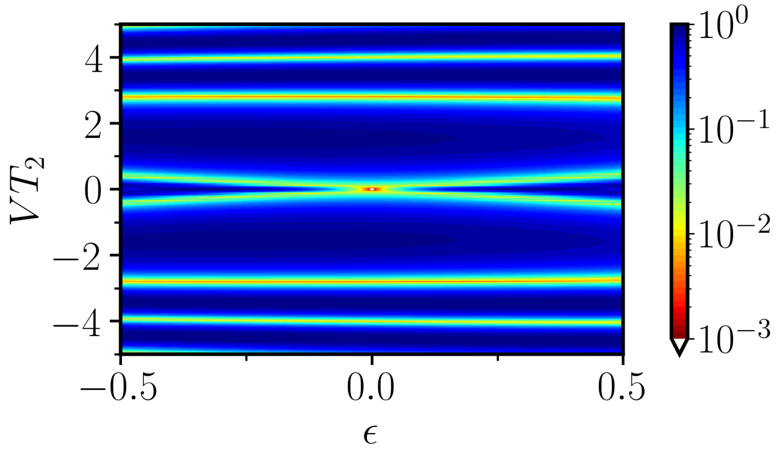

Figure 5.8: Colormap of the infidelity $\mathcal{I}_2(t = 50T)$, that is after 50 periods, in logarithmic scale, as a function of dimensionless ϵ and VT_2 for the asynchronous driving case. Here, $V \neq 0$ during T_1. In this case, the previous magic value for the compensation is not so clear. However, there are two values, $VT_2 = \pm 2.8$ and $VT_2 = \pm 3.9$, for which we can obtain good fidelity independently of the error ϵ. (Figure adapted from [121]).

the antiblockade regime [14, 126]. In fact, in this regime one can excite both atoms when, in general, $\delta = V/2$. In our case, this condition is indicated by the black line in Fig. 5.9(b). In this way, the computational qubit can indeed exploit the interaction of the correction qubit to compensate the error.

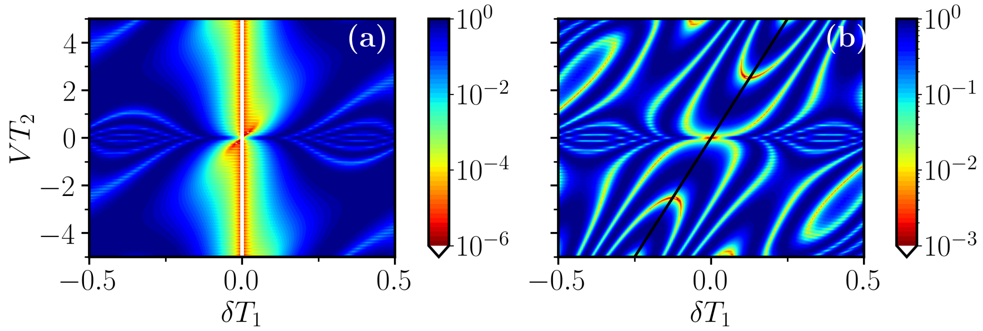

Figure 5.9: Colormap of the infidelity $\mathcal{I}_2(t = 50T)$, that is after 50 periods, in logarithmic scale, as a function of dimensionless δT_1 and VT_2 for the synchronous driving case. In Fig. (a) we assume $V = 0$ during T_1, while in (b) we assume V always on. (Figure taken from [121])

5.2.4 *Stability analysis*

A natural question could be how stable is the conditions that we have found in the previous section. Here, we analyze an example of dynamical error in order to verify the compensation robustness. For the purpose, we apply fluctuations at the interaction value V, supposing the control in the experiment is not very precise. Figure 5.10 shows an example for a cut of Fig. 5.7(b) at $\epsilon = 0.005$. We considered two range of fluctuations, ±5% in Fig. 5.10(a) and

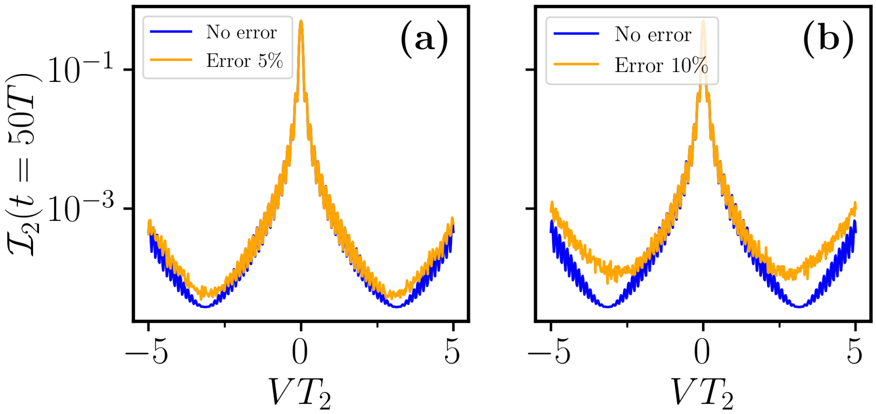

Figure 5.10: Stability of compensation for fluctuations of the interaction value V. We consider the specific value of $\epsilon = 0.005$ of the Fig. 5.7(b). In (a) we consider fluctuations of 5%, while in (b) a fluctuation of 10%. We see that, around the magic value condition, the system has a very stable response. In the figure, the orange curve represents the error curve, while the blue one the curve with no error. The other simulation parameters are the same as in Fig. 5.7(b). (Figure taken from [121]).

±10% in Fig. 5.10(b). In both cases the system response is very stable around the magic value defined in Eq. (5.14), also for the relatively large fluctuations of the second case.

We expect that other cases, for instance the one in Fig. 5.4, are not so stable. In fact, as we have mentioned before, the condition for the optimal compensation in the rotation-angle error of the asynchronous configuration, require a very precise control of the interaction. This is visible especially for high number of periods as in Fig. 5.4(b) where the best compensation region is a very narrow line around $VT_2 = \pm\pi$. From this point of view, the synchronous model described in this section is then more convenient.

5.2.5 *Compensation search tool*

In the previous section, we optimized the fidelity at a given period number n. However, for other values n the best compensation condition could be different from the one we have found. For this reason, we present an analysis tool which allows us to find the compensation condition independently of the number n of periods. For the purpose, we consider the difference between the populations $P(t) = P_g(t) - P_e(t)$ and we analyzed it by means of their Fourier components. In particular, we know that when no error is present, that is $\epsilon = 0$, $P(nT)$ is constant and therefore its Fourier transformation $\tilde{P}(\nu)$ has only one peak at frequency $\nu_0 = 1/T$. This is shown by the dashed red curve in Fig. 5.11(a). Whereas, when the system is affected by an error $\epsilon \neq 0$, the Fourier spectrum has the form of the solid blue curve in Fig. 5.11(a). The single peak centered in ν_0 is now split into two main peaks centered at the frequencies $\nu_0(1 \pm \epsilon T_1)$ and in two additional sidebands, which are visible only at large values of ϵ. The compensation effect of the interaction, in this case,

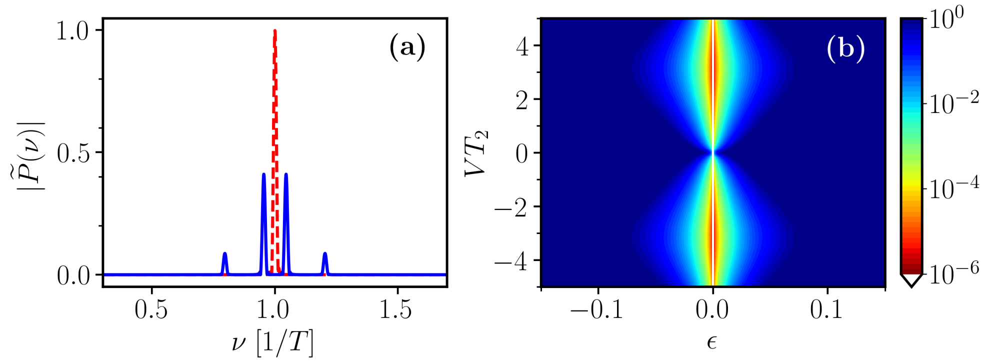

Figure 5.11: (a) Fourier transform $\tilde{P}(\nu)$ of the population difference $P(t)$. The dashed red line represents the case with $\epsilon = 0$ whose peak is at frequency $\nu_0 = 1/T$. While the solid blue one is the case with $\epsilon = 0.1$ and $VT_2 = 1$ whose two main peaks are at frequencies $\nu_0(1 + \epsilon T_1)$. The other small sidebands arise for large values of ϵ. (b) Peak height of the Fourier component $\tilde{P}(\nu_0)$ in logarithmic scale, as a function of parameter space (ϵ, VT_2). There is a strong analogy with the Fig. 5.7(b) confirming the efficacy of such a tool. Other simulation parameters are $\delta = 0$. (Figure taken from [121]).

is to shift the main peaks towards the natural frequency of the system, that is ν_0. Therefore, knowing the height of the peak of the frequency component ν_0, one is able to say whether the interaction compensates the error. Figure 5.11(b) shows a systematic study of the height of $1 - \tilde{P}(\nu_0)$ peak over the parameter space (ϵ, VT_2). We observe that there is a strong similarity with Fig. 5.7(b) that we have encountered before. This, makes the Fourier analysis a very useful numerical tool in searching the compensation condition, independently of the number of periods.

5.3 TWO-PHOTON EXCITATION

So far, we have dealt with a couple of two level atoms which could be reduced to a three-level problem or a two-level one, according to the type of driving we choose. In this part, instead, we analyze the synchronous driving case for a couple of three level interacting systems. In particular, we study a well known protocol in quantum optics called STIRAP (STImulated Raman Adiabatic Passage) [119, 127–130] which, as the mentioned in its name, uses the adiabatic principles presented in Sec. 2.1. In the following, it will be briefly introduced the STIRAP protocol and then we will see how we use it for our compensation scheme.

5.3.1 *STIRAP*

The STIRAP protocol is a technique for quantum state transfer applied, in general, in a three-level system but also in many other setups [119]. We consider a ladder setup shown in Fig. 5.12(a). We can imagine to realize the population transfer $|0\rangle \rightarrow |2\rangle$ passing through the state $|1\rangle$ which, usually,

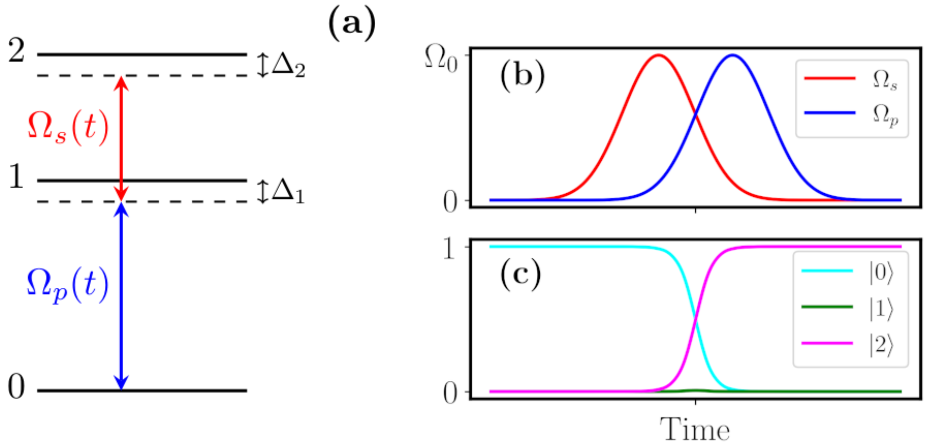

Figure 5.12: (a) Three-level scheme for the STIRAP protocol in a ladder configuration. It is controlled by two laser pulses with Rabi frequency Ω_p and Ω_s. Then, it is characterized by single-photon and two-photon detunings, Δ_1 and Δ_2 respectively. (b) Example of Gaussian temporal profile of the Pump and Stokes pulses. (c) Example of populations transfer $|0\rangle \rightarrow |2\rangle$ with the pulses in (b). We notice that the state $|1\rangle$ is never populated during the transfer.

has a very short life time and therefore an high decay rate. For the purpose, two pulses are used, Ω_p (Pump) and Ω_s (Stokes), represented in Fig. 5.12(a) by the blue and red line respectively. The STIRAP protocol is characterized by a single-photon detuning Δ_1 and a two-photon detuning Δ_2 which must be 0 in order to have a correct population transfer. An example of population transfer is depicted in the right part of Fig. 5.12 with Gaussian pulses in Fig. 5.12(b) and the temporal profile of the populations of the three states in Fig. 5.12(c). For a perfect population transfer, it is used the so-called counterintuitive sequence of pulses, i.e., first the Stokes and then the pump. In this way, as showed in the Fig. 5.12(c), the state $|1\rangle$ is never populated during the evolution, the transition $|0\rangle \rightarrow |2\rangle$ is perfectly performed. We point out that, even if in a different context, we have already encountered adiabatic population transfer between two eigenstates of the system in Ch. 3 using the adiabatic control tools of Ch. 2.

After introducing the general concept of the STIRAP protocol, we will see the detail of the protocol related to our compensation scheme. We denoted $|0\rangle$ as the ground state $|g_j\rangle$, the intermediate level $|1\rangle$ as $|i_j\rangle$ and $|2_j\rangle$ is the excited state, with $j = 1, 2$ representing the two qubits. In our case, the single atom Hamiltonian describing the system in the RWA is written as

$$H_j(t) = \hbar \begin{pmatrix} 0 & \frac{\Omega_p(t)}{2} & 0 \\ \frac{\Omega_p(t)}{2} & -\Delta_1 & \frac{\Omega_s(t)}{2} \\ 0 & \frac{\Omega_s(t)}{2} & -\Delta_2 \end{pmatrix}, \tag{5.27}$$

being the Stokes and Pump pulses respectively

$$\begin{aligned}\Omega_s(t) =&\Omega_0\, e^{-\left(\frac{t+T_1/2}{T_G}\right)^2}\\ \Omega_p(t) =&\Omega_0\, e^{-\left(\frac{t-T_1/2}{T_G}\right)^2},\end{aligned} \tag{5.28}$$

where Ω_0 is the peak of the Rabi frequency, T_1 is the distance between the maxima of the pulses and T_G the width of the Gaussian. Such a Gaussian shape is largely used due to its stability and easy to realize in a laboratory [119, 131].

The state transition that we have seen above can be realized because of the presence of the so-called *dark state* [119, 127], which reads as

$$|D_j(t)\rangle = \cos(\theta(t))|g_j\rangle - \sin(\theta(t))|e_j\rangle\,, \tag{5.29}$$

where $\theta(t) = \arctan(\Omega_p/\Omega_s)$ is the mixing angle. Technically, in atom physics, a *dark state* is a special state which does not absorb or emit photon, that is reason of the word *dark*. Therefore, a system in this state will remain there indefinitely. For our purpose, the importance of this state lies in the fact that it does not couple the intermediate state $|i_j\rangle$ with the other two. This, can be seen from its analytical expression in Eq. (5.29) in which there is no intermediate state $|i_j\rangle$ component. Therefore, preparing the system in the ground state and adiabatically following the dark state, the transfer $|g_j\rangle \rightarrow |e_j\rangle$ can be performed without any non-adiabatic transitions between the states.

As in the single-photon case, in the following we aim at realizing consecutive quantum state transfers with high fidelity.

5.3.2 *Synchronous driving*

For the two-photon excitation model, we consider only the synchronous driving, which means that the computational and correction qubits are driven simultaneously. Before going into the details, we remark that the STIRAP three-level model can be reduced to an effective two-level one by considering large detuning Δ_1. The same procedure has been shown previously in Ch. 3, where in Sec. 3.4 we have reduced a four-level system in a three-level one using the adiabatic elimination method. If, then, we reduce the STIRAP to a two-level system, the compensation scheme that we have studied in the previous sections can be applied. Here, instead, we study the regime of small Δ_1 where such an approximation is not valid. The structure of the period T with STIRAP is defined in Fig. 5.13 where the related population P_{g_1} and the pump and Stokes pulses are shown. The weak adiabatic regime due to parameter that we have chosen, allows the intermediate state to be slightly populated during the transition. This generates the little oscillations visible in the population P_{g_1} of Fig. 5.13. It is worth noting that while the first transition $|g_j\rangle \rightarrow |e_j\rangle$ is realized with counter-intuitive pulse sequence defined above, the second transition $|e_j\rangle \rightarrow |g_j\rangle$ is achieved by inverting the order of the pulses.

Now, having defined the structure of the period T, we repeat it n times as in the sections above. The error, in this case, is defined by the parameter

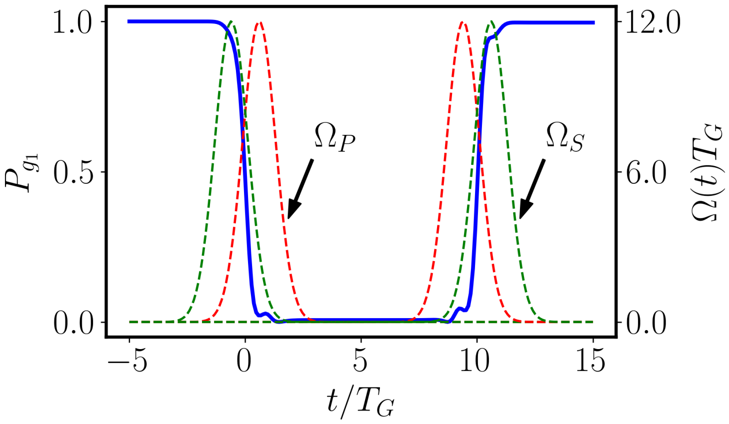

Figure 5.13: Structure of one period T with the STIRAP protocol. To perform the first transition $|g_j\rangle \rightarrow |e_j\rangle$ we use the counter-intuitive pulse sequence, that is first Ω_s and then Ω_p. The second transition $|e_j\rangle \rightarrow |g_j\rangle$, instead, is done by exchanging the previous order of the pulses. This is represented in the figure by the dashed green and red lines for the pulses and the solid blue line for the population of the ground state of the computational qubit. The left vertical axis represents the probability of the ground state P_{g_1}, while the right one represents the pulse amplitude in the dimensionless quantity $\Omega(t)T_g$. The horizontal axis is the time in units of T_g. The oscillations observed in the population P_{g_1} have already been studied in [132] Other simulation parameters are $\Delta_2 = 0, \Delta_1 T_1 = 1.4, T_1 = 1.2T_G, T_2 = 10T_G$. (Figure adapted from [121]).

Δ_1, in particular for the specific value of $\Delta_1 T_1 = 1.4$ the adiabatic regime is not valid anymore. For this case, Fig. 5.14(a) shows the degradation of the fidelity when no compensation is applied. We notice that the population of the intermediate state is not zero as it should be from the Eq. (5.29) of the dark state. On the contrary, when we apply the compensation value of $VT_2 = 2$, the population P_{i_1} is very low and the performance of the system are greatly improved, as shown in Fig. 5.14(b). For both the figures (a) and (b), we assume the interaction always on. Anyway, switching it on only during T_2 does not produce any significant effects, as shown in the App. E.

The fidelity dependence on the detuning, after 5 periods, is very complex and it is shown in Fig. 5.15(a). The dashed blue line represents the infidelity without compensation and the two high peaks determine a very low fidelity. When we apply the compensation $VT_2 = 2$, the behavior is still complex but in correspondence of the two peaks the infidelity is greatly improved. The black line in the figure represents the value of $\Delta_1 T_1 = 1.4$. This means that given the value of the detuning and the number of periods, we can optimize the interaction in order to have a better fidelity. However, a more complete study is performed in Fig. 5.15(b). It represents the height of the peak of the Fourier component $\tilde{P}(\nu_0)$ in the parameters plane $(\Delta_1 T_1, VT_2)$ and, as we have seen in Sec. 5.2.5, it provides the compensation condition independently of the number of the periods. In fact, the black line in the figure, representing the valued $\Delta_1 T_1 = 1.4$ as in the case (a), shows that one

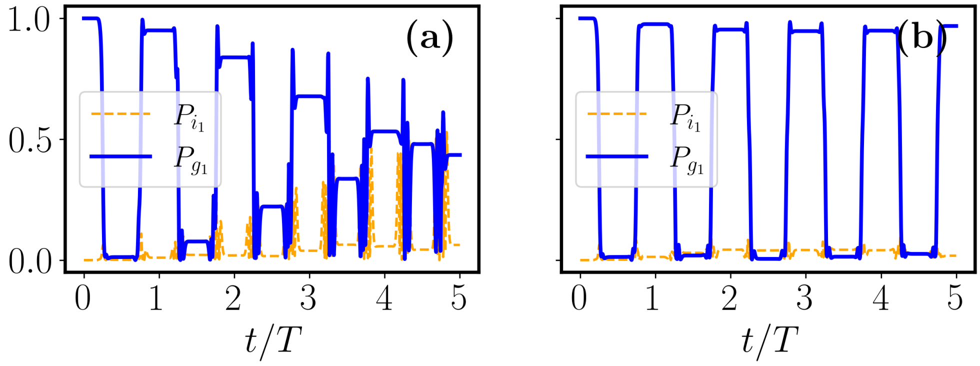

Figure 5.14: Temporal dependence of populations P_{g_1} and P_{i_1} for $n = 5$ periods T at $\Delta_1 T_1 = 1.4$. In (a) no compensation is applied, that is $VT_2 = 0$, and the fidelity becomes worse as the time goes on. At $t/T = 5T$ it is $\mathcal{F}_2 \simeq 0.43$. In (b), instead, the interaction, with value $VT_2 = 2$, improves the fidelity reaching the value of $\mathcal{F}_2 \simeq 0.96$ at $t/T = 5$. The interaction is assumed always on. Other simulation parameters are the same of Fig. 5.13. (Figure taken from [121]).

the compensation value of $VT_2 = 2$ generates high fidelity for that specific value of the detuning.

5.4 REMARKS

In this chapter, we have investigated a new protocol that aim at compensating errors affecting the control parameters of quantum systems. As shown at the beginning in Sec. 5.1, we consider a two interacting qubit model subject to a periodic driving. We denote the first qubit *computational* and the second one *correction* one.The idea is to use this interaction to compensate errors in the driving parameters. We suppose to perform many quantum operations, like a bit flip, periodically in time. We then analyzed the system for tens of periods and such that the error propagates as the time goes on. For the study, we considered two main types of qubit structures: single-photon and two-photon excitation. The first one, presented in Sec. 5.2, has been studied under two different types of driving: asynchronous, explored in Sec. 5.2.2, and synchronous in Sec. 5.2.3. For each of them, we analyzed the rotation-angle error and the rotation-axis error, finding, when possible, an analytical condition for the compensation. What we found is that, optimizing the strength of the interaction for a given period, we can mitigate the effects of the error and also improve the performance. However, optimizing the fidelity for a single period could not be an efficient solution since one cannot be sure it is valid also for larger periods. Therefore, when an analytical condition is not available, it is useful to exploit the Fourier analysis tool. In Sec. 5.2.5, then, we showed how to use Fourier analysis to find the compensation condition independently of the number of periods.

We have seen that the scheme is also valid for a two-photon excitation system, in particular, using the STIRAP protocol described in Sec. 5.3.1. We have seen, then, in Sec. 5.3.2, that also for this scenario it is possible to find

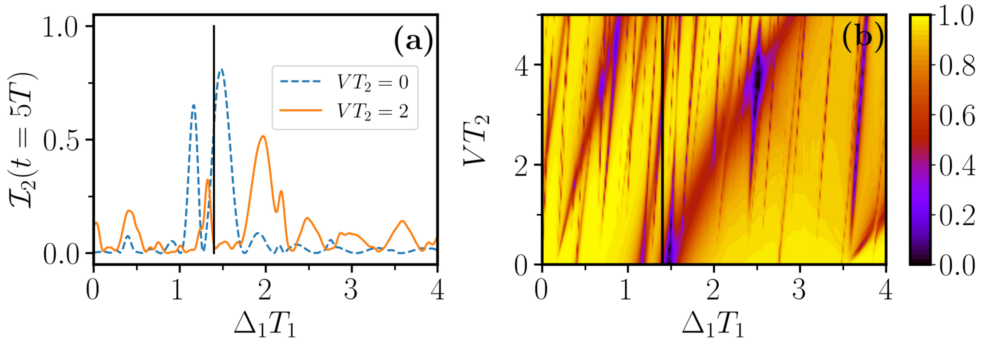

Figure 5.15: In (a) it is shown the infidelity after $5T$, $\mathcal{I}_2(5T)$, as a function of the detuning $\Delta_1 T_1$. The dashed blue line represents the infidelity without compensation, whereas in the solid orange curve a compensation of VT_2 is applied. It can be noticed that at $\Delta_1 T_1 = 1.4$, identified by the black line, the fidelity is highly improved. This specific case has been shown in the Fig. 5.14 above. (b) represents the peak height of $\tilde{P}(\nu_0)$, given by the Fourier analysis introduced in the section above, in the parameter space $(\Delta T_1, VT_2)$. The black line identifies the value of $\Delta_1 T_1 = 1.4$ and it can be seen that also in this case we find the compensation performance seen in (a) and Fig. 5.14. In these plots the interaction is assumed always on. (Figure adapted from [121]).

an interaction value for the compensation. In this case, due to the complexity of the system, only the Fourier analysis was used, confirming the utility of such a tool.

Overall, our compensation scheme is able to improve the fidelity in all the cases that we have studied. However, the complexity of the problem does not allow a further analytical treatment for periods larger than 1. For more complex cases, such as the simultaneously presence of angle and axis error in the single photon excitation must be addressed by resorting to numerical tools.

Our scheme is suitable to be implemented in quantum gates [106, 133] which is the natural extension of the work. Indeed, in this direction, in the next chapter we provide an overview on future development on quantum gates.

Part IV

CONCLUSION AND OUTLOOK

6

CONCLUSIONS AND OUTLOOK

This last chapter of this thesis is dedicated to conclusions and outlook. We first give a summary of the previous chapters, including the problems and results that we have obtained with our solutions, then we provide an overview of possible extensions of our work. In particular, we will concentrate on the implementation of an accelerated adiabatic two-qubit gate relevant for quantum computing.

6.1 SUMMARY

In this thesis we have studied quantum systems affected by errors of different nature. We have addressed the problem essentially from two points of view: adiabatic control tools in Part ii, for close and open quantum systems, and a compensation scheme for unitary errors in our experimental platform based on Rydberg atoms, in part iii. In particular, in Ch. 3, we have optimized a population transfer in a multi-level quantum system. For the purpose, we have specifically designed and optimized three sweep functions in order to maximize the transfer efficiency. The protocols have also been accelerated using the CD driving [33, 34], introduced in Ch. 2, in order to face the problem of the very short life time of the target state. The initial four-level system has been studied in two regimes: firstly in a simplified version by adiabatically eliminating one of the states which did not take part to the evolution and secondly in the full four-level description. In both cases, the application of our designed accelerated adiabatic protocols showed an improvement of the fidelity with respect to the one obtained in the experiment [79]. Our results, then, showed that it is possible to reach a population transfer fidelity very close to 1 in realizing an all-optical switch, in a system more complex than the two-level one of [84], by optimizing the sweep function and applying the corresponding CD Hamiltonian.

While in Ch. 3 the sweep function have been analyzed in a close system environment, neglecting all the decoherence and decay effects, Ch. 4 is dedicated to cover such an aspect. The objective was to study the robustness of three sweep functions in the presence of various sources of noise, especially decoherence and decay by spontaneous emission. We have seen that each sweep function showed different behavior under the effects of the mentioned source of noise. In particular, for a given decoherence channel or decay, one of the sweeps was more robust with respect to the other. The protocols have been tested first on a simple two-level system and then on a two-qubit entangling gate, and the results showed similar behavior for both systems. This means that the adiabatic protocols can be optimized also according to the type of decoherence and decay affecting the system.

In the Part ii we reduced the effects of noise and errors by using adiabatic driving protocols. In the Part iii we tackle the problem from a different perspective. We propose a compensation scheme based on the exploitation of the interaction between two qubits. We considered errors generated by the imperfections in the control parameters which accumulate during a periodic evolution of the system. We first analyzed a simplified model obtained by the assumption that the two qubits can be addressed independently. This reduced the model from four to two levels. The analytical investigation of the fidelity after many periods was not possible. Therefore, under certain assumptions given in Sec. 5.2, we analyzed the analytical expression of the fidelity after one period, for all the error types considered. In some cases, it was possible to derive an compensation relation, denoted as "magic value", such that the interaction perfectly compensates the effects of the errors. Although the numerical simulation showed an agreement with the analytical compensation condition, this method could only optimize the fidelity at a given period. For this reason, we resorted to the Fourier analysis in order to find a more general compensation condition. Indeed, the results showed that such an approach is a powerful tool for eliminating the dependence on the number of periods of the compensation condition. The same approach has been also applied to a more complicated system which showed that the compensation procedure could be generalized to a more realistic systems.

Finally, we believe that our studies confirm that errors in quantum systems can be corrected or mitigated using quantum control tools. We use the adiabatic protocols with CD acceleration method but many others could be used [29]. Additionally, we also provide a new compensation scheme which could be adopted in non-trivial qubit gates, as anticipated in the following, in Sec. 6.2.

6.2 OUTLOOK

The work of this thesis lays the basis for future applications especially in quantum computing scenarios. We aim at correcting and mitigate errors occurring in a quantum system and optimizing the performance of quantum operations using specific tools of quantum control, such as, adiabatic evolution and counterdiabatic driving. The natural extension of our studies, is their implementation to a non-trivial quantum gates. Recently, one of the most promising quantum platforms are Rydberg atoms because of their features and highly controllable degrees of freedom [14]. In this section, we give a brief preview of how our ideas can be connected to quantum gates with Rydberg atoms. First, we introduce some standard quantum gates and then we will see a their adiabatic implementation using Rydberg atoms [26]. Finally, we provide some directions for an implementation of our compensation scheme, presented in Ch. 5.

6.2.1 *CZ and CNOT gates*

Likewise *classical* computers are based on *classical* gates for performing mathematical and logical operations, such as AND, OR, NOT..., *quantum* computers are built using *quantum* gates. The difference lies in the elementary information they have to manage. In fact, while classical gates deal with classical bits, which can assume only two values 0 and 1, their quantum counterpart have to deal with quantum bits, or qubits, which can assume infinite values, or states, given by the superpositions between 0 and 1. In the bra-ket notation this is written as [4]

$$|\psi\rangle = \alpha|0\rangle + \beta|1\rangle \tag{6.1}$$

where $|\psi\rangle$ is the state of the qubit and α and β are two complex coefficients forming the linear superposition such that $|\alpha|^2 + |\beta|^2 = 1$. There exists many gates acting on a qubit and they can be distinguished in the *single* qubit and *multi* qubits gates. The first ones, e.g., X (or NOT), Z and H (Hadamard) gate, are trivial and are easily experimentally realizable. The second, instead, for instance Controlled-NOT and Controlled-Z, are non-trivial and they attract the attention of the physicists because they are key ingredients for building a universal set of quantum gates [4]. From the mathematical point of view, the quantum gates are described by unitary matrices and for the single qubit case, the mentioned exemplary gates, in the basis $|0\rangle \hat{=} \begin{pmatrix} 1 \\ 0 \end{pmatrix}$ and $|1\rangle \hat{=} \begin{pmatrix} 0 \\ 1 \end{pmatrix}$, have the form

$$X = \begin{pmatrix} 0 & 1 \\ 1 & 0 \end{pmatrix}, \qquad Z = \begin{pmatrix} 1 & 0 \\ 0 & -1 \end{pmatrix}, \qquad H = \frac{1}{\sqrt{2}} \begin{pmatrix} 1 & 1 \\ 1 & -1 \end{pmatrix}. \tag{6.2}$$

The X and Z gates, corresponds to the Pauli matrices σ_x and σ_z that we have seen in the previous chapters, while the Hadamard gate is useful for creating a maximal superposition of states. In fact, the application of H on the state $|0\rangle$ gives $H|0\rangle = \frac{1}{\sqrt{2}}(|0\rangle + |1\rangle)$.

The CZ and CNOT gates belong to the two qubits case and they are represented by

$$CZ = \begin{pmatrix} 1 & 0 & 0 & 0 \\ 0 & 1 & 0 & 0 \\ 0 & 0 & 1 & 0 \\ 0 & 0 & 0 & -1 \end{pmatrix}, \qquad CNOT = \begin{pmatrix} 1 & 0 & 0 & 0 \\ 0 & 1 & 0 & 0 \\ 0 & 0 & 0 & 1 \\ 0 & 0 & 1 & 0 \end{pmatrix}. \tag{6.3}$$

These two gates are realized with two qubits such that one controls the operation on the other. For instance, the CZ performs a Z gate on the second qubit only if the first one is in the state $|1\rangle$. Similarly, for the CNOT gate. They have been implemented using various physical quantum systems, such as superconducting qubits [10] and Rydberg atoms [14]. In the next sections, we introduce an implementation of the adiabatic CZ using Rydberg atoms and we will see how such a system can be extended exploiting the control tools that we encountered in in this thesis.

6.2.2 *Adiabatic CZ gate*

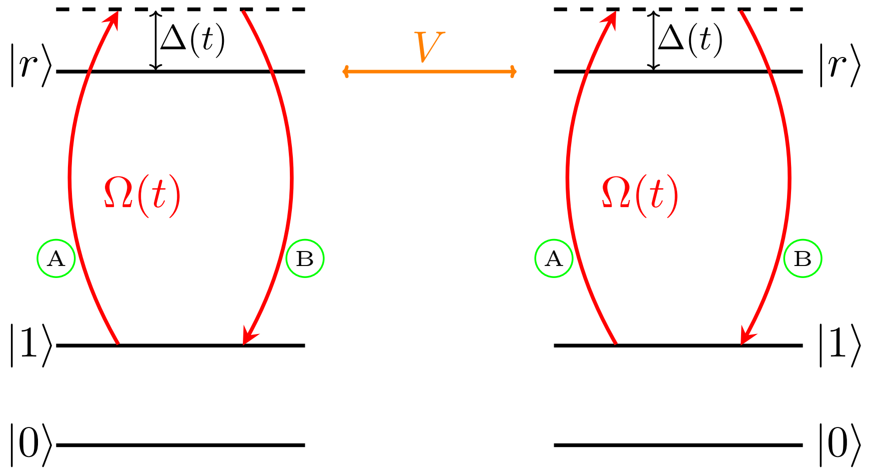

Figure 6.1: Level scheme of the adiabatic protocol for the CZ gate. It consists of two three-levels qubits, the left one is the control qubit and the right one is the target qubit. They have two ground states $|0\rangle$ and $|1\rangle$ and an excited state $|r\rangle$. The protocol consists of two pulses, denoted A and B in the figure, such that the state $|1\rangle$ is excited to the state $|r\rangle$ and a 2π rotation is performed. The pulses are simultaneously applied by means of the Rabi frequency $\Omega(t)$ and detuning $\Delta(t)$. Additionally, the two qubits interact with each other, with strength V, through their $|r\rangle$ state.

As mentioned in the previous section, a lot of quantum gates can be realized. In this section, we concentrate in the CZ quantum gate which is interesting not only because it is a non-trivial two-qubits gate, but also because it can be used, together with two Hadamard gates, for building the CNOT gate [4]. We show an implementation of the CZ gate with Rydberg atoms, which is a platform that we have already studied in Ch. 5, using the adiabatic evolution theory that we have applied in Ch. 3 and 4. The protocol we are going to show has been studied in [26] and its sketch is shown in Fig. 6.1. As we have mentioned in Sec. 5.2.3, we stress the similarity of the present scheme for the adiabatic CZ gate and the one in Fig. 5.3. Figure 6.1 reports two interacting qubits, with interaction strength $V \gg \Omega_{\text{max}}$, consisting of three levels: two ground states $|0\rangle$ and $|1\rangle$ and a Rydberg excited state $|r\rangle$. Their state $|1\rangle$ is excited to $|r\rangle$ using a laser pulse with Rabi frequency $\Omega(t)$, represented by the solid blue line in Fig. 6.2, and detuning $\Delta(t)$ identified by the dashed orange line in Fig. 6.2. Their analytical expressions read as

$$\Omega(t) = \begin{cases} \frac{\Omega_{\text{max}}}{1-a_1}\left(e^{-\frac{(t-T/4)^4}{\tau^4}} - a_1\right) & \text{for} \quad 0 \leq t \leq T/2 \\ \frac{\Omega_{\text{max}}}{1-a_2}\left(e^{-\frac{(t-3T/4)^4}{\tau^4}} - a_2\right) & \text{for} \quad T/2 \leq t \leq T\,, \end{cases} \tag{6.4}$$

$$\Delta(t) = \begin{cases} -\Delta_{\text{max}} \cos(\frac{2\pi t}{T}) & \text{for} \quad 0 \leq t \leq T/2 \\ \Delta_{\text{max}} \cos(\frac{2\pi t}{T}) & \text{for} \quad T/2 \leq t \leq T \end{cases}\,, \tag{6.5}$$

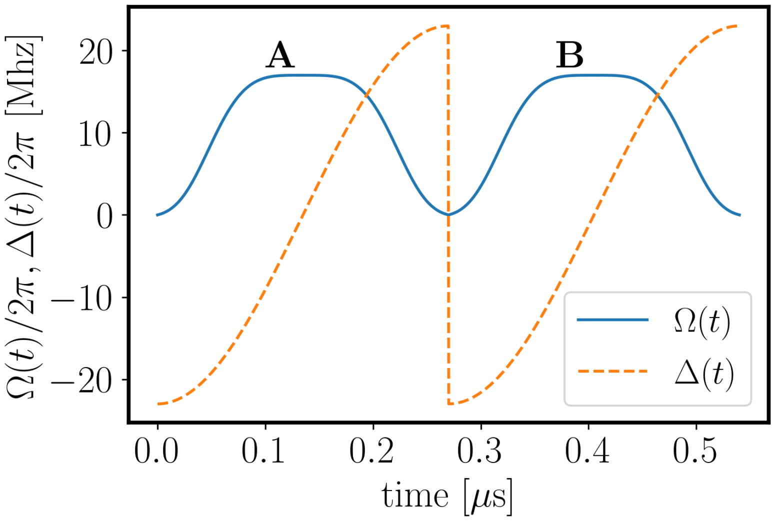

Figure 6.2: Time profile of Rabi frequency $\Omega(t)$, represented by the solid blue line, and the detuning $\Delta(t)$ represented by the dashed orange line. The pulse $\Omega(t)$ is composed of two pulses ARP A and B, corresponding to the pulses A and B in Fig. 6.1. The total period is $T = 0.54$ μs, the maximum Rabi frequency is $\Omega_{\max}/2\pi = 17$ MHz and maximum detuning $\Delta_{\max}/2\pi = 23$ MHz.

where $T = 0.54$ μs is the total duration of the pulse, $\tau = 0.175\,T$ is the life time of the Rydberg level $|r\rangle$, $\Omega_{\max}$ and $\Delta_{\max}$ are the maximum Rabi frequency and detuning respectively, and a_1 and a_2 are constants chosen such that $\Omega(0) = \Omega(T) = 0$.

The pulse $\Omega(t)$, composed of two ARP (Adiabatic Rapid Passage) pulses denoted A and B in Fig. 6.1 with the corresponding time shape in Fig. 6.2, is simultaneously applied to both the qubits, as in our case of Sec. 5.2.3, and it realizes a 2π rotation. Taking into account the computational basis $\{|00\rangle, |01\rangle, |10\rangle, |11\rangle\}$, the states acquire the phases $\{1, \phi_1, \phi_1, \phi_2\}$ respectively. The state $|00\rangle$ is a dark state with respect to the evolution since is not coupled with the field and therefore it does not acquire any phase; the states $|01\rangle$ and $|10\rangle$ are symmetric and therefore they acquire the same phase ϕ_1, while the state $|11\rangle$ acquires a phase ϕ_2 which depends on the Rydberg blockade condition $V \gg \Omega_{\max}$. With the $\Omega(t)$ pulse, the phases ϕ_1 and ϕ_2 will be equal to π. Therefore, the resulting matrix of the adiabatic CZ gate in basis $\{|00\rangle, |01\rangle, |10\rangle, |11\rangle\}$ will be

$$CZ_{ad} = \begin{pmatrix} 1 & 0 & 0 & 0 \\ 0 & -1 & 0 & 0 \\ 0 & 0 & -1 & 0 \\ 0 & 0 & 0 & -1 \end{pmatrix}. \tag{6.6}$$

Notice that the difference between the adiabatic CZ of Eq. (6.6) and the one in Eq. (6.3) is only an irrelevant global phase.

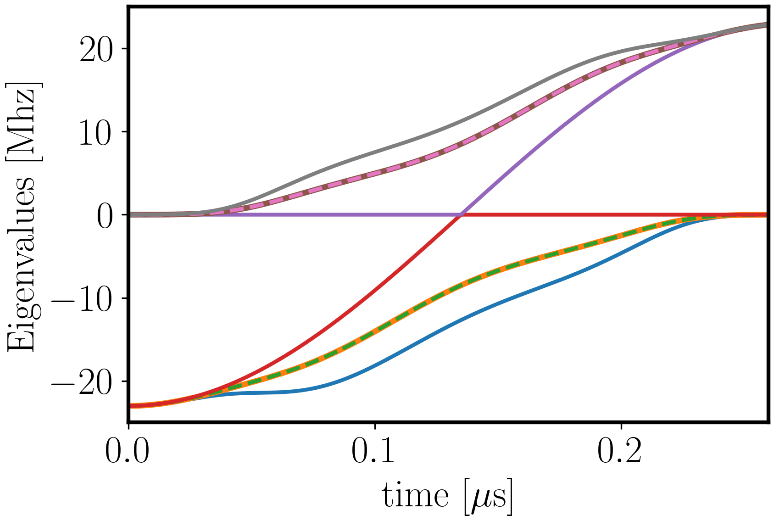

Figure 6.3: Half-spectrum ($0 \leq t \leq T/2$) of instantaneous eigenvalues of the adiabatic CZ gate. In the figure, only 8 of 9 eigenvalues are depicted. The other one is much higher and it is not relevant for our purpose. All the 8 eigenvalues are degenerate at $t = 0$ and $t = T/2$. Moreover, two couples of them are degenerate for the entire evolution. The other half of the spectrum, $T/2 \leq t \leq T/2$ is identical to the first half. Simulation parameters are $T = 0.54$ μs, $\tau = 0.175\,T$, $a_1 = a_2 = 0.01553078$, $\Delta_{\max}/2\pi = 23$ Mhz, $\Omega_{\max}/2\pi = 17$ Mhz.

6.2.3 *Counterdiabatic CZ*

The gate just showed is realized with adiabatic pulses and it already reaches fidelities > 0.999. Therefore, a possible extension is the application of CD correction in order to speed up the evolution and reducing the time for performing a *CZ* operation. Having the possibility of implementing very fast quantum gates allows one to perform many quantum operations within the decoherence time of the system, and therefore execute much complex algorithm. Hence, for computing the H_{CD} Hamiltonian, we study the instantaneous eigenvalues structure depicted in Fig. 6.3. In the figure only 8 of 9 eigenvalues are shown because one of them is much higher than the others, and we can neglect it for our purpose. The 8 eigenvalues are degenerate at $t = 0$ and $t = T/2$ while two of them are degenerate for the entire evolution. This could be a problem for the computation of H_{CD} in Eq. (2.25), since it requires that all the eigenvalues have to be non degenerate at any time. However, as extensively explained in the Bachelor thesis of Tim Ehret [134], in our special case the problem does not arises because the matrix representing the entire system can be split into blocks which are independent. Therefore, the CD driving works as it should and the adiabatic evolution is accelerated. Additionally, another advantage of such an implementation is related to the unwanted dynamical phase generated by the non-perfect Rydberg blockade regime. It turned out that the CD term also compensates such a phase improving, then, the performance.

Another way to compensate the unwanted dynamical phase is to use two single-qubit phase gates. Such a phase gate produces an energy shift such that it cancels out the unwanted phase. In this direction, the compensation scheme presented in Ch. 5 can be explored. In our same synchronous driving of Sec. 5.2.3, the interaction was used to compensate an extra phase generated by the imperfection in the control parameters. Therefore, keeping the interaction range within the Rydberg blockade regime, that is $V \gg \Omega_{\mathrm{max}}$, the fidelity can be studied as a function of the interaction strength. Alternatively, also the asynchronous scheme could be investigated for this purpose.

In the end, improving the performance of the CZ gate allows us to built a CNOT gate, using two Hadamard gate and one CZ [4, 135], and consequently improving fidelity of a quantum error correction schemes based on the CNOT gate [16, 17]. In this direction, a more detailed studied has been developed in the Bachelor thesis of Tim Ehret [134].

Part V

APPENDIX

A

SWEEP FUNCTIONS DERIVATION

In Sec. 2.3, we have introduced the sweep functions that we used in the Ch. 3 and 4. This appendix is dedicated to show the main steps for deriving the RC and PL protocols.

A.1 ROLAND–CERF

The RC has been already calculated and studied in [35, 56, 57]. However, we followed the mention references to derive the RC in our problems and, therefore, the aim of this section is to review the main steps for the derivation. In particular, we consider an exemplary case of the two level system described by an Hamiltonian similar to the one in Eq. (2.26). For this reason, let us consider a two level system governed by the Hamiltonian:

$$H(t) = \alpha f(t)\sigma_z + \Omega\sigma_x \,, \tag{A.1}$$

where $\alpha > 0$ and Ω are the same parameters defined in Eq. 2.13. Let us compute, then, the gap between the eigenenergies of systems E_+ and E_-, corresponding to the instantaneous excited and ground eigenstates $|\psi_+[f(t)]\rangle$ and $|\psi_-[f(t)]\rangle$, respectively:

$$\Delta E[f(t)] = E_+[f(t)] - E - [f(t)] = 2\alpha\sqrt{f^2(t) + \left(\frac{g}{\alpha}\right)^2} \,, \tag{A.2}$$

$$|\psi_\pm\rangle = \frac{1}{\sqrt{1 + \alpha^2 \left|\frac{\sqrt{f^2(t)+(\Omega/\alpha)^2} \mp f(t)}{\Omega}\right|^2}} \begin{pmatrix} 1 \\ \pm\frac{\sqrt{f^2(t)+(\Omega/\alpha)^2} - f(t)}{\Omega} \end{pmatrix} . \tag{A.3}$$

Notice that the eigenvalues, as well as the eigenstates, depend on the function $f(t)$ which is the unknown that we want to find.

Now, using the instantaneous eigenstates in Eq. (A.3) and computing $\partial_f H$, we can impose the local adiabatic condition as follows [57, 136]:

$$\left|\frac{df}{dt}\right| \frac{|\langle\psi_+(f)|\partial_f H|\psi_-(f)|\rangle|}{(\Delta E)^2} < \epsilon \,. \tag{A.4}$$

We also demand that $f(t)$ is monotonically decreasing $\frac{df}{dt} \leq 0$ such that we obtain:

$$\frac{dt}{df} = -\frac{|g|}{4\epsilon\alpha^2\left[\left(\frac{g}{\alpha}\right)^2 + f^2(t)\right]^{3/2}} \,, \tag{A.5}$$

where we consider the threshold value from Eq. (A.4). For convenience, we first integrate Equation (A.5) between $f(0) = f_0 > 0$ and $f(t_f) = -f_0$, obtaining the expression for the final time as follows:

$$t_f = \frac{f_0}{2\epsilon|g|\sqrt{\left(\frac{g}{\alpha}\right)^2 + f_0^2}}\,. \tag{A.6}$$

Having the final time t_f, we can now find $f(t)$ by integrating again Equation (A.5), this time from $f(0)$ to $f(t)$, and then by inverting the resulting function $t(f)$. The RC protocol then reads as follows:

$$f(t) = \frac{\left(\frac{t_f}{2} - t\right) 4\epsilon|g|^2}{\alpha\sqrt{1 - \left(\frac{t_f}{2} - t\right)^2 16\epsilon^2|g|^2}}\,. \tag{A.7}$$

Finally, using the same change of variable as in Sec. 2.1.1 and rearranging the expression we obtain exactly the Eq. (2.38)

$$f_{RC}(\tau) = \frac{(1-2\tau)f_0}{\sqrt{1 + 4\alpha_g^2 f_0^2 \tau(1-\tau)}}\,. \tag{A.8}$$

We have shown a quite procedure for a two level system but it can be used also in other cases. In fact, in Ch. 3, we computed the RC by considering only the two-level subsystem consisting of the states $|1\rangle$ and $|T\rangle$. Repeating, then, the procedure just shown, we obtain the RC for the specific case.

A.2 POLYNOMIAL

The PL sweep function is derived using the BCMs [55] mentioned in Sec. 2.3. As extensively explained in the PhD dissertation [51], we are looking for a sweep function whose first n derivatives are null at the beginning and at the end of evolution [137]. Typically, such features are present in the polynomial functions. Therefore, for the one-qubit case studied in Ch. 4, we consider a polynomial of the form

$$p(\tau) = 1 + a\tau^3 + b\tau^4 + c\tau^5 + d\tau^6 + e\tau^7\,, \tag{A.9}$$

with $\tau \in [0, 1]$. Thus, we need to find the values of the five coefficients a, b, c, d, e requiring that the first three derivatives are 0, that the values at the end of the protocol $\tau = 1$ is $p(1) = -1$ and that it is 0 at the avoided crossing, that is $p(1/2) = 0$. The request of having $p(0) = 1$ is already fulfilled from the definition in Eq. (A.9). In formula, we have to solve the system

$$\begin{cases} a + b + c + d + e + 1 = -1 \\ 3a + 6d = 0 \\ 4b + 5c + 7e = 0 \\ 6a + 12b + 20c + 30d + 42e = 0 \\ \frac{a}{8} + \frac{b}{16} + \frac{c}{32} + \frac{d}{64} + \frac{e}{128} + 1 = 0\,. \end{cases} \tag{A.10}$$

The solution provide the coefficients of the polynomial function in Eq. (2.37) with the temporal profile showed by the dashed red line of Fig. 4.1(a).

B

DERIVATION OF 4 × 4 HAMILTONIAN OF SEC. 3.2

In the present appendix we show the main analytical calculations useful for a better understanding of the system studied in Ch. 3. In particular, first we start writing the Hamiltonian in the unperturbed basis with the states $|S_0\rangle$and$|T_0\rangle$, and we derive a simpler description in a rotating frame with the Rotating-Wave Approximation (RWA). Second, we change the basis in the perturbed basis with the states $|S\rangle$ and $|T\rangle$ as in the experimental reference paper [79]. Finally, we show the main steps of the adiabatic elimination procedure, useful for the reduced system described in Sec. 3.4.

B.1 UNPERTURBED BASIS DESCRIPTION

In this brief section, we write the Hamiltonian of the system in the lab frame. We consider the unperturbed basis $\{|1\rangle, |S_0\rangle, |T_0\rangle, |2\rangle\}$

$$\hat{H} = \hat{H}_0 + \hat{H}_{so} = \begin{pmatrix} E_1 & \Omega_p \cos(\omega_p t) & 0 & 0 \\ \Omega_p \cos(\omega_p t) & E_{S_0} & V & 0 \\ 0 & V & E_{T_0} & \Omega_c \cos(\omega_c t) \\ 0 & 0 & \Omega_c \cos(\omega_c t) & E_2 \end{pmatrix}, \tag{B.1}$$

where E_1, E_{S_0}, E_{T_0} and E_2 are the energies of the states $|1\rangle, |S_0\rangle, |T_0\rangle$ and $|2\rangle$, respectively. Ω_p and Ω_c are the probe and the control Rabi frequencies, V is the spin-orbit coupling strength defined in Eq. (3.1) and cos function represents the laser and ω_p and ω_c are the corresponding frequencies. Now we choose the level $|T_0\rangle$ as the zero energy point, so we obtain

$$\hat{H} = \hat{H}_0 + \hat{H}_{so} = \begin{pmatrix} \omega_1 + \Delta_0 & \Omega_p \cos(\omega_p t) & 0 & 0 \\ \Omega_p \cos(\omega_p t) & \Delta_0 & V & 0 \\ 0 & V & 0 & \Omega_c \cos(\omega_c t) \\ 0 & 0 & \Omega_c \cos(\omega_c t) & \omega_2 \end{pmatrix} \tag{B.2}$$

where $\Delta_0 = E_{S_0} - E_{T_0}$, $\omega_1 = E_{S_0} - E_1$ and $\omega_2 = E_2 - E_{T_0}$. Now, we simplify the expression of the matrix of Eq. (B.2) by applying the RWA.

B.1.1 *Rotating Frame and RWA*

In this section, we apply a unitary transformation $U(t)$ for changing the system reference and using the rotating frame of the lasers. For simplicity we do not use the hat notation of the operators.

Consider the transformation $U(t) = \begin{pmatrix} e^{-i\omega_p t} & 0 & 0 & 0 \\ 0 & 1 & 0 & 0 \\ 0 & 0 & 1 & 0 \\ 0 & 0 & 0 & e^{i\omega_c t} \end{pmatrix}$. The new Hamiltonian is found using the relation $H' = UHU^\dagger + i\dot{U}U^\dagger$. Let us, then, evaluate the two terms separately.

1. The first term is given by the matrix product

$$
\begin{aligned}
UHU^\dagger = &\begin{pmatrix} e^{-i\omega_p t} & 0 & 0 & 0 \\ 0 & 1 & 0 & 0 \\ 0 & 0 & 1 & 0 \\ 0 & 0 & 0 & e^{i\omega_c t} \end{pmatrix} \times \\
\times &\begin{pmatrix} \omega_1 + \Delta_0 & \frac{\Omega_p}{2}\left(e^{-i\omega_p t} + e^{i\omega_p t}\right) & 0 & 0 \\ \frac{\Omega_p}{2}\left(e^{-i\omega_p t} + e^{i\omega_p t}\right) & \Delta_0 & V & 0 \\ 0 & V & 0 & \frac{\Omega_c}{2}\left(e^{-i\omega_c t} + e^{i\omega_c t}\right) \\ 0 & 0 & \frac{\Omega_c}{2}\left(e^{-i\omega_c t} + e^{i\omega_c t}\right) & \omega_2 \end{pmatrix} \times \\
\times &\begin{pmatrix} e^{i\omega_p t} & 0 & 0 & 0 \\ 0 & 1 & 0 & 0 \\ 0 & 0 & 1 & 0 \\ 0 & 0 & 0 & e^{-i\omega_c t} \end{pmatrix} = \\
= &\begin{pmatrix} \omega_1 + \Delta_0 & \frac{\Omega_p}{2}\left(1 + e^{-i2\omega_p t}\right) & 0 & 0 \\ \frac{\Omega_p}{2}\left(e^{i2\omega_p t} + 1\right) & \Delta_0 & V & 0 \\ 0 & V & 0 & \frac{\Omega_c}{2}\left(e^{-i2\omega_c t} + 1\right) \\ 0 & 0 & \frac{\Omega_c}{2}\left(1 + e^{i2\omega_c t}\right) & \omega_2 \end{pmatrix}
\end{aligned}
\tag{B.3}
$$

   Now using the RWA we can neglect the exponentials $e^{\pm i2\omega_{p,c}t}$ since they rotates much faster than the reference frequencies and we obtain the much simpler matrix

$$
UHU^\dagger = \begin{pmatrix} \omega_1 + \Delta_0 & \frac{\Omega_p}{2} & 0 & 0 \\ \frac{\Omega_p}{2} & \Delta_0 & V & 0 \\ 0 & V & 0 & \frac{\Omega_c}{2} \\ 0 & 0 & \frac{\Omega_c}{2} & \omega_2 \end{pmatrix}. \tag{B.4}
$$

2. The other term of the transformation, instead, is

$$
i\dot{U}U^\dagger = i\begin{pmatrix} -i\omega_p e^{-i\omega_p t} & 0 & 0 & 0 \\ 0 & 0 & 0 & 0 \\ 0 & 0 & 0 & 0 \\ 0 & 0 & 0 & i\omega_c e^{i\omega_c t} \end{pmatrix}\begin{pmatrix} e^{i\omega_p t} & 0 & 0 & 0 \\ 0 & 1 & 0 & 0 \\ 0 & 0 & 1 & 0 \\ 0 & 0 & 0 & e^{-i\omega_c t} \end{pmatrix} = \begin{pmatrix} \omega_p & 0 & 0 & 0 \\ 0 & 0 & 0 & 0 \\ 0 & 0 & 0 & 0 \\ 0 & 0 & 0 & -\omega_c \end{pmatrix}. \tag{B.5}
$$

Finally, adding the two results in Eqs. (4) and (5), the Hamiltonian in the rotating frame and with the RWA reads

$$H' = UHU^{\dagger} + i\dot{U}U^{\dagger} = \begin{pmatrix} \delta_p + \Delta_0 & \frac{\Omega_p}{2} & 0 & 0 \\ \frac{\Omega_p}{2} & \Delta_0 & V & 0 \\ 0 & V & 0 & \frac{\Omega_c}{2} \\ 0 & 0 & \frac{\Omega_c}{2} & -\delta_c \end{pmatrix}, \tag{B.6}$$

where $\delta_p = \omega_p - \omega_1$ and $\delta_c = \omega_c - \omega_2$ are the two detunings.

B.2 PERTURBED BASIS DESCRIPTION

In order to be consistent with the treatment in [79], in our simulation we used the Hamiltonian in the perturbed basis. Therefore, in this section we show the main steps to derive such an Hamiltonian.

Let us write the Hamiltonian of Eq. (B.8) in the basis $(|1\rangle, |S\rangle, |T\rangle, |2\rangle)$ where

$$|S\rangle = \alpha|S_0\rangle - \beta|T_0\rangle \qquad |T\rangle = \beta|S_0\rangle + \alpha|T_0\rangle\,. \tag{B.7}$$

Using $A = \begin{pmatrix} 1 & 0 & 0 & 0 \\ 0 & \alpha & \beta & 0 \\ 0 & -\beta & \alpha & 0 \\ 0 & 0 & 0 & 1 \end{pmatrix}$ as the change-of-basis matrix, the transformation is

$$\tilde{H} = AHA^{-1} = \begin{pmatrix} \delta_p + \Delta_0 & \alpha\frac{\Omega_p}{2} & -\beta\frac{\Omega_p}{2} & 0 \\ \alpha\frac{\Omega_p}{2} & \alpha^2\Delta_0 + 2\alpha\beta V & (\alpha^2-\beta^2)V - \alpha\beta\Delta_0 & \beta\frac{\Omega_c}{2} \\ -\beta\frac{\Omega_p}{2} & (\alpha^2-\beta^2)V - \alpha\beta\Delta_0 & \beta^2\Delta_0 - 2\alpha\beta V & \alpha\frac{\Omega_c}{2} \\ 0 & \beta\frac{\Omega_c}{2} & \alpha\frac{\Omega_c}{2} & -\delta_c \end{pmatrix}. \tag{B.8}$$

We should evaluate the new energy splitting between the states $|S\rangle$ and $|T\rangle$. So let us diagonalize the subsystem 2×2, obtaining

$$E_{S,T} = \frac{1}{2}\left[\Delta_0 \pm \sqrt{\left[(\alpha^2-\beta^2)^2 + 4\alpha^2\beta^2\right]\left[\Delta_0^2 + 4V^2\right]}\right]. \tag{B.9}$$

Since we have performed a parametric diagonalization of the subsystem, with parameters α and β, the relation between Δ_{so} and V with Δ_0 is found by imposing the two conditions: (i) energy splitting equal to Δ_{so} and (ii) off-diagonal elements of Eq. (B.8) equal to 0, which read

$$\Delta_{so} = E_S - E_T = \sqrt{\left[(\alpha^2-\beta^2)^2 + 4\alpha^2\beta^2\right]\left[\Delta_0^2 + 4V^2\right]} \tag{B.10}$$

$$V(\alpha^2-\beta^2) - \alpha\beta\Delta_0 = 0\,. \tag{B.11}$$

Solving for V in Eq. (B.11) and substituting it in the Eq. (B.10), we find the relations for V and Δ_0 which correspond to the Eqs. (3) and (4) of [73]

$$\Delta_0 = \left(\alpha^2 - \beta^2\right) \Delta_{so} \tag{B.12}$$

$$V = \alpha\beta\Delta_{so} \, . \tag{B.13}$$

At this point, substituting the latter relations of the Eqs. (B.12) and (B.13) into the Eq. (B.8), the Hamiltonian finally reads

$$\tilde{H} = \begin{pmatrix} \delta_p + \Delta_{so} & \alpha\frac{\Omega_p}{2} & -\beta\frac{\Omega_p}{2} & 0 \\ \alpha\frac{\Omega_p}{2} & \Delta_{so} & 0 & \beta\frac{\Omega_c}{2} \\ -\beta\frac{\Omega_p}{2} & 0 & 0 & \alpha\frac{\Omega_c}{2} \\ 0 & \beta\frac{\Omega_c}{2} & \alpha\frac{\Omega_c}{2} & -\delta_c \end{pmatrix} , \tag{B.14}$$

where, in the new basis with $|S\rangle$ and $|T\rangle$, we took the state $|T\rangle$ as the zero energy level.

C

OPTIMAL CORRECTION FOR SYNCHRONOUS DRIVING

In Sec. 5.2.2.1, we have stated that for the angle rotation error it possible to prove that the magic value in Eq. (5.14) provides a perfect compensation of the error, independent of the value of ϵ. Indeed, in this appendix, we show that for $VT_2 = \pi$, the evolution operator after one period $T = 2T_1 + 2T_2$, that is $U(T)$, is equivalent to the identity operator. From Eqs. (5.8) and (5.9), setting $\delta = 0$, we recall that

$$\begin{aligned} U(T) &= U_2(T_2)U_1(T_1)U_2(T_2)U_1(T_1) = \\ &= e^{-iVT_2|e_1\rangle\langle e_1|}e^{-i\frac{\Omega T_1}{2}\sigma_{x_1}}e^{-iVT_2|e_1\rangle\langle e_1|}e^{-i\frac{\Omega T_1}{2}\sigma_{x_1}}\,, \end{aligned} \tag{C.1}$$

where σ_{x_1} is the X Pauli matrix applied to the first qubit. Knowing that $\Omega T_1 = \pi(1+\epsilon)$ and $VT_2 = \pi$, we can substitute such values in the Eqs. (5.8) and (5.9). In this way, the multiplication of the first three factors of Eq. (C.1) yield to the operator

$$\begin{pmatrix} \cos(\frac{pi}{2}(1+\epsilon)) & i\sin(\frac{pi}{2}(1+\epsilon)) \\ i\sin(\frac{pi}{2}(1+\epsilon)) & \cos(\frac{pi}{2}(1+\epsilon)) \end{pmatrix} = e^{i\frac{\Omega T_1}{2}\sigma_{x_1}}\,. \tag{C.2}$$

Finally, the time evolution operator $U(T)$ can be written as

$$U(T) = e^{i\frac{\Omega T_1}{2}\sigma_{x_1}}e^{-i\frac{\Omega T_1}{2}\sigma_{x_1}} = \mathbb{1}\,. \tag{C.3}$$

Hence, we see that for the specific magic value $VT_2 = \pi$, the unitary operator is independent of the error ϵ and it produces an identity operation which leaves the system unchanged.

D

MODIFICATION OF THE LZ PROTOCOL

In Sec. 3.3 we observed that the LZ protocol produces two avoided crossings instead of one, as shown in Fig. 3.2(a). This could be a problem in the adiabatic evolution as explained in the following.

The initial state of the system is $|1\rangle$, therefore, at the beginning of the evolution, that is at time $t/t_f = 0$, we start from the solid/blue line. Then, adiabatically following the solid/blue instantaneous eigenstate, at the end of the protocol, that is at $t/t_f = 1$, we would end up in the state $|T\rangle$ and the population transfer from $|1\rangle$ to $|T\rangle$ would be complete. However, using the Eq. (2.36) as it is, also the state $|S\rangle$ will be populated if the evolution is not sufficiently slow. This problem is shown in Fig. D.1(a), where we can see that the state $|S\rangle$ has approximately 30% of the population. The solution is to modify the sweep function as follows

$$f'_{LZ}(\tau) = \begin{cases} f_{LZ}(\tau) & \text{for} \qquad 0 < \tau < \bar{\tau} \\ f_{LZ}(\bar{\tau}) & \text{for} \qquad \bar{\tau} < \tau < 1 \end{cases} \tag{D.1}$$

where $\bar{\tau}$ is a fixed time after which the LZ protocol is constant. Choosing $\bar{\tau} = 0.3$ we obtain the population distribution as in Fig. D.1(b) where the state $|S\rangle$ remains unpopulated. However, the price to pay for this is the generation of coherent oscillations between $|1\rangle$ and $|S\rangle$ around the centered value of the case (a), as can be observed in the Fig. D.1(b). Notice that, in both cases, the fidelity is around 70% but the time needed to reach such a value is much longer than the life time $1/\Gamma_T$ of the target state $|T\rangle$. In the simulations, the modified LZ protocol described here has been used such that the state $|S\rangle$ is not populated.

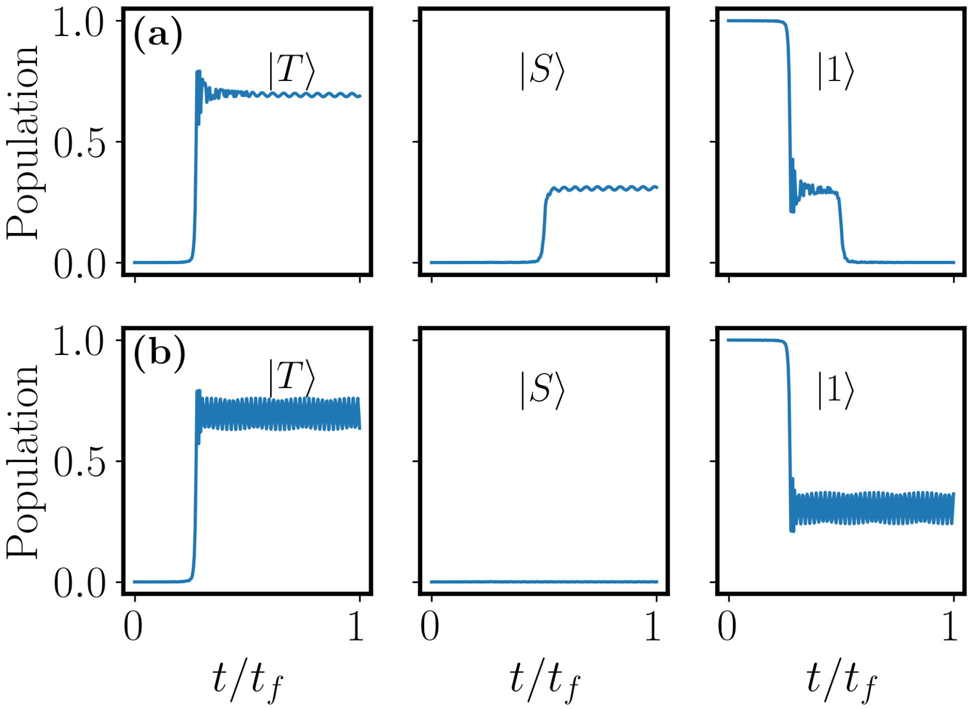

Figure D.1: Populations of the three levels $|T\rangle, |S\rangle$ and $|1\rangle$ for (a) LZ protocol in Eq. (2.36) and (b) modified LZ of Eq. (D.1). In the case (a), the state $|S\rangle$ is populated because of the second avoided crossing visible in Fig. 3.2(a). In the case (b), the state $|S\rangle$ remains unpopulated but coherent oscillations appear between the states $|T\rangle$ and $|1\rangle$. Simulation parameters are $\delta_c = 30\ \text{ns}^{-1}$, $a = 10\ \text{ns}^{-1}$ and $t_f = 2000$ ns.

E

INTERACTION IN STIRAP

In Sec. 5.3.2 we have studied the case in which the interaction is always present in both the time ranges of the evolution, T_1 and T_2. Then, we stated that if the interaction is off during T_1, we do not observe any significant change. Therefore, in this appendix, we address such a problem showing an exemplary plot in Fig. E.1. In particular, Fig. E.1(a) report the behavior of the interaction, as a function of the time, compared with the pulses profile. In this case, we turned of the interaction V during T_1, where we defined T_1 as the distance between the two peak pulses. During T_2, we set $VT_2 = 2$ and the result is reported in Fig. E.1(b), which must be compared with Fig. 5.14(b). As we observe, turning V off during T_1 does not produce any significant effect and, therefore, the results showed in Sec. 5.3.2 are valid also for the case presented in this section.

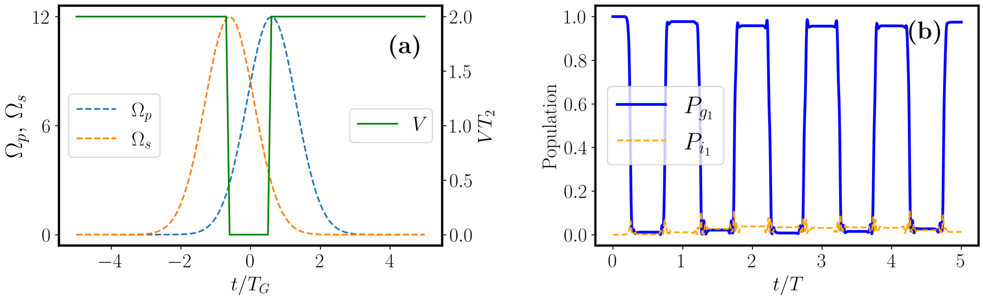

Figure E.1: (a) Temporal profile of the Pump and Stokes pulses, represented by the dashed orange and blue lines, respectively, and of the interaction V denoted with the green solid line. In contrast to the case in Sec. 5.3.1, here we set $V = 0$ during T_1. The left scale refers to the pulses Ω_p and Ω_s while the one on the right refers to the interaction. (b) Population of the ground and intermediate states, as in Fig. 5.14(b). Comparing the case in (b) of the present figure with that of Fig. 5.14(b) we see that the two results are very similar. Apart from the interaction, other simulation parameters are the same of Fig. 5.14.

BIBLIOGRAPHY

[1] Walther Gerlach and Otto Stern. "Der experimentelle Nachweis der Richtungsquantelung im Magnetfeld." In: *Zeitschrift für Physik* 9.1 (1922), pp. 349–352. ISSN: 0044-3328. DOI: 10.1007/BF01326983.

[2] Richard P Feynman. "Simulating physics with computers." In: *International Journal of Theoretical Physics* 21.6 (1982), pp. 467–488. ISSN: 1572-9575. DOI: 10.1007/BF02650179.

[3] "40 years of quantum computing." In: *Nature Reviews Physics* 4.1 (2022), p. 1. ISSN: 2522-5820. DOI: 10.1038/s42254-021-00410-6.

[4] M. A. Nielsen and I. L. Chuang. *Quantum Computation and Quantum Information*. Cambridge University Press, 2000. ISBN: 9780521635035.

[5] David Deutsch and Richard Jozsa. "Rapid solution of problems by quantum computation." In: *Proceedings of the Royal Society of London. Series A: Mathematical and Physical Sciences* 439.1907 (1992), pp. 553–558. DOI: 10.1098/rspa.1992.0167.

[6] P.W. Shor. "Algorithms for quantum computation: discrete logarithms and factoring." In: *Proceedings 35th Annual Symposium on Foundations of Computer Science*. 1994, pp. 124–134. DOI: 10.1109/SFCS.1994.365700.

[7] Lov K. Grover. "A Fast Quantum Mechanical Algorithm for Database Search." In: *Proceedings of the Twenty-Eighth Annual ACM Symposium on Theory of Computing*. STOC '96. Philadelphia, Pennsylvania, USA: Association for Computing Machinery, 1996, 212–219. ISBN: 0897917855. DOI: 10.1145/237814.237866.

[8] Lov K. Grover. "Quantum Mechanics Helps in Searching for a Needle in a Haystack." In: *Phys. Rev. Lett.* 79 (2 1997), pp. 325–328. DOI: 10.1103/PhysRevLett.79.325.

[9] Frank et al. Arute. "Quantum supremacy using a programmable superconducting processor." In: *Nature* 574.7779 (2019), pp. 505–510. ISSN: 1476-4687. DOI: 10.1038/s41586-019-1666-5.

[10] Morten Kjaergaard, Mollie E. Schwartz, Jochen Braumüller, Philip Krantz, Joel I.-J. Wang, Simon Gustavsson, and William D. Oliver. "Superconducting Qubits: Current State of Play." In: *Annual Review of Condensed Matter Physics* 11.1 (2020), pp. 369–395. DOI: 10.1146/annurev-conmatphys-031119-050605.

[11] Alexandre Blais, Jay Gambetta, A. Wallraff, D. I. Schuster, S. M. Girvin, M. H. Devoret, and R. J. Schoelkopf. "Quantum-information processing with circuit quantum electrodynamics." In: *Phys. Rev. A* 75 (3 2007), p. 032329. DOI: 10.1103/PhysRevA.75.032329.

[12] A. Blais, R.-S. Huang, A. Wallraff, S. M. Girvin, and R. J. Schoelkopf. “Cavity quantum electrodynamics for superconducting electrical circuits: An architecture for quantum computation.” In: *Phys. Rev. A* 69 (6 2004), p. 062320. DOI: `10.1103/PhysRevA.69.062320`.

[13] J. I. Cirac and P. Zoller. “Quantum Computations with Cold Trapped Ions.” In: *Phys. Rev. Lett.* 74 (20 1995), pp. 4091–4094. DOI: `10.1103/PhysRevLett.74.4091`.

[14] M. Morgado and S. Whitlock. “Quantum simulation and computing with Rydberg-interacting qubits.” In: *AVS Quantum Science* 3.2 (2021), p. 023501. DOI: `10.1116/5.0036562`.

[15] D. Jaksch, J. I. Cirac, P. Zoller, S. L. Rolston, R. Côté, and M. D. Lukin. “Fast Quantum Gates for Neutral Atoms.” In: *Phys. Rev. Lett.* 85 (10 2000), pp. 2208–2211. DOI: `10.1103/PhysRevLett.85.2208`.

[16] Simon J Devitt, William J Munro, and Kae Nemoto. “Quantum error correction for beginners.” In: *Reports on Progress in Physics* 76.7 (2013), p. 076001. DOI: `10.1088/0034-4885/76/7/076001`.

[17] Barbara M. Terhal. “Quantum error correction for quantum memories.” In: *Rev. Mod. Phys.* 87 (2 2015), pp. 307–346. DOI: `10.1103/RevModPhys.87.307`.

[18] D. D’Alessandro. *Introduction to Quantum Control and Dynamics*. Chapman & Hall/CRC Applied Mathematics & Nonlinear Science. CRC Press, 2007. ISBN: 9781584888833.

[19] D. Dong and I.R. Petersen. “Quantum control theory and applications: a survey.” English. In: *IET Control Theory & Applications* 4 (12 2010), 2651–2671(20). ISSN: 1751-8644.

[20] C. P. Koch et al. “Quantum optimal control in quantum technologies. Strategic report on current status, visions and goals for research in Europe.” In: *EPJ Quantum Technology* 9.1 (2022), p. 19. ISSN: 2196-0763. DOI: `10.1140/epjqt/s40507-022-00138-x`.

[21] M. Shapiro and P. Brumer. *Quantum Control of Molecular Processes*. John Wiley & Sons, Ltd, 2011. ISBN: 9783527639700.

[22] S. Pang and A. N. Jordan. “Optimal adaptive control for quantum metrology with time-dependent Hamiltonians.” In: *Nature Communications* 8.1 (2017), p. 14695. ISSN: 2041-1723. DOI: `10.1038/ncomms14695`.

[23] M. Born and V. Fock. “Beweis des Adiabatensatzes.” In: *Zeitschrift für Physik* 51.3 (1928), pp. 165–180. DOI: `10.1007/BF01343193`.

[24] T. Kato. “On the Adiabatic Theorem of Quantum Mechanics.” In: *Journal of the Physical Society of Japan* 5.6 (1950), pp. 435–439. DOI: `10.1143/JPSJ.5.435`.

[25] D. Møller, L. B. Madsen, and K. Mølmer. “Quantum Gates and Multiparticle Entanglement by Rydberg Excitation Blockade and Adiabatic Passage.” In: *Phys. Rev. Lett.* 100 (17 2008), p. 170504. DOI: `10.1103/PhysRevLett.100.170504`.

[26] M. Saffman, I. I. Beterov, A. Dalal, E. J. Páez, and B. C. Sanders. "Symmetric Rydberg controlled-Z gates with adiabatic pulses." In: *Phys. Rev. A* 101 (6 2020), p. 062309. DOI: 10.1103/PhysRevA.101.062309.

[27] Y. P. Kandel, H. Qiao, S. Fallahi, G. C. Gardner, M. J. Manfra, and J. M. Nichol. "Adiabatic quantum state transfer in a semiconductor quantum-dot spin chain." In: *Nature Communications* 12.1 (2021), p. 2156. ISSN: 2041-1723. DOI: 10.1038/s41467-021-22416-5.

[28] T. Albash and D. A. Lidar. "Adiabatic quantum computation." In: *Rev. Mod. Phys.* 90 (1 2018), p. 015002. DOI: 10.1103/RevModPhys.90.015002.

[29] D. Guéry-Odelin, A. Ruschhaupt, A. Kiely, E. Torrontegui, S. Martínez-Garaot, and J. G. Muga. "Shortcuts to adiabaticity: Concepts, methods, and applications." In: *Rev. Mod. Phys.* 91 (4 2019), p. 045001. DOI: 10.1103/RevModPhys.91.045001.

[30] A. del Campo and K. Kim. "Focus on Shortcuts to Adiabaticity." In: *New Journal of Physics* 21.5 (2019), p. 050201. DOI: 10.1088/1367-2630/ab1437.

[31] L. Zhou, S.-T. Wang, S. Choi, H. Pichler, and M. D. Lukin. "Quantum Approximate Optimization Algorithm: Performance, Mechanism, and Implementation on Near-Term Devices." In: *Phys. Rev. X* 10 (2 2020), p. 021067. DOI: 10.1103/PhysRevX.10.021067.

[32] H. R. Lewis and W. B. Riesenfeld. "An Exact Quantum Theory of the Time-Dependent Harmonic Oscillator and of a Charged Particle in a Time-Dependent Electromagnetic Field." In: *Journal of Mathematical Physics* 10.8 (1969), pp. 1458–1473. DOI: 10.1063/1.1664991.

[33] M. Demirplak and S. A. Rice. "Adiabatic population transfer with control fields." In: *Journal of Physical Chemistry A* 107.46 (2003), pp. 9937–9945. ISSN: 10895639. DOI: 10.1021/jp030708a.

[34] M. V. Berry. "Transitionless quantum driving." In: *Journal of Physics A: Mathematical and Theoretical* 42.36 (2009), pp. 1–9. ISSN: 17518113. DOI: 10.1088/1751-8113/42/36/365303.

[35] M. G. Bason, M. Viteau, N. Malossi, P. Huillery, E. Arimondo, D. Ciampini, R. Fazio, V. Giovannetti, R. Mannella, and O. Morsch. "High-fidelity quantum driving." In: *Nature Physics* 8.2 (2012), pp. 147–152. ISSN: 1745-2481. DOI: 10.1038/nphys2170.

[36] J. Zhang et al. "Experimental Implementation of Assisted Quantum Adiabatic Passage in a Single Spin." In: *Phys. Rev. Lett.* 110 (24 2013), p. 240501. DOI: 10.1103/PhysRevLett.110.240501.

[37] S. An, D. Lv, A. del Campo, and K. Kim. "Shortcuts to adiabaticity by counterdiabatic driving for trapped-ion displacement in phase space." In: *Nature Communications* 7.1 (2016), p. 12999. ISSN: 2041-1723. DOI: 10.1038/ncomms12999.

[38] Y.-X. Du, Z.-T. Liang, Y.-C. Li, X.-X. Yue, Q.-X. Lv, W. Huang, X. Chen, H. Yan, and S.-L. Zhu. "Experimental realization of stimulated Raman shortcut-to-adiabatic passage with cold atoms." In: *Nature Communications* 7.1 (2016), p. 12479. ISSN: 2041-1723. DOI: `10.1038/ncomms12479`.

[39] Antti Vepsäläinen, Sergey Danilin, and Gheorghe Sorin Paraoanu. "Superadiabatic population transfer in a three-level superconducting circuit." In: *Science Advances* 5.2 (2019), eaau5999. DOI: `10.1126/sciadv.aau5999`.

[40] A. Kay. "Perfect, efficient, state transfer and its application as a constructive tool." In: *International Journal of Quantum Information* 08.04 (2010), pp. 641–676. DOI: `10.1142/S0219749910006514`.

[41] S. Ospelkaus, K.-K. Ni, D. Wang, M. H. G. de Miranda, B. Neyenhuis, G. Queméméner, P. S. Julienne, J. L. Bohn, D. S. Jin, and J. Ye. "Quantum-State Controlled Chemical Reactions of Ultracold Potassium-Rubidium Molecules." In: *Science* 327.5967 (2010), pp. 853–857. ISSN: 00368075, 10959203. (Visited on 10/18/2022).

[42] L. D. Landau. "Zur Theorie der Energieübertragung. II." In: *Physics of the Soviet Union* 2 (1932), pp. 46–51.

[43] C. Zener. "Non-adiabatic crossing of energy levels." In: *Proceedings of the Royal Society of London. Series A, Containing Papers of a Mathematical and Physical Character* 137.833 (1932), pp. 696–702. DOI: `10.1098/rspa.1932.0165`.

[44] E. C. G. Stueckelberg. "Theorie der unelastischen Stösse zwischen Atomen." In: *Helvetica Physica Acta* 5.VI (1932), p. 369. ISSN: 0018-0238. DOI: `10.5169/seals-110177`.

[45] E. Majorana. "Atomi orientati in campo magnetico variabile." In: *Il Nuovo Cimento (1924-1942)* 9.2 (1932), pp. 43–50. ISSN: 1827-6121. DOI: `10.1007/BF02960953`.

[46] H. Carmichael. *An Open Systems Approach to Quantum Optics: Lectures Presented at the Université Libre de Bruxelles, October 28 to November 4, 1991*. An Open Systems Approach to Quantum Optics: Lectures Presented at the Université Libre de Bruxelles, October 28 to November 4, 1991 v. 18. Springer Berlin Heidelberg, 1993. ISBN: 9783540566342.

[47] M.O. Scully and M.S. Zubairy. *Quantum Optics*. Quantum Optics. Cambridge University Press, 1997. ISBN: 9780521435956.

[48] J. J. Sakurai and J. Napolitano. *Modern Quantum Mechanics*. 3rd Ed. Cambridge University Press, 2021.

[49] M. V. Berry. "Quantal phase factors accompanying adiabatic changes." In: *Proceedings of the Royal Society of London. A. Mathematical and Physical Sciences* 392.1802 (1984), pp. 45–57. DOI: `10.1098/rspa.1984.0023`.

[50] C. Wittig. "The Landau–Zener Formula." In: *The Journal of Physical Chemistry B* 109.17 (2005), pp. 8428–8430. ISSN: 1520-6106. DOI: `10.1021/jp040627u`.

[51] F. Petiziol. “Accelerated adiabatic quantum control.” PhD thesis. Università di Parma. Dipartimento di Scienze Matematiche, fisiche e informatiche, 2020. URL: https://hdl.handle.net/1889/4010.

[52] F. Petiziol, B. Dive, F. Mintert, and S. Wimberger. “Fast adiabatic evolution by oscillating initial Hamiltonians.” In: *Phys. Rev. A* 98 (4 2018), p. 043436. DOI: 10.1103/PhysRevA.98.043436.

[53] Malossi, N. and Bason, M. G. and Viteau, M. and Arimondo, E. and Mannella, R. and Morsch, O. and Ciampini, D. “Quantum driving protocols for a two-level system: From generalized Landau-Zener sweeps to transitionless control.” In: *Phys. Rev. A* 87 (1 2013), p. 012116.

[54] A. T. Rezakhani, W.-J. Kuo, A. Hamma, D. A. Lidar, and P. Zanardi. “Quantum Adiabatic Brachistochrone.” In: *Phys. Rev. Lett.* 103 (8 2009), p. 080502. DOI: 10.1103/PhysRevLett.103.080502.

[55] D. A. Lidar, A. T. Rezakhani, and A. Hamma. “Adiabatic approximation with exponential accuracy for many-body systems and quantum computation.” In: *Journal of Mathematical Physics* 50.10 (2009), p. 102106. DOI: 10.1063/1.3236685.

[56] F. Petiziol, B. Dive, S. Carretta, R. Mannella, F. Mintert, and S. Wimberger. “Accelerating adiabatic protocols for entangling two qubits in circuit QED.” In: *Phys. Rev. A* 99 (4 2019), p. 042315. DOI: 10.1103/PhysRevA.99.042315.

[57] J. Roland and N. J. Cerf. “Quantum search by local adiabatic evolution.” In: *Phys. Rev. A* 65 (4 2002), p. 042308. DOI: 10.1103/PhysRevA.65.042308.

[58] Dionisis Stefanatos and Emmanuel Paspalakis. “Speeding up adiabatic passage with an optimal modified Roland–Cerf protocol.” In: *Journal of Physics A: Mathematical and Theoretical* 53.11 (2020), p. 115304. DOI: 10.1088/1751-8121/ab7423.

[59] E.B. Davies. *Quantum Theory of Open Systems*. Academic Press, 1976. ISBN: 9780122061509.

[60] H.-P. Breuer and F. Petruccione. *The Theory of Open Quantum Systems*. Oxford: Oxford University Press, 2007, p. 656. ISBN: 9780199213900. DOI: 10.1093/acprof:oso/9780199213900.001.0001.

[61] G Lindblad. “On the generators of quantum dynamical semigroups.” In: *Communications in Mathematical Physics* 48.2 (1976), pp. 119–130. ISSN: 1432-0916. DOI: 10.1007/BF01608499.

[62] V. Gorini, A. Kossakowski, and E. C. G. Sudarshan. “Completely positive dynamical semigroups of N-level systems.” In: *Journal of Mathematical Physics* 17.5 (1976), pp. 821–825. DOI: 10.1063/1.522979.

[63] D. Manzano. “A short introduction to the Lindblad master equation.” In: *AIP Advances* 10.2 (2020), p. 025106. DOI: 10.1063/1.5115323.

[64] F. Herrera and F. C. Spano. “Cavity-Controlled Chemistry in Molecular Ensembles.” In: *Phys. Rev. Lett.* 116 (23 2016), p. 238301. DOI: 10.1103/PhysRevLett.116.238301.

[65] S. Zahedpour, J. K. Wahlstrand, and H. M. Milchberg. "Quantum Control of Molecular Gas Hydrodynamics." In: *Phys. Rev. Lett.* 112 (14 2014), p. 143601. DOI: `10.1103/PhysRevLett.112.143601`.

[66] H. Wu and J. E. Thomas. "Optical Control of Feshbach Resonances in Fermi Gases Using Molecular Dark States." In: *Phys. Rev. Lett.* 108 (1 2012), p. 010401. DOI: `10.1103/PhysRevLett.108.010401`.

[67] T. Fennel, K.-H. Meiwes-Broer, J. Tiggesbäumker, P.-G. Reinhard, P. M. Dinh, and E. Suraud. "Laser-driven nonlinear cluster dynamics." In: *Rev. Mod. Phys.* 82 (2 2010), pp. 1793–1842. DOI: `10.1103/RevModPhys.82.1793`.

[68] L. Xia, X.-D. Wang, C.-J. Xuan, X.-J. Zeng, H.-K. Li, S. X. Tian, Y. Pan, and K.-C. Lau. "Communication: State mixing by spin-orbit coupling in the anionic chloroiodine dissociations." In: *The Journal of Chemical Physics* 140.4 (2014), p. 041106. DOI: `10.1063/1.4862684`.

[69] C. M. Marian. "Spin–orbit coupling and intersystem crossing in molecules." In: *WIREs Computational Molecular Science* 2.2 (2012), pp. 187–203. DOI: `https://doi.org/10.1002/wcms.83`.

[70] A. S. Miñarro and G. Herranz. "Jahn-Teller states mixed by spin-orbit coupling in an electromagnetic field." In: *Phys. Rev. B* 106 (16 2022), p. 165108. DOI: `10.1103/PhysRevB.106.165108`.

[71] L. Li and A.M. Lyyra. "Triplet states of Na_2 and Li_2 by perturbation facilitated optical–optical double resonance spectroscopy." In: *Spectrochimica Acta Part A: Molecular and Biomolecular Spectroscopy* 55.11 (1999), pp. 2147–2178. ISSN: 1386-1425. DOI: `https://doi.org/10.1016/S1386-1425(99)00091-8`.

[72] B. Beser, V. B. Sovkov, J. Bai, E. H. Ahmed, C. C. Tsai, F. Xie, L. Li, V. S. Ivanov, and A. M. Lyyra. "Experimental investigation of the $^{85}Rb_2$ $a^3\Sigma_u^+$ triplet ground state: Multiparameter Morse long range potential analysis." In: *The Journal of Chemical Physics* 131.9 (2009), p. 094505. DOI: `10.1063/1.3194290`.

[73] Teodora Kirova and Frank C. Spano. "Designing molecular eigenstates in a four-level Λ system." In: *Phys. Rev. A* 71 (6 2005), p. 063816. DOI: `10.1103/PhysRevA.71.063816`.

[74] M. V. Korolkov and J. Manz. "Coherent spin control of matrix isolated molecules by IR+UV laser pulses: Quantum simulations for ClF in Ar." In: *The Journal of Chemical Physics* 120.24 (2004), pp. 11522–11531. DOI: `10.1063/1.1753256`.

[75] J. González-Vázquez, I. R. Sola, J. Santamaria, and V. S. Malinovsky. "Quantum control of spin–orbit coupling by dynamic Stark-shifts induced by laser fields." In: *Chemical Physics Letters* 431.4 (2006), pp. 231–235. ISSN: 0009-2614. DOI: `https://doi.org/10.1016/j.cplett.2006.09.085`.

[76] J. González-Vázquez, Ignacio R. Sola, J. Santamaria, and V. S. Malinovsky. “Optical control of the singlet-triplet transition in Rb_2.” In: *The Journal of Chemical Physics* 125.12 (2006), p. 124315. DOI: 10.1063/1.2355492.

[77] S. H. Autler and C. H. Townes. “Stark Effect in Rapidly Varying Fields.” In: *Phys. Rev.* 100 (2 1955), pp. 703–722. DOI: 10.1103/PhysRev.100.703.

[78] E. H. Ahmed, J. Huennekens, T. Kirova, J. Qi, and A. M. Lyyra. “The Autler–Townes Effect in Molecules: Observations, Theory, and Applications.” In: *Advances in Atomic, Molecular, and Optical Physics*. Ed. by Paul Berman, Ennio Arimondo, and Chun Lin. Vol. 61. Advances In Atomic, Molecular, and Optical Physics. Academic Press, 2012, pp. 467–514. DOI: https://doi.org/10.1016/B978-0-12-396482-3.00009-0.

[79] E. H. Ahmed, S. Ingram, T. Kirova, O. Salihoglu, J. Huennekens, J. Qi, Y. Guan, and A. M. Lyyra. “Quantum Control of the Spin-Orbit Interaction Using the Autler-Townes Effect.” In: *Phys. Rev. Lett.* 107 (16 2011), p. 163601. DOI: 10.1103/PhysRevLett.107.163601.

[80] P. Qi et al. “New spectroscopic data, spin-orbit functions, and global analysis of data on the $A^1\Sigma_u^+$ and $b^3\Pi_u$ states of Na_2.” In: *The Journal of Chemical Physics* 127.4 (2007), p. 044301. DOI: 10.1063/1.2747595.

[81] M. R. Manaa, A. J. Ross, F. Martin, P. Crozet, A. M. Lyyra, L. Li, C. Amiot, and T. Bergeman. “Spin–orbit interactions, new spectral data, and deperturbation of the coupled $\mathrm{b}^3\Pi_u$ and $\mathrm{A}^1\Sigma_u^+$ states of K_2.” In: *The Journal of Chemical Physics* 117.24 (2002), pp. 11208–11215. DOI: 10.1063/1.1522716.

[82] H. Salami et al. “Spectroscopic observations, spin-orbit functions, and coupled-channel deperturbation analysis of data on the $A^1\Sigma_u^+$ and $b\,^3\Pi_u$ states of Rb_2.” In: *Phys. Rev. A* 80 (2 2009), p. 022515. DOI: 10.1103/PhysRevA.80.022515.

[83] E. H. Bai J.and Ahmed et al. “Global analysis of data on the spin-orbit-coupled $A\,^1\Sigma_u^+$ and $b^3\Pi_u$ states of Cs_2.” In: *Phys. Rev. A* 83 (3 2011), p. 032514. DOI: 10.1103/PhysRevA.83.032514.

[84] E. H. Ahmed and A. M. Lyyra. “Frequency domain control of quantum state singlet/triplet character and prospects for an all-optical spin switch.” In: *Journal of Modern Optics* 61.1 (2014), pp. 7–12. DOI: 10.1080/09500340.2013.827248.

[85] D. D. Konowalow and J. L. Fish. “The molecular electronic structure of the twenty-six lowest lying states of Li_2 at short and intermediate internuclear separations.” In: *Chemical Physics* 84.3 (1984), pp. 463–475. ISSN: 0301-0104. DOI: https://doi.org/10.1016/0301-0104(84)85195-2.

[86] R. Gómez-Abal and W. Hübner. “Simple model for laser-induced electron dynamics.” In: *Phys. Rev. B* 65 (19 2002), p. 195114. DOI: 10.1103/PhysRevB.65.195114.

[87] I. R. Sola, J. González-Vázquez, and V. S. Malinovsky. "Optical control of a spin switch in the weak spin-orbit coupling limit." In: *Phys. Rev. A* 74 (4 2006), p. 043418. DOI: 10.1103/PhysRevA.74.043418.

[88] E. H. Ahmed, X. Pan, J. Huennekens, and A. M. Lyyra. "Optical control of collisional population flow between molecular electronic states of different spin multiplicity." In: *Phys. Rev. A* 89 (6 2014), p. 061401. DOI: 10.1103/PhysRevA.89.061401.

[89] D. A. Garanin and R. Schilling. "Effects of nonlinear sweep in the Landau-Zener-Stueckelberg effect." In: *Phys. Rev. B* 66 (17 2002), p. 174438. DOI: 10.1103/PhysRevB.66.174438.

[90] E Brion, L H Pedersen, and K Mølmer. "Adiabatic elimination in a lambda system." In: *Journal of Physics A: Mathematical and Theoretical* 40.5 (2007), pp. 1033–1043. DOI: 10.1088/1751-8113/40/5/011.

[91] M. Delvecchio, T. Kirova, E. Arimondo, D. Ciampini, and S. Wimberger. "High-fidelity quantum control via Autler-Townes splitting." In: *Phys. Rev. A* 106 (5 2022), p. 052802. DOI: 10.1103/PhysRevA.106.052802.

[92] S. Masuda and S. A. Rice. "A model study of assisted adiabatic transfer of population in the presence of collisional dephasing." In: *The Journal of Chemical Physics* 142.24 (2015), p. 244303. DOI: 10.1063/1.4922779.

[93] A. Levy, E. Torrontegui, and R. Kosloff. "Action-noise-assisted quantum control." In: *Phys. Rev. A* 96 (3 2017), p. 033417. DOI: 10.1103/PhysRevA.96.033417.

[94] A. Levy, A. Kiely, J. G. Muga, R. Kosloff, and E. Torrontegui. "Noise resistant quantum control using dynamical invariants." In: *New Journal of Physics* 20.2 (2018), p. 025006. DOI: 10.1088/1367-2630/aaa9e5.

[95] B. B. Zhou, A. Baksic, H. Ribeiro, C. G. Yale, F. J. Heremans, P. C. Jerger, A. Auer, G. Burkard, A. A. Clerk, and D. D. Awschalom. "Accelerated quantum control using superadiabatic dynamics in a solid-state lambda system." In: *Nature Physics* 13.4 (2017), pp. 330–334. ISSN: 1745-2481. DOI: 10.1038/nphys3967.

[96] M. Grifoni and P. Hänggi. "Driven quantum tunneling." In: *Physics Reports* 304.5 (1998), pp. 229–354. ISSN: 0370-1573. DOI: https://doi.org/10.1016/S0370-1573(98)00022-2.

[97] Sigmund Kohler, Thomas Dittrich, and Peter Hänggi. "Floquet-Markovian description of the parametrically driven, dissipative harmonic quantum oscillator." In: *Phys. Rev. E* 55 (1 1997), pp. 300–313. DOI: 10.1103/PhysRevE.55.300.

[98] R. Blümel, A. Buchleitner, R. Graham, L. Sirko, U. Smilansky, and H. Walther. "Dynamical localization in the microwave interaction of Rydberg atoms: The influence of noise." In: *Phys. Rev. A* 44 (7 1991), pp. 4521–4540. DOI: 10.1103/PhysRevA.44.4521.

[99] M. Delvecchio, F. Petiziol, and S. Wimberger. “The Renewed Role of Sweep Functions in Noisy Shortcuts to Adiabaticity.” In: *Entropy* 23.7 (2021). ISSN: 1099-4300. DOI: `10.3390/e23070897`.

[100] P. Sompet, S. S. Szigeti, E. Schwartz, A. S. Bradley, and M. F. Andersen. “Thermally robust spin correlations between two 85Rb atoms in an optical microtrap.” In: *Nature Communications* 10.1 (2019), p. 1889. ISSN: 2041-1723. DOI: `10.1038/s41467-019-09420-6`.

[101] L. A. Reynolds, E. Schwartz, U. Ebling, M. Weyland, J. Brand, and M. F. Andersen. “Direct Measurements of Collisional Dynamics in Cold Atom Triads.” In: *Phys. Rev. Lett.* 124 (7 2020), p. 073401. DOI: `10.1103/PhysRevLett.124.073401`.

[102] M. Weyland, S. S. Szigeti, R. A. B. Hobbs, P. Ruksasakchai, L. Sanchez, and M. F. Andersen. “Pair Correlations and Photoassociation Dynamics of Two Atoms in an Optical Tweezer.” In: *Phys. Rev. Lett.* 126 (8 2021), p. 083401. DOI: `10.1103/PhysRevLett.126.083401`.

[103] D.F. Walls and G.J. Milburn. *Quantum Optics*. Springer Berlin Heidelberg, 2008. ISBN: 9783540285731.

[104] A. A. Clerk, M. H. Devoret, S. M. Girvin, Florian Marquardt, and R. J. Schoelkopf. “Introduction to quantum noise, measurement, and amplification.” In: *Rev. Mod. Phys.* 82 (2 2010), pp. 1155–1208. DOI: `10.1103/RevModPhys.82.1155`.

[105] T. C. Ralph, S. D. Bartlett, J. L. O’Brien, G. J. Pryde, and H. M. Wiseman. “Quantum nondemolition measurements for quantum information.” In: *Phys. Rev. A* 73 (1 2006), p. 012113. DOI: `10.1103/PhysRevA.73.012113`.

[106] C. Zhang, F. Pokorny, W. Li, G. Higgins, A. Pöschl, I. Lesanovsky, and M. Hennrich. “Submicrosecond entangling gate between trapped ions via Rydberg interaction.” In: *Nature* 580.7803 (2020), pp. 345–349. ISSN: 1476-4687. DOI: `10.1038/s41586-020-2152-9`.

[107] A. Blais, A. L. Grimsmo, S. M. Girvin, and A. Wallraff. “Circuit quantum electrodynamics.” In: *Rev. Mod. Phys.* 93 (2 2021), p. 025005. DOI: `10.1103/RevModPhys.93.025005`.

[108] J. Majer et al. “Coupling superconducting qubits via a cavity bus.” In: *Nature* 449.7161 (2007), pp. 443–447. ISSN: 1476-4687. DOI: `10.1038/nature06184`.

[109] M. H. Levitt. “Composite pulses.” In: *Progress in Nuclear Magnetic Resonance Spectroscopy* 18.2 (1986), pp. 61–122. ISSN: 0079-6565. DOI: `https://doi.org/10.1016/0079-6565(86)80005-X`.

[110] J. A. Jones. “Quantum computing with NMR.” In: *Progress in Nuclear Magnetic Resonance Spectroscopy* 59.2 (2011), pp. 91–120. ISSN: 0079-6565. DOI: `https://doi.org/10.1016/j.pnmrs.2010.11.001`.

[111] S. J. Glaser et al. “Training Schrödinger’s cat: quantum optimal control.” In: *The European Physical Journal D* 69.12 (2015), p. 279. ISSN: 1434-6079. DOI: `10.1140/epjd/e2015-60464-1`.

[112] M. Saffman, T. G. Walker, and K. Mølmer. "Quantum information with Rydberg atoms." In: *Rev. Mod. Phys.* 82 (3 2010), pp. 2313–2363. DOI: `10.1103/RevModPhys.82.2313`.

[113] D. D. B. Rao and K. Mølmer. "Robust Rydberg-interaction gates with adiabatic passage." In: *Phys. Rev. A* 89 (3 2014), p. 030301. DOI: `10.1103/PhysRevA.89.030301`.

[114] I. I. Beterov, D. B. Tretyakov, V. M. Entin, E. A. Yakshina, I. I. Ryabtsev, M. Saffman, and S. Bergamini. "Application of adiabatic passage in Rydberg atomic ensembles for quantum information processing." In: *Journal of Physics B: Atomic, Molecular and Optical Physics* 53.18 (2020), p. 182001. DOI: `10.1088/1361-6455/ab8719`.

[115] S. de Léséleuc, D. Barredo, V. Lienhard, A. Browaeys, and T. Lahaye. "Analysis of imperfections in the coherent optical excitation of single atoms to Rydberg states." In: *Phys. Rev. A* 97 (5 2018), p. 053803. DOI: `10.1103/PhysRevA.97.053803`.

[116] S. Ravets, H. Labuhn, D. Barredo, L. Béguin, T. Lahaye, and A. Browaeys. "Coherent dipole–dipole coupling between two single Rydberg atoms at an electrically-tuned Förster resonance." In: *Nature Physics* 10.12 (2014), pp. 914–917. ISSN: 1745-2481. DOI: `10.1038/nphys3119`.

[117] G. Higgins, F. Pokorny, C. Zhang, Q. Bodart, and M. Hennrich. "Coherent Control of a Single Trapped Rydberg Ion." In: *Phys. Rev. Lett.* 119 (22 2017), p. 220501. DOI: `10.1103/PhysRevLett.119.220501`.

[118] X.-R. Huang, Z.-X. Ding, C.-S. Hu, L.-T. Shen, W. Li, H. Wu, and S.-B. Zheng. "Robust Rydberg gate via Landau-Zener control of Förster resonance." In: *Phys. Rev. A* 98 (5 2018), p. 052324. DOI: `10.1103/PhysRevA.98.052324`.

[119] N. V. Vitanov, A. A. Rangelov, B. W. Shore, and K. Bergmann. "Stimulated Raman adiabatic passage in physics, chemistry, and beyond." In: *Rev. Mod. Phys.* 89 (1 2017), p. 015006. DOI: `10.1103/RevModPhys.89.015006`.

[120] Thomas F. Gallagher and Pierre Pillet. "Dipole–Dipole Interactions of Rydberg Atoms." In: *Advances in Atomic, Molecular, and Optical Physics*. Vol. 56. Advances In Atomic, Molecular, and Optical Physics. Academic Press, 2008, pp. 161–218. DOI: `https://doi.org/10.1016/S1049-250X(08)00013-X`.

[121] M. Delvecchio, F. Petiziol, E. Arimondo, and S. Wimberger. "Atomic interactions for qubit-error compensation." In: *Phys. Rev. A* 105 (4 2022), p. 042431. DOI: `10.1103/PhysRevA.105.042431`.

[122] B. M. Garraway. "The Dicke model in quantum optics: Dicke model revisited." In: *Philosophical Transactions: Mathematical, Physical and Engineering Sciences* 369.1939 (2011), pp. 1137–1155. ISSN: 1364503X. (Visited on 10/24/2022).

[123] Z. Ficek and R. Tanaś. “Entangled states and collective nonclassical effects in two-atom systems.” In: *Physics Reports* 372.5 (2002), pp. 369–443. ISSN: 0370-1573. DOI: https://doi.org/10.1016/S0370-1573(02)00368-X.

[124] K. Almutairi, R. Tanaś, and Z. Ficek. “Generating two-photon entangled states in a driven two-atom system.” In: *Phys. Rev. A* 84 (1 2011), p. 013831. DOI: 10.1103/PhysRevA.84.013831.

[125] D. Comparat and P. Pillet. “Dipole blockade in a cold Rydberg atomic sample.” In: *J. Opt. Soc. Am. B* 27.6 (2010), A208–A232. DOI: 10.1364/JOSAB.27.00A208.

[126] S.-L. Su, Y. Gao, E. Liang, and S. Zhang. “Fast Rydberg antiblockade regime and its applications in quantum logic gates.” In: *Phys. Rev. A* 95 (2 2017), p. 022319. DOI: 10.1103/PhysRevA.95.022319.

[127] Bruce W. Shore. “Picturing stimulated Raman adiabatic passage: a STIRAP tutorial.” In: *Adv. Opt. Photon.* 9.3 (2017), pp. 563–719. DOI: 10.1364/AOP.9.000563.

[128] K. Bergmann, H. Theuer, and B. W. Shore. “Coherent population transfer among quantum states of atoms and molecules.” In: *Rev. Mod. Phys.* 70 (3 1998), pp. 1003–1025. DOI: 10.1103/RevModPhys.70.1003.

[129] S. Guérin, L. P. Yatsenko, T. Halfmann, B. W. Shore, and K. Bergmann. “Stimulated hyper-Raman adiabatic passage. II. Static compensation of dynamic Stark shifts.” In: *Phys. Rev. A* 58 (6 1998), pp. 4691–4704. DOI: 10.1103/PhysRevA.58.4691.

[130] L. P. Yatsenko, S. Guérin, T. Halfmann, K. Böhmer, B. W. Shore, and K. Bergmann. “Stimulated hyper-Raman adiabatic passage. I. The basic problem and examples.” In: *Phys. Rev. A* 58 (6 1998), pp. 4683–4690. DOI: 10.1103/PhysRevA.58.4683.

[131] L. Giannelli and E. Arimondo. “Three-level superadiabatic quantum driving.” In: *Phys. Rev. A* 89 (3 2014), p. 033419. DOI: 10.1103/PhysRevA.89.033419.

[132] T. A. Laine and S. Stenholm. “Adiabatic processes in three-level systems.” In: *Phys. Rev. A* 53 (4 1996), pp. 2501–2512. DOI: 10.1103/PhysRevA.53.2501.

[133] J.-L. Wu, Y. Wang, J.-X. Han, S.-L. Su, Y. Xia, Y. Jiang, and J. Song. “Resilient quantum gates on periodically driven Rydberg atoms.” In: *Phys. Rev. A* 103 (1 2021), p. 012601. DOI: 10.1103/PhysRevA.103.012601.

[134] Ehret, Tim. “Optimizing elementary quantum gates.” In: *Bachelor Thesis, Heidelberg University* (2020).

[135] L. Isenhower, E. Urban, X. L. Zhang, A. T. Gill, T. Henage, T. A. Johnson, T. G. Walker, and M. Saffman. “Demonstration of a Neutral Atom Controlled-NOT Quantum Gate.” In: *Phys. Rev. Lett.* 104 (1 2010), p. 010503. DOI: 10.1103/PhysRevLett.104.010503.

[136] M. H. S. Amin. “Consistency of the Adiabatic Theorem.” In: *Phys. Rev. Lett.* 102 (22 2009), p. 220401. DOI: `10.1103/PhysRevLett.102.220401`.

[137] L.M. Garrido and F.J. Sancho. “Degree of approximate validity of the adiabatic invariance in quantum mechanics.” In: *Physica* 28.6 (1962), pp. 553–560. ISSN: 0031-8914. DOI: `https://doi.org/10.1016/0031-8914(62)90109-X`.